The influence of river-derived particles on estuarine and marine elemental cycles: Evidence from lithium isotopes

Chun-Yao Liu [a,*], David J. Wilson [a], Ed C. Hathorne [b], Antao Xu [b],
Philip A.E. Pogge von Strandmann [a,c]

[a] London Geochemistry and Isotope Centre (LOGIC), Institute of Earth and Planetary Sciences, University College London and Birkbeck, University of London, Gower Street, London WC1E 6BT, UK
[b] GEOMAR Helmholtz Centre for Ocean Research Kiel, Wischhofstrasse 1-3, Kiel 24148, Germany
[c] Mainz Isotope Geochemistry (MIGHTY), Institute of Geosciences, Johannes Gutenberg University, 55122 Mainz, Germany

ARTICLE INFO

ABSTRACT

To examine the alteration of river-derived sediments through a large estuary and the implications for elemental cycling and global climate, this study analyses lithium (Li) isotopes and elemental concentrations (e.g., Li, Na, Mg, K, Ca, Fe and Al) of both the dissolved load and different phases of the sediment load (i.e., exchangeable, carbonate, oxide, clay and residue) in the Amazon estuary. The results show that river-derived sediments remove Li from the dissolved load, largely due to cation retention in secondary clays. By modelling the Li mass-balance and isotope fractionation, we estimate that the river-derived sediments gain 3–4 µg/g Li from the dissolved load in the Amazon estuary, with a Li isotope fractionation factor ($\alpha_{\text{clay-solution}}$) of approximately 0.975. Considering the whole Amazon estuary, the river-derived sediments remove around $3.6–4.8 \times 10^9$ g/yr of Li from the dissolved load. Specifically, around $1.0–1.7 \times 10^8$ g/yr of Li is removed from river water (~1.8–3.0% of the dissolved Li discharge flux of the Amazon River) and around $3.5–4.7 \times 10^9$ g/yr of Li is removed from seawater, which represents a significant sink from the ocean. This estuarine Li sink is likely to be related to continental erosion rates; thus, continental weathering and erosion regimes could influence not only riverine Li input, but could also directly affect the Li sink, leading to a dual control on the Li budget and isotope composition in the ocean.

1. Introduction

Continental weathering is a critical process in climate stabilization and global elemental cycling (Walker et al., 1981; Berner and Berner, 1996; Gislason et al., 2009). Chemical weathering, especially the hydrolysis of silicates, consumes atmospheric carbon dioxide (CO_2) and can therefore act as a climate thermostat. Every year, continental physical erosion and chemical weathering supply billions of tonnes of solid material (particles) ($\sim 1.8 \times 10^{13}$ kg/yr) and dissolved material ($\sim 3.8 \times 10^{12}$ kg/yr), including cations, alkalinity and nutrients, to the ocean by river transportation through estuaries (Milliman and Farnsworth, 2011). Estuarine processes are therefore critical for determining the state of the material fluxes (particulates vs. dissolved) to the oceans, and hence for marine biogeochemical cycles (Boyle et al., 1974; Oelkers et al., 2011).

Estuaries link continents and oceans, and they are regions in which

aqueous chemistry changes significantly and rapidly. Hence, the products from continental weathering can be further altered by sediment-water interaction processes while the river-derived particles pass through the estuary with the salinity increasing from 0 to 35 before sediment burial and diagenesis. Theoretically, this alteration includes both mineral dissolution causing element release and mineral formation causing element incorporation. Notably, if the cations are incorporated into aluminosilicates instead of carbonate, there is no carbon burial in the ocean and therefore no net atmospheric CO_2 consumption (Berner and Berner, 1997). This formation of aluminosilicates in the ocean, including in the estuary, at the continental shelf and/or at the ocean floor, has been termed as *reverse weathering* in some previous studies (Mackenzie and Garrels, 1966; Mackenzie and Kump, 1995; Krissansen-Totton and Catling, 2020). The behaviour of many elements in estuaries has previously been explored, with typically more than 70% of the dissolved riverine Fe, and 20–50% of the dissolved riverine Al and U,

being removed in low-salinity zones by flocculation and clay uptake (Boyle et al., 1977; Hydes and Liss, 1977; Sholkovitz, 1978; Morris et al., 1986; Chester, 1990; Porcelli et al., 1997; Schroth et al., 2014; Zhu et al., 2018). In contrast, dissolved Na, K and Mg have been observed to undergo conservative mixing between river water and seawater in many estuaries (Chester, 1990; Pogge von Strandmann et al., 2008). In addition, the estuarine behaviour of heavy metals, nutrients and organic carbon, and their influence on elemental fluxes, has also been explored (Sholkovitz, 1978; Chester, 1990; Benner and Opsahl, 2001; Callahan et al., 2004; Yao et al., 2014; Jiang et al., 2019).

Lithium (Li) and its isotopes (^{6}Li and ^{7}Li) are powerful tracers of silicate weathering, due to the significant isotopic fractionation during chemical weathering and the orders of magnitude higher Li concentrations in silicates than carbonates or plants, which lead to negligible influences from carbonate weathering and biological processes (Kisakürek et al., 2005; Clergue et al., 2015; Dellinger et al., 2015; Tomascak et al., 2016; Pogge von Strandmann et al., 2020). Furthermore, both particle-water interaction experiments and studies on natural systems have shown that there is no significant fractionation during mineral dissolution (Pistiner and Henderson, 2003; Wimpenny et al., 2010a; Dellinger et al., 2015). In contrast, the lighter Li isotope (^{6}Li) prefers to partition into solid phases during secondary mineral formation (e.g., clays and Fe/Mn-oxides/oxyhydroxides). An isotopic fractionation of up to 15‰ accompanies Li adsorption on the negatively charged surfaces of clays (i.e., exchangeable Li), whereas an isotopic fractionation greater than 15‰ occurs when Li enters lattice sites, such as the octahedral sites in clays, six-membered rings in gibbsite and Li-O-Fe bonds in Fe oxides (Vigier et al., 2008; Kim and Grey, 2010; Wimpenny et al., 2015; Hindshaw et al., 2019; Pogge von Strandmann et al., 2020). Thus, Li isotopes are a useful tracer of weathering congruency, defined as the ratio of primary silicate dissolution to secondary mineral uptake (Dellinger et al., 2015; Pogge von Strandmann and Henderson, 2015; Pogge von Strandmann et al., 2020).

In the modern day, global rivers transport around 5.6–6.9 × 10^{10} g/yr (8.0–10 × 10^9 mol/yr) of dissolved Li to the estuaries, with a mean δ^7Li value of 23‰, which represents one of the major input fluxes of Li to the ocean (Huh et al., 1998). However, these estimates are based on the Li concentration and isotopes of river waters measured close to the coast but before passing through estuaries (Huh et al., 1998). Furthermore, modern global rivers transport at least 1.5 × 10^{11} g/yr of Li in the particulate load (Viers et al., 2009; Oelkers et al., 2011), whose influence on modification of the riverine-dissolved Li input flux in the estuaries has not yet been widely explored. In addition, to date, there remain large uncertainties regarding Li sink fluxes and their isotopic fractionation from seawater. Currently, the two major Li sinks are thought to be an alteration of the (basaltic) oceanic crust (AOC) and uptake by marine aluminous authigenic clays (MAAC), also known as reverse weathering (Chan et al., 1992, 2002; Elderfield and Schultz, 1996; Zhang et al., 1998) (Table S1). The estimated AOC Li sink ranges from 1.0 to 14.6 × 10^{10} g/yr, with fractionation (Δ^7Li$_{AOC-seawater}$) ranging from −11‰ to −19‰ (Table S1). The estimated MAAC Li sink is 2.4–25.7 × 10^{10} g/yr, with fractionation (Δ^7Li$_{MAAC-seawater}$) ranging from −5‰ to −28‰ (Table S1). However, the current MAAC Li sink has mainly been explored as a diagenetic process that occurs after burial or in the open ocean, including authigenic clay formation (Hoefs and Sywall, 1997; Huh et al., 1998), marine clay uptake (Seyfried et al., 1984; Elderfield and Schultz, 1996) and clay authigenesis in carbonate-rich sedimentary environments due to the biogenic silica (Andrews et al., 2020). However, the alteration of river-derived sediment in the estuarine transects before burial has not been included, or indeed particularly studied.

So far, only a few studies have examined Li and its isotopes in estuaries, and they are not sufficient to constrain the behaviour of Li in estuaries at a global scale. In general, dissolved river Li concentrations have shown conservative mixing with seawater (Brunskill et al., 2003; Pogge von Strandmann et al., 2008; Yang et al., 2021), but dissolved river Li isotopes and particulate load Li and Li isotopes suggest that some

dissolved Li is removed by particles in estuaries (Brunskill et al., 2003; Pogge von Strandmann et al., 2008; Murphy et al., 2014; Yang et al., 2021). Hence, the understanding of Li geochemistry behaviour globally remains limited because of the lack of data from the estuaries of many major rivers, including the Amazon River.

In this study, to explore Li behaviour during estuarine processes and to constrain its influence on the oceanic Li budget, we examined a series of dissolved load samples and particulate samples (suspended and bedload sediments) from the Amazon estuary. Because of the strong relationship between Li isotope fractionation and Li occupying sites in secondary minerals (Vigier et al., 2008; Wimpenny et al., 2015; Hindshaw et al., 2019; Pogge von Strandmann et al., 2020), the particulate samples were separated into five operationally defined phases (i.e., exchangeable, carbonate, oxide, clay and residue) using a sequential chemical extraction method (Tessier et al., 1979; Pogge von Strandmann et al., 2019a; Liu et al., 2022). Elemental concentrations (e.g., Na, Mg, Ca, K, Al, Fe, Mn, Li) and Li isotope compositions were analysed in both the dissolved loads and the leachates extracted from the particulate samples, enabling an assessment of the alteration of river-derived sediments in the Amazon estuary.

2. Study area and sampling

2.1. Study area

The Amazon River is the largest river in the world and drains an area of around 6.3 × 10^6 km^2 in the tropics of northern South America. It originates in the Andes, converges with tributaries from the Guyana and Brazilian shields, and runs through the Amazon floodplain, before entering the Atlantic Ocean at Para, Brazil (Gibbs, 1967). The continental erosion, chemical weathering and biogeochemistry of the Amazon River catchment have been widely explored through major elements, trace elements, REEs, and isotope systems including Li, Ni, Sr, Mo, Ba and U (Gibbs, 1967; Stallard, 1985; Gaillardet et al., 1997; Vital and Statteger, 2000; Dosseto et al., 2006; Bouchez et al., 2014; Dellinger et al., 2014, 2015; Charbonnier et al., 2020; Revels et al., 2021a, 2021b). Lithium isotopes in Amazon River water are controlled by the proportion of Li that enters secondary minerals relative to that supplied from the dissolution of primary rocks, and they show a 'boomerang' relationship with the ratio of chemical weathering rates to total denudation rates, where denudation comprises both chemical weathering and physical erosion rates (Dellinger et al., 2015).

In its estuary, the Amazon River discharges around 6300 km^3/yr (6.3 × 10^{15} kg/yr) of water and 1.2 × 10^{12} kg/yr of particles to the Atlantic Ocean (Gibbs, 1967; Milliman and Farnsworth, 2011; Dellinger et al., 2015). The continental shelf adjacent to the Amazon River mouth is as wide as 300 km, narrowing to 100 km towards the northwest (Fig. 1). The inner shelf is relatively flat and smooth to about the 40 m isobath, where the shelf steepens abruptly. The outer shelf (60–100 m water depth) is again relatively flat, but it is mantled with large-scale bedforms oriented perpendicular to the shelf break (Kuehl et al., 1982). In the Amazon estuary, the Amazon River splits into the north and south channels (Fig. 1). The Amazon estuary is located under easterly prevailing trade winds, which shift between northeasterly winds (December to June) and southeasterly winds (June to December) (Kuehl et al., 1982; Nittrouer and DeMaster, 1996). The North Brazil Current flows along the Amazon shelf towards northwest, and the flow is at a maximum in July to August and a minimum in April to May (Kuehl et al., 1982; Condie, 1991; Geyer et al., 1996). In addition, the semidiurnal tides near the Amazon mouth can produce a strong tidal wave, with a tidal range of up to 10 m, over the shelf and into the river mouth (Gibbs, 1976; Geyer et al., 1996; Nittrouer and DeMaster, 1996).

The freshwater from the Amazon debouches onto the shelf through the north and south channels, then mixes with saline seawater in the direction of offshore (Geyer et al., 1996). The bottom water salinity increases to reach 35 at around the 15 m isobath and 150 km away from
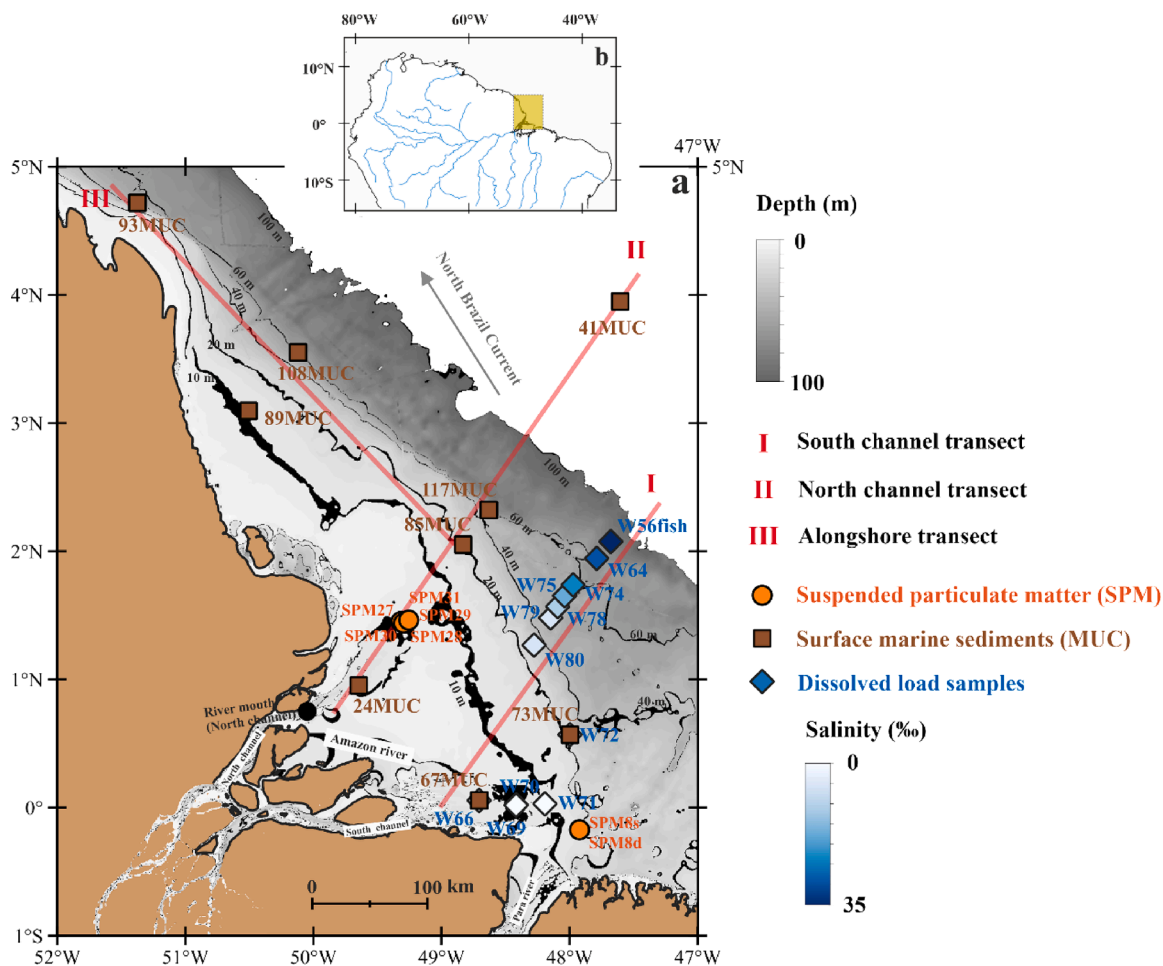
Fig. 1. Setting of the Amazon estuary and sampling locations. (a) The contours indicating isobaths. The grey color bar demonstrates the ocean water depth from 0 to 100 m. The isobaths and water depth are based on bathymetry data from GEBCO (The General Bathymetric Chart of the Oceans). Locations of the dissolved load, suspended particulate matter and ocean marine sediment samples are marked by symbols and labelled. The blue colour filling for each dissolved load sample shows salinity. The red lines numbered I, II and III refer to the sampling transects. The grey arrow shows the direction of North Brazil Current (NBC). (b) The shaded area corresponds to the area of map (a).

the river mouth. The near-surface salinity shows seasonal variations, with the surface salinity reaching 35 at around 260 km away from the river mouth during the high-discharge season, but at around 200 km from the river mouth during the low-discharge season (Geyer et al., 1996). In the alongshore direction, part of the freshwater goes northwards and forms a relatively homogenous salinity belt running parallel to the shore, with salinity increasing offshore (Geyer et al., 1996). The riverine particles discharge through the north and south channels, and most of the particles are deposited either directly offshore or alongshore on the Amazon shelf (Kuehl et al., 1986). River-derived particles dominate the particles in the Amazon inner shelf. More than 95% of the particles at its river mouth are silt- and clay-sized particles, consisting of quartz, illite, kaolinite, montmorillonite and feldspar (Gibbs, 1977; Martinelli et al., 1993). These sediments are mostly derived from the Andes, which contain low-grade uplifted Palaeozoic silicate sedimentary rocks and a few Tertiary and Quaternary sedimentary deposits (Gibbs, 1967; Dellinger et al., 2015). In the offshore transects, the suspended sediment concentration near the bottom reaches a maximum of more than 0.5 g/L (Gibbs, 1976) at a distance of 100 km from the river mouth. In the alongshore, the suspended particles can be transported northwestwards for around 600 km to reach approximately the location of sample 93MUC (Gibbs, 1976). Notably, the North Brazil Current and tides may cause resuspension of the ocean surface sediments and therefore create a fluid mud area (between the 10 m isobath and 20 m

isobath) with suspended sediment concentrations near the bottom greater than 10 g/L (Kuehl et al., 1986; Kineke et al., 1996).

2.2. Sampling

All water and sediment samples were collected from the Amazon estuary during RV Meteor Cruise M147 (process study GApr11 of the international GEOTRACES program) in April and May 2018 (Koschinsky et al., 2018). Twelve surface water samples (i.e., dissolved load) were collected in a transect across the mixing zone between the Amazon south channel and seawater, spanning a salinity range from 0.03 to 30.75 (Fig. 1, Table 1). Sample W56fish was collected by a towed fish surface water sampler, and the other 11 samples were collected by a Conductivity-Temperature-Depth (CTD) rosette. The water samples were filtered through 0.45 μm Nucleopore filters and acidified to approximately pH 2 using concentrated ultrapure distilled hydrochloric acid (HCl). The collection depths of the water samples were around 2–3 m, and further details are reported in Koschinsky et al. (2018). The temperature, salinity and pH were determined during sampling (Table 1). The concentration of Cl^- (mg/g) was calculated based on salinity, using salinity (‰) $= 1.80655 \times Cl^-$ (Wooster et al., 1969). The concentrations of dissolved NO_2^-, NO_3^- and SiO_4^{4-} were analysed by a SEAL QuAAtro continuous flow auto analyser on board (Koschinsky et al., 2018). The total alkalinity was analysed at GEOMAR (Helmholtz

Table 1
Chemistry and Li isotope compositions of the dissolved load samples.

Sample	Latitude	Longitude	Depth m	Salinity ‰	Temperature °C	pH	Na mg/L	Ca mg/L	Mg mg/L	K mg/L	Li µg/L	δ^7Li ‰	2sd ‰	SiO_4^{4-} µmol/L	NO_2^- µmol/L	NO_3^- µmol/L	Total alkalinity µmol/L
W66	00°03.27′N	48°42.45′W	2.4	0.03	28.3	7.23	17.34	5.95	3.06	1.63	0.87	23.7	0.3	150	0.2	12	387.7
W70	00°01.20′N	48°25.02′W	2.5	0.58	27.0	8.18	257.7	15.5	31.2	11.3	4.99	29.8	0.2	147		15	380.6
W69	00°01.07′N	48°25.11′W	2.4	1.03	27.8		412.7	26.7	82.5	26.2	11.0	31.0	0.2	141		16	
W71	00°01.72′N	48°11.60′W	2.3	3.67	27.5	8.20	1178	52.7	154	51.7	24.1	31.2	0.4	125	0.4	12	576.0
W80	01°16.00′N	48°16.71′W	2.9	6.58	28.1	8.65	1986	84.3	256	85.6	34.0	32.4	0.1	66.0	0.1	0.1	820.1
W72	00°34.07′N	47°59.88′W	2.7	7.01	28.2	8.53	2075	88.2	266	88.6	36.4	32.2	0.3	50.6	0.3	2.0	1275
W79	01°28.77′N	48°08.91′W	3.1	9.33	28.0	8.54	2925	124	379	126	49.1	32.8	0.0	67.8	0.1	0.4	1010
W78	01°34.06′N	48°05.65′W	3.1	12.31	27.9	8.47	4300	182	574	188	75.8	31.4	0.3	58.3	0.1	1.6	1187
W75	01°39.12′N	48°02.38′W	2.8	17.79	27.9		5466	222	680	228	99	30.4	0.4	44.2	0.1	0.6	
W74	01°44.22′N	47°58.39′W	3.0	20.51	28.1	8.29	6366	263	830	272	121	30.3	0.1	31.0	0.1	0.3	1612
W64	01°56.64′N	47°47.33′W	3.2	26.76	28.4	8.06	8103	314	1020	333	139	32.6	0.3	16.3	0.1	0.3	1867
W56fish	02°04.50′N	47°40.71′W	2.0	30.75	28.0		9320	362	1184	381	151	31.2	0.1	1.30	0.1	0.3	

Centre for Ocean Research Kiel) (Koschinsky et al., 2018).

Seven suspended particulate matter (SPM) samples were obtained from material that settled during filtering of 20 L CTD water samples. At GEOMAR, the SPM was rinsed into pre-cleaned containers using ultra-pure water (resistivity = 18.2 MΩ cm). The excess water was removed by siphoning after the SPM had visually settled and then centrifugation (3220g, 30 min). The SPM was freeze-dried at −52 °C and homogenised before an aliquot was sent to the LOGIC (London Geochemistry and Isotope Centre) laboratory. Notably, the finest particles attached on 0.45 µm Nucleopore filters after filtering were hard to remove. Thus, the finest particles, which take around 3% of bulk SPM samples by mass, were not included in the following analyses. According to their locations, the SPM samples are divided into two groups (Fig. 1, Table S2). Five SPM samples (i.e., SPM27–31) are from a small area with medium salinity, ranging from 1.78 to 12.89, in the north channel. The other two samples (SPM8s and SPM8d) were collected at the same location but at different water depths (16 m and 20 m, respectively) from near the Para River outflow, which is to the south of the Amazon River mouth.

Nine marine surface sediment samples were collected by Multi-corer (MUC), and the samples used here were the uppermost 0.5–2 cm of sediment from each core. At GEOMAR, the pore waters were removed by centrifugation (3220g, 30 min). The MUC samples were freeze-dried at −52 °C and homogenised before an aliquot was sent to the LOGIC laboratory. Further details are reported in Koschinsky et al. (2018). According to their locations (Fig. 1, Table S2), the MUC samples can be divided into three groups. In the first group, four samples (i.e., 24MUC, 85MUC, 117MUC and 41MUC) lie on an offshore transect across the north outflow. The five suspended load samples (i.e., SPM27–31) are also located in this transect between 24MUC and 85MUC. In the second group, two samples (i.e., 67MUC and 73MUC) lie on an offshore transect across the southern Amazon outflow. The third group consists of four samples (i.e., 85MUC, 89MUC, 108MUC and 93MUC) in an alongshore transect that starts on the north channel transect at 85MUC.

3. Analytical methods

3.1. Sequential chemical extractions

The solid samples, including SPM and MUC samples, were leached using a full sequential extraction procedure, modified from Tessier et al. (1979) and further detailed in Liu et al. (2022), in the order of exchangeable, carbonate, oxide, clay and residue. To assess precision, the USGS reference standard BCR-2 (Basalt, Columbia River; Wilson, 1998) and a basaltic river sand sample from Iceland (Pogge von Strandmann et al., 2019a) were leached as full-procedure references (Liu et al., 2022). A total procedural blank using the same leaching reagents was also applied to monitor the potential Li contamination. All procedures were conducted in the metal-free clean laboratories of LOGIC. The details on the reagent grade are in Liu et al. (2022).

A known mass (50 ± 2 mg) of each solid sample was weighed and reacted with the specific leaching reagents in the order of each step. The extracted leachate from each step was separated from the solid by centrifuging at 8200g for 3 min. Leachates (i.e., supernatants) were pipetted into pre-cleaned PFA vials, and the remaining solids were subjected to the next extraction step. The leachates in the PFA vials were dried down on a hotplate for elemental concentration and Li isotope analysis. The exchangeable phase was extracted using 1 M sodium acetate (NaOAc) at room temperature for 1 h with occasional agitation (Tessier et al., 1979; Pogge von Strandmann et al., 2019a). Then the carbonate phase was targeted with 1 M NaOAc buffered to pH 5 by acetic acid (HOAc) at room temperature for 5 h with occasional agitation (Tessier et al., 1979; Pogge von Strandmann et al., 2019b). Next the secondary oxide phase was extracted using 0.04 M hydroxylamine hydrochloride in 25% (v/v) HOAc at room temperature for 1 h with occasional agitation (Liu et al., 2022; Pogge von Strandmann et al., 2022). Then 0.6 M HCl was used to partly target the secondary clay phase at

room temperature for 1 h (Pogge von Strandmann et al., 2019a). We note that this HCl leach is primarily designed for examining the Li isotope composition of the secondary silicate phases rather than for quantitively extracting it. After the extraction of these phases, the remaining solids were totally dissolved (i.e., residue) by nitric acid (HNO$_3$, ca. 68% m/m) – hydrofluoric acid (HF, 47–51% m/m) – perchloric acid (HClO$_4$, 65–71% m/m), followed by HNO$_3$ (ca. 68% m/m), and then 6 M HCl in PFA vials on the hotplate (Pogge von Strandmann et al., 2019a).

For the water samples (i.e., dissolved load), a given volume of each sample was taken into PFA vials and dried down for further elemental concentration analysis and Li isotope analysis.

3.2. Li isotopes and elemental concentration analysis

The Li isotope compositions of the leachates and water samples were analysed by the Multi-Collector Inductively Coupled Plasma Mass Spectrometer (MC-ICP-MS, Nu Plasma 3) with a CETAC Aridus II™ Desolvating Nebulizer system in the LOGIC laboratory. The sample solutions for Li isotope analysis were purified through two cation-exchange columns using AG®50 W X-12 resin and 0.2 M HCl (Liu et al., 2022). Given that Li isotopes fractionate on the columns, the splits before and after the Li collection bracket were also collected and analysed for Li content to determine that all Li was collected. For most samples, the pre- and post-collect splits contained less than 0.1% Li out of the total Li, and for all samples, the Li content of the splits was insufficient to cause noticeable fractionation (Gou et al., 2020; Wilson et al., 2021). The Li isotope analysis used a sample-standard bracketing method, relative to the standard IRMM-016, which has an isotope ratio effectively identical to that of LSVEC (Jeffcoate et al., 2004; Pogge von Strandmann et al., 2019a). A 5 ng/g Li solution achieved a signal intensity of around 10 V (~100 pA) of ^{7}Li$^+$. The signal intensity of the blank (2% v/v HNO$_3$) was less than 0.02 ng/g. Each sample was measured a total of 3 times with 10 ratios for each time, and the mean value and 2sd are reported in Tables 1 and 2. Further analytical details are given in Pogge von Strandmann et al. (2019a) and Liu et al. (2022). The Li isotope data are reported as δ^7Li (‰) = ((^{7}Li/^{6}Li$_{sample}$)/(^{7}Li/^{6}Li$_{LSVEC}$) − 1) × 1000. Atlantic seawater was analysed as an "unknown" reference, yielding a δ^7Li value of 31.25 ± 0.45‰ (2sd, n = 8) during this study, identical to published values (Jeffcoate et al., 2004; Pogge von Strandmann et al., 2019a; Gou et al., 2020).

The elemental concentrations of the leachates and water samples were analysed by inductively coupled plasma optical emission spectroscopy (ICP-OES, Varian 720) and inductively coupled plasma mass spectrometry (ICP-MS, Agilent 7900) in the LOGIC laboratories. The concentrations of Ca, Mg, K and Na of all samples were analysed by ICP-OES. The concentrations of Fe, Al and Mn of the oxide leachates, clay leachates and dissolved residues were analysed by ICP-OES, whereas Fe, Al and Mn of the exchangeable and carbonate leachates were analysed by ICP-MS. The Li concentrations of all samples were analysed by ICP-MS. The standards NBS SRM 88A and SGR-1 were analysed as the reference materials to assess accuracy and precision, and the results are reported in Table S3. The relative standard deviations of individual analyses are better than 5% for all reported elements.

The reported elemental concentrations in the leachates of MUC and SPM samples are normalized to the total mass of leached solid according to Eq. (1). The composition of each element in bulk sediment samples is calculated as the sum of the concentration of that element in all phases, with an example for Li given as Eq. (2). In addition, the bulk δ^7Li values can be calculated based on the sum of the measured Li concentrations and isotope compositions for each fraction in the sequence, as shown in Eq. (3).

$$[X] \text{ in leachate} = X \text{ mass in leachate/solid mass}$$
$$= X \text{ concentration (by mass, measured)} \times \text{dilution factor}$$
$$\times \text{original leachate volume/solid mass}$$

$$(1)$$

$$[Li]_{bulk} = [Li]_{exchangeable} + [Li]_{carbonate} + [Li]_{oxide} + [Li]_{clay} + [Li]_{residue} \quad (2)$$

$$\delta^7 Li_{bulk} \times [Li]_{bulk} = \delta^7 Li_{exchangeable} \times [Li]_{exchangeable} + \delta^7 Li_{carbonate}$$
$$\times [Li]_{carbonate} + \delta^7 Li_{oxide} \times [Li]_{oxide} + \delta^7 Li_{clay}$$
$$\times [Li]_{clay} + \delta^7 Li_{residue} \times [Li]_{residue} \quad (3)$$

The bulk data calculated based on chemical extractions is compared to the bulk data measured by Spiegel et al. (2021) and Vosteen et al. (2022) in Supplementary Material S1.

4. Results

4.1. Dissolved samples in the Amazon estuary

The dissolved Li concentration increases through the Amazon estuary, displaying a linear relationship with salinity, ranging from 0.87 μg/L (at salinity of 0.03) to 151 μg/L (at salinity of 30.75) (Fig. 2a). The Li isotope composition (δ^7Li$_{diss}$) increases rapidly from 23.7‰ (at salinity of 0.03) to 31.0‰ (at salinity of 1.03), before increasing more slowly to peak at 32.8‰ (at salinity of 9.33) (Fig. 2b). Subsequently, there appear to be minor fluctuations before a slight decrease to 31.2‰ in the most offshore sample (at salinity of 30.75) (Fig. 2b). The concentration of major elements, such as Na, Mg, Ca and K, also increases in a linear relationship with salinity through the estuary (Table 1), indicating conservative mixing. The total alkalinity increases with salinity as well, whereas the SiO$_4^{4-}$ and NO$_3^-$ decrease with salinity. The pH increases from 7.2 (at salinity of 0.03) to around 8.5 at medium salinity (salinity of around 6–12) and decreases to around 8.0 at high salinity (Table 1).

4.2. Leachates of sediments

The elemental concentrations and Li isotopes in leachates of sediments are shown in Table 2. According to their elemental concentrations (i.e., Mg, K, Ca, Fe, Mn and Al), the leachates of the exchangeable pool, oxides and clays of the sediments (except sample 41MUC) are considered representative of the targeted phases (Supplementary Material S2). However, apart from the sample 41MUC, the operationally defined carbonate leachates of the other MUC and SPM samples are likely influenced by leaching of other phases, due to their low carbonate content (Supplementary Material S2).

For the exchangeable leachates, [Li]$_{exchangeable}$ increases from 0.08 μg/g at the river endmember to around 0.15 μg/g at low salinity, then increases again to around 0.25 μg/g at high salinity, and δ^7Li$_{exchangeable}$ also increases from 5.7 to 17.0‰ through the transect of the north channel (Fig. 3). In the alongshore transect, [Li]$_{exchangeable}$ remains constant at around 0.3 μg/g, and the δ^7Li$_{exchangeable}$ values are within a relatively small range of 16.9–18.6‰. Similarly, in the north channel transect, [Li]$_{oxide}$ increases from 0.05 to 0.37 μg/g with increasing salinity, and the δ^7Li$_{oxide}$ values increase from −2.8‰ in the riverine endmember to 5.2‰ at a salinity of 20. In the alongshore transect, the [Li]$_{oxide}$ generally remains stable at 0.33–0.37 μg/g and the δ^7Li$_{oxide}$ values range from 4.4 to 6.1‰. The [Li]$_{clay}$ also increases from 0.19 to 0.88 μg/g in the north channel transect, and the δ^7Li$_{clay}$ values generally increase from 0.2‰ to around 5.0‰. In the alongshore transect, the [Li]$_{clay}$ generally remains stable at 0.88–1.21 μg/g, and the δ^7Li$_{clay}$ ranges from 4.5 to 5.4‰. The leaching residue of the sediment samples contains more than 94% of the Li in bulk sediments so that the [Li]$_{bulk}$ and δ^7Li$_{bulk}$ are dominated by the residue. In the north channel transect, [Li]$_{bulk}$ is 32.6 μg/g in the river endmember, remains stable at around

Table 2
Elemental concentrations and Li isotope compositions for different phases of the MUC and SPM samples.

Sample	δ7Li ‰	2sd ‰	Li[1] µg/g	Ca[1] mg/g	Mg[1] mg/g	K[1] mg/g	Fe[1] mg/g	Mn[1] mg/g	Al[1] mg/g	Si[2] mg/g
24MUC exchangeable	5.7	0.0	0.08	0.80	0.51	0.12	0.008	0.004	0.002	
SPM27 exchangeable	9.7	0.1	0.11	0.71	1.17	0.26	0.005	0.002	0.001	
SPM28 exchangeable	9.7	0.3	0.14	0.85	1.41	0.35	0.009	0.002	0.002	
SPM29 exchangeable	11.3	0.3	0.15	0.82	1.37	0.40	0.006	0.001	0.002	
SPM30 exchangeable	14.3	0.4	0.16	0.68	1.18	0.48	0.004	0.001	0.001	
SPM31 exchangeable	13.5	0.1	0.15	0.68	1.19	0.48	0.005	0.001	0.001	
85MUC exchangeable	18.5	0.3	0.31	0.81	1.39	1.15	0.003	0.003	0.002	
117MUC exchangeable	16.4	0.3	0.24	1.11	1.16	0.95	0.005	0.003	0.002	
41MUC exchangeable	17.0	0.5	0.26	1.54	1.34	1.06	0.006	0.001	0.001	
89MUC exchangeable	17.5	0.2	0.29	0.93	1.62	0.99	0.007	0.006	0.001	
108MUC exchangeable	18.6	0.1	0.31	1.19	1.81	1.17	0.004	0.004	0.001	
93MUC exchangeable	16.9	0.3	0.34	1.63	1.87	1.45	0.006	0.004	0.002	
67MUC exchangeable	2.1	0.3	0.08	2.17	0.34	0.12	0.009	0.004	0.001	
73MUC exchangeable	19.8	0.2	0.26	1.32	1.93	1.17	0.013	0.002	0.001	
SPM8s exchangeable	16.8	0.3	0.28	1.22	1.74	0.81	0.005	0.002	0.001	
SPM8d exchangeable	16.6	0.5	0.27	1.38	1.76	0.79	0.007	0.001	0.001	
24MUC carbonate[3]	−0.4	0.3	0.06	0.22	0.09	0.04	0.04	0.03	0.02	
SPM27 carbonate[3]	0.4	0.0	0.10	0.24	0.23	0.10	0.03	0.03	0.02	
SPM28 carbonate[3]	0.6	0.1	0.11	0.20	0.26	0.13	0.03	0.03	0.02	
SPM29 carbonate[3]	1.4	0.2	0.13	0.43	0.30	0.17	0.02	0.03	0.02	
SPM30 carbonate[3]	4.6	0.2	0.14	0.27	0.29	0.18	0.02	0.02	0.02	
SPM31 carbonate[3]	5.2	0.2	0.16	0.27	0.41	0.22	0.03	0.02	0.02	
85MUC carbonate[3]	8.2	0.2	0.38	0.34	0.53	0.43	0.08	0.09	0.03	
117MUC carbonate[3]	8.4	0.2	0.33	4.29	0.61	0.37	0.12	0.30	0.02	
41MUC carbonate	14.9	0.3	0.33	66.9	0.79	0.36	0.09	0.02	0.01	
89MUC carbonate[3]	10.1	0.3	0.32	0.39	0.55	0.37	0.02	0.09	0.02	
108MUC carbonate[3]	10.4	0.4	0.36	1.26	0.66	0.46	0.05	0.24	0.02	
93MUC carbonate[3]	8.5	0.1	0.44	0.98	0.60	0.55	0.09	0.20	0.02	
67MUC carbonate[3]	−5.0	0.4	0.06	0.54	0.06	0.04	0.09	0.05	0.02	
73MUC carbonate[3]	10.4	0.3	0.29	1.68	0.69	0.46	0.04	0.06	0.02	
SPM8s carbonate[3]	6.8	0.3	0.25	0.50	0.51	0.34	0.03	0.05	0.02	
SPM8d carbonate[3]	6.7	0.4	0.27	0.73	0.53	0.31	0.03	0.04	0.02	
24MUC oxide	−2.8	0.1	0.05	0.10	0.02	0.01	0.47	0.17	0.08	
SPM27 oxide	0.3	0.2	0.12	0.14	0.07	0.06	0.72	0.20	0.16	
SPM28 oxide	−0.7	0.2	0.12	0.11	0.07	0.05	0.59	0.19	0.09	
SPM29 oxide	0.8	0.2	0.15	0.12	0.09	0.08	0.69	0.21	0.19	
SPM30 oxide	2.4	0.4	0.16	0.15	0.10	0.07	0.74	0.24	0.12	
SPM31 oxide	2.0	0.3	0.19	0.14	0.13	0.11	0.76	0.23	0.22	
85MUC oxide	4.4	0.3	0.33	0.12	0.16	0.13	0.95	0.03	0.11	
117MUC oxide	5.2	0.2	0.37	0.62	0.20	0.14	1.53	0.20	0.12	
41MUC oxide[4]	19.0	0.3	0.59	121	0.60	0.15	0.38	0.26	0.18	
89MUC oxide	4.7	0.4	0.33	0.14	0.17	0.13	0.84	0.22	0.12	
108MUC oxide	6.1	0.2	0.36	0.25	0.20	0.18	1.02	0.43	0.18	
93MUC oxide	4.7	0.0	0.37	0.20	0.18	0.18	1.14	0.21	0.11	
67MUC oxide	−6.2	0.1	0.04	0.14	0.02	0.02	0.97	0.39	0.10	
73MUC oxide	6.1	0.2	0.15	0.26	0.12	0.11	0.65	0.10	0.09	
SPM8s oxide	4.3	0.3	0.24	0.18	0.13	0.14	0.95	0.30	0.17	
SPM8d oxide	4.1	0.1	0.20	0.18	0.12	0.10	0.73	0.24	0.09	
24MUC clay	0.2	0.2	0.19	0.40	0.09	0.02	2.04	0.06	0.57	
SPM27 clay	2.8	0.2	0.42	0.33	0.22	0.05	3.39	0.11	0.94	
SPM28 clay	2.8	0.3	0.51	0.32	0.25	0.06	3.64	0.15	1.02	
SPM29 clay	3.3	0.0	0.52	0.35	0.28	0.06	3.70	0.16	1.03	
SPM30 clay	4.0	0.2	0.60	0.35	0.33	0.08	4.29	0.18	1.17	
SPM31 clay	3.7	0.1	0.68	0.35	0.35	0.09	4.20	0.18	1.14	
85MUC clay	5.4	0.4	0.88	0.34	0.43	0.13	3.33	0.06	1.02	
117MUC clay	4.7	0.0	0.87	0.62	0.49	0.12	4.20	0.10	1.01	
41MUC clay	5.0	0.0	0.71	5.78	0.29	0.09	1.75	0.02	0.66	
89MUC clay	4.5	0.0	0.93	0.25	0.45	0.12	3.78	0.19	1.06	
108MUC clay	5.1	0.1	0.86	0.32	0.46	0.14	3.75	0.24	1.10	
93MUC clay	5.2	0.3	1.21	0.38	0.58	0.15	5.02	0.22	1.00	
67MUC clay	−0.3	0.3	0.22	0.49	0.11	0.02	4.01	0.16	0.77	
73MUC clay	4.5	0.3	0.60	0.37	0.35	0.15	4.54	0.17	1.02	
SPM8s clay	4.2	0.4	0.68	0.29	0.40	0.13	5.51	0.26	1.25	
SPM8d clay	4.1	0.4	0.65	0.35	0.40	0.14	5.02	0.28	1.19	
24MUC residue	−1.6	0.0	32.2	5.35	5.94	14.9	28.3	0.34	59.6	
SPM27 residue	−2.4	0.3	56.4	2.98	8.62	21.4	38.5	0.35	93.8	
SPM28 residue	−2.0	0.1	61.5	2.79	9.21	21.6	42.3	0.39	101	
SPM29 residue	−1.9	0.3	62.4	3.20	9.48	22.2	43.4	0.41	104	
SPM30 residue	−2.6	0.2	61.7	2.70	9.53	22.8	43.6	0.41	101	
SPM31 residue	−1.5	0.5	64.2	3.26	9.84	23.0	45.3	0.41	107	
85MUC residue	−2.0	0.2	56.3	2.98	8.64	19.1	41.8	0.37	91.1	
117MUC residue	−1.7	0.3	49.1	3.91	8.21	18.5	37.0	0.33	85.0	
41MUC residue	−1.8	0.3	31.5	2.70	4.60	6.42	21.0	0.13	47.5	

Table 2 (*continued*)

Sample	δ^7Li ‰	2sd ‰	Li[1] µg/g	Ca[1] mg/g	Mg[1] mg/g	K[1] mg/g	Fe[1] mg/g	Mn[1] mg/g	Al[1] mg/g	Si[2] mg/g
89MUC residue	−2.3	0.2	66.0	1.97	9.99	21.4	47.7	0.44	105	
108MUC residue	−2.7	0.1	61.6	2.07	9.47	19.6	46.9	0.43	98.8	
93MUC residue	−2.6	0.3	67.8	2.09	10.2	19.7	46.5	0.42	104	
67MUC residue	−1.9	0.1	42.7	5.37	7.33	17.5	34.1	0.35	75.9	
73MUC residue	−1.6	0.1	60.6	2.32	8.73	19.3	45.3	0.39	101	
SPM8s residue	−2.3	0.5	65.0	2.21	9.44	20.6	48.8	0.43	111	
SPM8d residue	−2.6	0.1	71.3	2.01	10.4	22.6	54.3	0.50	121	
24MUC bulk[5]	−1.6		32.6	6.87	6.65	15.1	30.8	0.60	60.2	375
SPM27 bulk[5]	−2.3		57.1	4.40	10.3	21.9	42.7	0.68	95.0	334
SPM28 bulk[5]	−2.0		62.4	4.27	11.2	22.2	46.5	0.76	102	321
SPM29 bulk[5]	−1.8		63.3	4.92	11.5	22.9	47.8	0.81	106	316
SPM30 bulk[5]	−2.4		62.7	4.14	11.4	23.6	48.7	0.85	102	319
SPM31 bulk[5]	−1.4		65.6	4.70	11.9	23.9	50.3	0.84	108	312
85MUC bulk[5]	−1.7		58.2	4.60	11.1	20.9	46.2	0.55	92.3	331
117MUC bulk[5]	−1.4		50.9	10.6	10.7	20.0	42.8	0.94	86.1	335
41MUC bulk[5]	−1.0		33.4	197	7.6	8.08	23.2	0.43	48.3	269
89MUC bulk[5]	−2.0		67.9	3.67	12.8	23.1	52.4	0.94	107	312
108MUC bulk[5]	−2.3		63.5	5.09	12.6	21.6	51.7	1.34	100	318
93MUC bulk[5]	−2.2		70.2	5.29	13.4	22.1	52.8	1.05	105	312
67MUC bulk[5]	−1.9		43.1	8.71	7.86	17.7	39.2	0.95	76.8	351
73MUC bulk[5]	−1.3		61.9	5.96	11.8	21.2	50.5	0.73	102	318
SPM8s bulk[5]	−2.1		66.4	4.40	12.2	22.0	55.3	1.04	113	305
SPM8d bulk[5]	−2.4		72.7	4.65	13.2	24.0	60.1	1.06	123	291

[1] Elemental concentrations report the mass of the element in the leachate per gram of solid leached (Eq. (1)).
[2] Si concentration in bulk sediments is calculated (see Section 5.3).
[3] The nominal carbonate phase is strongly influenced by other phases (see Supplementary Material S2).
[4] The oxide phase of 41MUC is influenced by carbonates (see Supplementary Material S2).
[5] The element concentrations and Li isotopes are calculated using Eqs. (2) and (3).
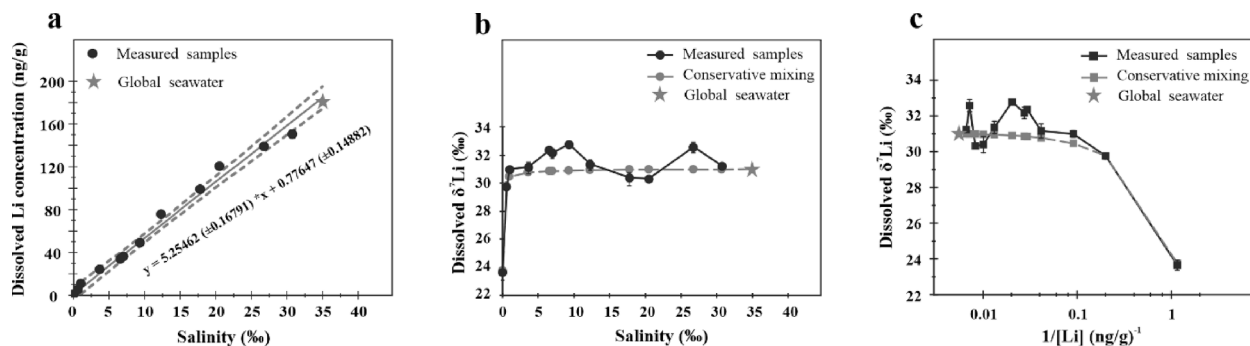
Fig. 2. Dissolved load Li concentrations and Li isotope compositions. (a) Relationship between dissolved Li concentrations and salinity. The grey line is a fit to the data, and the dashed lines represent confidence levels of p less than 0.05. The error bars of Li concentration represent analytical uncertainty (sd). Invisible error bars are hidden by sample symbols. (b) Relationship between dissolved Li isotope compositions and salinity. (c) Relationship between dissolved Li isotope compositions and Li concentrations (plotted as 1/[Li]). In panels (b) and (c), the dashed grey line is a conservative mixing line (Section 5.1.1). The error bars of δ^7Li represent analytical uncertainty (2sd). Invisible error bars are hidden by sample symbols.

63 µg/g at medium salinity and decreases to 33.4 µg/g in the offshore sediment 41MUC. Although the [Li]$_{bulk}$ at medium salinity is approximately double that of the river endmember, the δ^7Li$_{bulk}$ lies in a narrow range from −2.4 to −1.0‰ for all samples without showing a clear relationship with salinity. In the alongshore transect, [Li]$_{bulk}$ ranges from 58.2 to 70.2 µg/g and δ^7Li$_{bulk}$ ranges from −2.3 to −1.7‰.

5. Discussion

5.1. Behaviour of Li and its isotopes in the Amazon estuary

5.1.1. Dissolved Li during mixing of river water and seawater

In the transect of the Amazon south channel, the dissolved Li concentrations of surface water samples generally lie within the conservative mixing line between river water and seawater (Fig. 2a), which agrees with previous studies (Stoffyn-Egli, 1982; Colten and Hanor, 1984; Brunskill et al., 2003; Pogge von Strandmann et al., 2008; Murphy et al., 2014; Yang et al., 2021). Thus, the dissolved Li generally shows

conservative behaviour in the Amazon estuary, although the measured Li concentrations of some samples deviate slightly from the precise theoretical mixing line, as also reported by previous studies (Pogge von Strandmann et al., 2008; Yang et al., 2021). The slight deviations may be analytical (i.e., analytical precision of salinity or Li concentration measurements), but they are more likely due to mixing variation related to influences of waves and/or tide, or dissolution/incorporation by particles, discussed in Section 5.1.3.

Based on conservative binary mixing of river water and seawater and mass balance, the theoretical conservative mixing of Li isotopes (i.e., δ^7Li$_{conservative}$) can be calculated using Eqs. (4)–(9) (Fig. 2b and c).

$$[Li]_{measured} = [Li]_{riverwater} \times FV_{riverwater} + [Li]_{seawater} \times FV_{seawater} \quad (4)$$

$$FV_{riverwater} = V_{riverwater}/V_{total} = V_{riverwater}/(V_{riverwater} + V_{seawater}) \quad (5)$$

$$FV_{seawater} = V_{seawater}/V_{total} = V_{seawater}/(V_{riverwater} + V_{seawater}) \quad (6)$$

ARTICLE IN PRESS

C.-Y. Liu et al.   Geochimica et Cosmochimica Acta xxx (xxxx) xxx
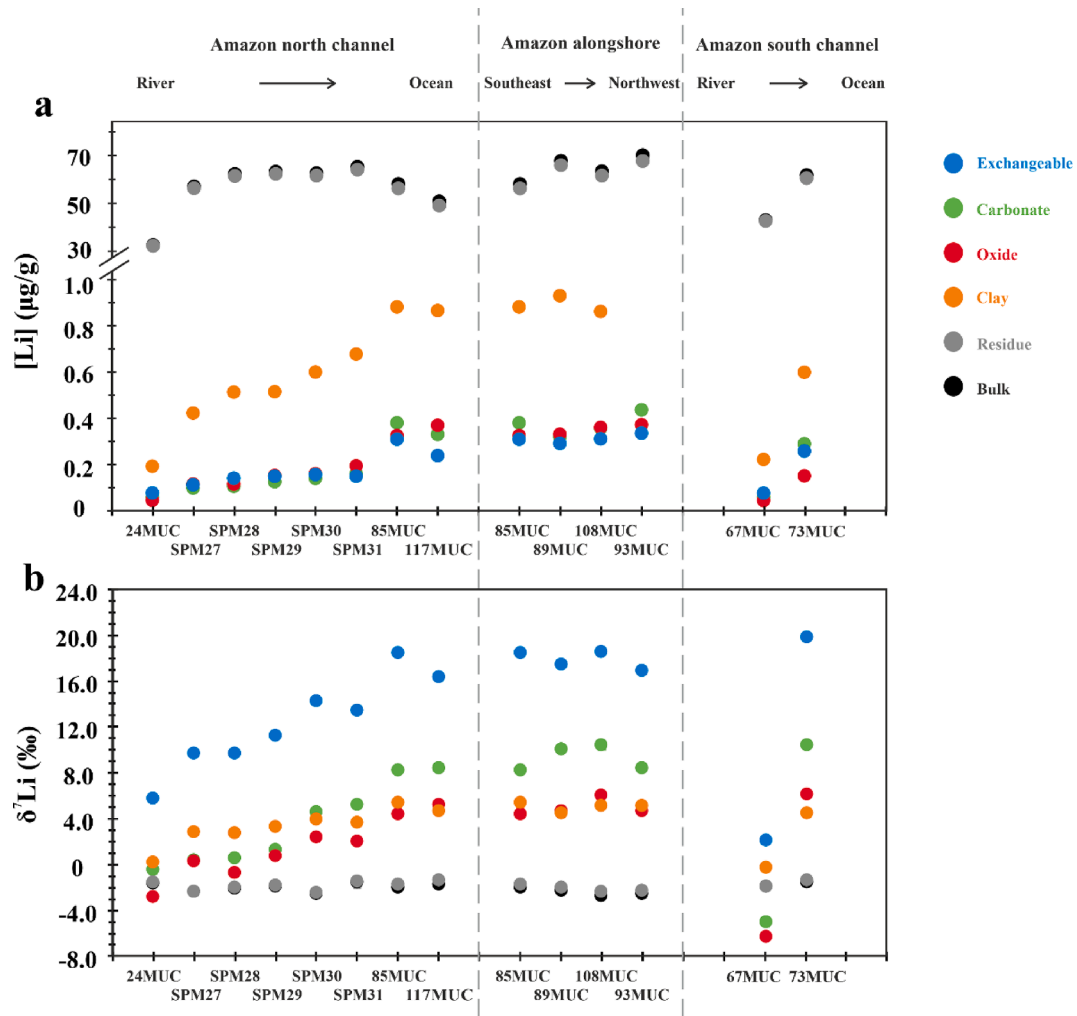
Fig. 3. Lithium concentrations and isotope compositions for different phases of the sediment samples. (a) Lithium concentrations for different phases of the sediment samples. Note that the [Li] axis is broken between 1.0 and 30 μg/g. (b) Lithium isotope compositions for different phases of the sediment samples. Note that the phases are separated based on sequential leaching, and that the carbonate phase is probably influenced by the leaching of phases other than carbonate (Supplementary Material S2). The data labelled 'bulk' represent the sum of all fractions, based on Eqs. (2) and (3). Where the black data points are not visible, they are hidden by the grey data points because of their similar values. The directions from river to ocean in the Amazon north channel transect and south channel transects are labelled above panels (a) and (b). The southeast end of the alongshore transect is near the river endmember. The salinities of the water samples corresponding to the sediment samples are shown in Table S2. Note that data from samples 41MUC, SPM8s and SPM8d are not shown.

$$FLi_{riverwater} = FV_{riverwater} \times ([Li]_{riverwater}/[Li]_{measured}) \qquad (7)$$

$$FLi_{seawater} = FV_{seawater} \times ([Li]_{seawater}/[Li]_{measured}) \qquad (8)$$

$$\delta^7Li_{conservative} = \delta^7Li_{riverwater} \times FLi_{riverwater} + \delta^7Li_{seawater} \times FLi_{seawater} \qquad (9)$$

In those equations, $[Li]_{measured}$ is the measured Li concentration of each dissolved sample. $[Li]_{seawater}$ and $\delta^7Li_{seawater}$ represent the Li concentration (180 μg/L) and the Li isotope composition (31.0‰) of the modern global ocean, respectively (Jeffcoate et al., 2004; Tomascak et al., 2016). $[Li]_{riverwater}$ and $\delta^7Li_{riverwater}$ are the Li concentration (0.87 μg/L) and Li isotope composition (23.7‰) of the Amazon estuarine river, respectively, based on the riverine endmember sampled at the south channel (i.e., sample W66). $V_{riverwater}$ and $V_{seawater}$ are the volume of the Amazon River water and seawater contributed to each sample, respectively, based on conservative mixing of Li concentrations (similar to results based on Na or Cl concentrations). $FV_{riverwater}$ and $FV_{seawater}$ refer to the mass fraction of the water volume contributed by the Amazon River and seawater, respectively. $FLi_{riverwater}$ and $FLi_{seawater}$ refer to the mass fraction of the Li derived from the Amazon River water and seawater, respectively.

Based on the mixing calculation, the theoretical dissolved δ^7Li value increases to greater than 30.0‰ at a very low salinity of 1.03 (equivalent to sample W69) (Fig. 2b and c), which is due to the significantly higher Li concentrations of seawater compared to river water. At a salinity of 1.03, seawater contributes around 92% of the total dissolved Li (i.e., $FLi_{seawater}$), although the volume of seawater only comprises around 4% of the total water volume (i.e., $FV_{seawater}$). At a salinity of 6.58, the theoretical conservative mixing-derived δ^7Li value reaches 30.8‰, which is within the range of modern seawater, because the seawater dominates the Li in the dissolved samples (i.e., $FLi_{seawater} > 98\%$). As shown in Fig. 2b, the measured dissolved Li isotopes ($\delta^7Li_{measured}$) lie on the mixing line, suggesting conservative mixing, at low salinity area. However, from a salinity of 6.58–9.33, the $\delta^7Li_{measured}$ is around 1–2‰ higher than the mixing line. The higher $\delta^7Li_{measured}$ may imply Li uptake by particles, although there is no significant decrease in dissolved Li concentration (Pogge von Strandmann et al., 2008; Murphy et al., 2014; Yang et al., 2021). At salinities higher than 10, the $\delta^7Li_{measured}$ appears consistent with conservative mixing (with the exception of one sample with a salinity of 26.76 that shows a higher $\delta^7Li_{measured}$). In general, the high seawater Li concentrations may hinder the observation of Li isotope fractionation during clay formation (Pogge von Strandmann et al., 2008;

Murphy et al., 2014; Yang et al., 2021), which is explored further in Section 5.1.3.

5.1.2. Behaviour of Li in the sediment samples

In general, both [Li] and δ^7Li values in the leachates of the sediment samples increase through the estuary (Fig. 3). In the exchangeable pool, [Li]$_{exchangeable}$ increases from 0.08 µg/g to around 0.25 µg/g and δ^7Li$_{exchangeable}$ increases from 5.7 to 17.0‰ along the north channel transect. Furthermore, δ^7Li$_{exchangeable}$ in those samples shows a linear relationship with 1/[Li]$_{exchangeable}$, supporting the addition of Li to the exchangeable pool and allowing the δ^7Li composition of this endmember to be calculated as 21.7 ± 2.8‰ (Fig. 4). Assuming derivation from seawater, the fractionation factor ($\alpha_{exchangeable-seawater}$) between the exchangeable pool and seawater is calculated as 0.9907 ± 0.0028 (2sd), which is similar to the fractionation factor calculated in previous experimental studies and natural settings (0.99 in Wimpenny et al., 2010a; 0.988 in Pogge von Strandmann et al., 2019a; 0.999 in Hindshaw et al., 2019; 0.992 in Li and Liu, 2020). In the alongshore transect, [Li]$_{exchangeable}$ remains constant at around 0.3 µg/g, and the δ^7Li$_{exchangeable}$ values are within a small range from 17.0 to 18.6‰ (Fig. 3), which gives an $\alpha_{exchangeable-seawater}$ value of 0.9860–0.9876, similar to the previous calculation. Overall, the consistent Li concentrations and isotope compositions in those samples may imply that the maximum amount of Li that can be adsorbed on exchangeable sites by the sediments in the Amazon plume is around 0.3 µg/g (i.e., 12.5 ± 1.0 ng/m^2 with the surface area of MUC samples at alongshore transect as 24 ± 2.0 m^2/g, Table S2), which is less than 0.5% of the Li in the bulk sediments.

For the oxide fraction, the [Li]$_{oxide}$ increases from 0.05 to 0.37 µg/g with salinity in the north channel transect (except for sample 41MUC; Supplementary Material S2), whereas the δ^7Li$_{oxide}$ values also increase from −2.8 to 5.2‰ (Fig. 3), and they show a linear relationship with 1/[Li]$_{oxide}$ (Fig. 4). In this case, the empirical value for the endmember is 4.4 ± 2.0‰, which implies that oxides take up Li from seawater with a fractionation factor ($\alpha_{oxide-seawater}$) of 0.9734 ± 0.0020 (2sd). This value is similar to that reported in some studies (Wimpenny et al., 2010b; Hindshaw et al., 2018; Liu et al., 2022; Pogge von Strandmann et al., 2022) but is a smaller value (implying greater fractionation) than reported in some other studies (Pistiner and Henderson, 2003; Chan and Hein, 2007; Li et al., 2020). To avoid a specific sample dominating the fit, a fitting line without 24MUC (the riverine endmember) is tested, as the empirical value for δ^7Li$_{oxide}$ is 7.1 ± 1.8‰, giving an $\alpha_{oxide-seawater}$ of

Fig. 4. δ^7Li versus 1/[Li] for the different phases of the sediment samples in the north channel transect. Data are plotted as filled circles. Solid blue, red and orange lines are the best-fit lines for the exchangeable, oxide and clay phases, respectively, and dashed lines represent the boundaries of the fits with p less than 0.05. Data from sample 41MUC are not included for the oxide and clay phases, because of the influence of carbonate (Supplementary Material S2).

0.9779 ± 0.0018 (2sd), which is similar to the previous value. In the alongshore transect, the Li concentrations are stable at around 0.35 µg/g and δ^7Li values vary in a narrow range from 4.4 to 6.1‰, giving an $\alpha_{oxide-seawater}$ of 0.9734–0.9751.

Similarly, for the clay fraction, δ^7Li$_{clay}$ and 1/[Li]$_{clay}$ also have a linear relationship (Fig. 4), with [Li]$_{clay}$ increasing from 0.20 to 0.88 µg/g in the north channel transect (except for sample 41MUC; Supplementary Material S2), whereas δ^7Li$_{clay}$ increases from 0.2‰ to around 5.0‰. This observation implies the uptake of Li by clays in saline water, with an empirical δ^7Li endmember of 5.7 ± 1.0‰ (Fig. 4), and hence a fractionation factor ($\alpha_{clay-seawater}$) between clay phases and seawater of 0.9747 ± 0.0010 (2sd). This fractionation factor is close to the low end (higher fractionation) of the range reported in previous studies from 0.9950 to 0.9763 (Pogge von Strandmann et al., 2008, 2020; Andrews et al., 2020). In the alongshore transect, [Li]$_{clay}$ stabilises at around 1.0 µg/g and δ^7Li$_{clay}$ values are from 4.5 to 5.4‰, giving an $\alpha_{clay-seawater}$ of 0.9735–0.9744.

Among the exchangeable, oxide and clay phases, the concentrations of Li retained in exchangeable and oxide phases in the bulk sediments are similar at 0.3 µg/g, which is less than Li retained in the clay phases (0.7–1.0 µg/g). Furthermore, given that the clay leaching method is designed to obtain the Li isotope composition of the clay phase rather than to quantitatively leach the entire clay phase (Section 3.1, Liu et al., 2022), the amount of Li removed into the clay phase may be underestimated in this case (Supplementary Material S4). Besides, based on the element concentrations in leachates, it appears that the inadvertent leaching of the clay can influence oxide leachates (Supplementary Material S4; Liu et al., 2022). However, because of the similar $\alpha_{oxide-seawater}$ and $\alpha_{clay-seawater}$, the oxide and clay phase can be combined. Thus, the amount of Li retained in secondary mineral lattice phases (i.e., oxide and clay) is estimated as comprising more than 90% of the total Li removal (i.e., exchangeable, oxide and clay) in the Amazon estuary, as also reported from weathering experiments (Pogge von Strandmann et al., 2019a). These secondary mineral lattice phases remove Li from saline solutions with larger isotopic fractionation than the exchangeable pool in the Amazon estuary.

5.1.3. Fractionation modelling of Li removal into sediments

As discussed previously, the exchangeable, oxide and clay phases of the sediments appear to remove Li from the saline water with accompanying isotopic fractionation in the Amazon estuary, especially along the offshore transect. In the dissolved load, [Li]$_{measured}$ is indistinguishable from conservative mixing (Fig. 2a), but the δ^7Li$_{measured}$ values are slightly higher than δ^7Li$_{conservative}$ values, especially at medium salinity (Fig. 2b and c). A Li isotope fractionation model (Supplementary Material S4, Table S4) confirms that the removal of Li into sediments can lead to elevated dissolved δ^7Li$_{measured}$ values without detectable dissolved [Li]$_{measured}$ decreases (Fig. 5). In the model, the fraction of Li that remains in the dissolved load after sediment removal (f) is calculated from Eq. (10).

$$f = 1 - SSC \times [Li]_{sediment\ added}/[Li]_{conservative} \qquad (10)$$

Here, the [Li]$_{sediment\ added}$ is the mass of Li per gram that is gained by the sediments and the [Li]$_{conservative}$ is the dissolved Li concentration by conservatively mixing with river water and seawater. The SSC is the suspended sediment concentration. The SSC of SPM27–31 samples ranges from 0.26 to 0.59 g/L (Table S2). Generally, in the Amazon estuary, the SSC in the surface layer (less than 3 m) is greater than 0.2 g/L just off the river mouth, greater than 0.5 g/L in the mud resuspension area in the middle of the estuary, but less than 0.1 g/L towards the end of the estuary (Gibbs, 1976; Kineke et al., 1996). The average SSC in the Amazon River estuary has also been calculated as 0.19 g/L based on the Amazon River annual discharge of water and particle load (Gaillardet et al., 1999; Milliman and Farnsworth, 2011). To examine the general situation, the estimated range for SSC is 0.1–1.0 g/L in the model.
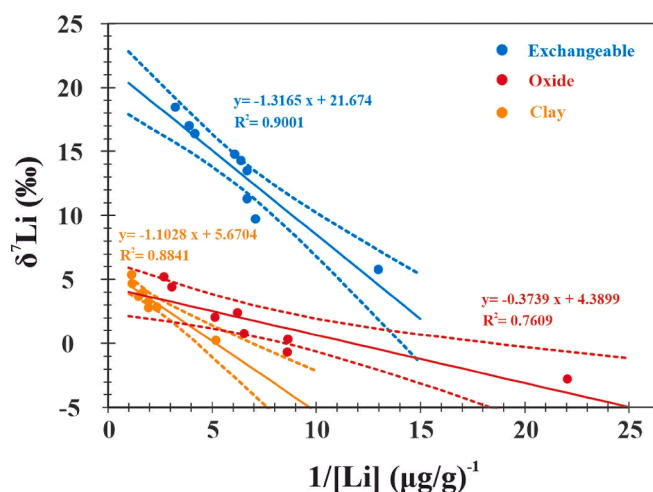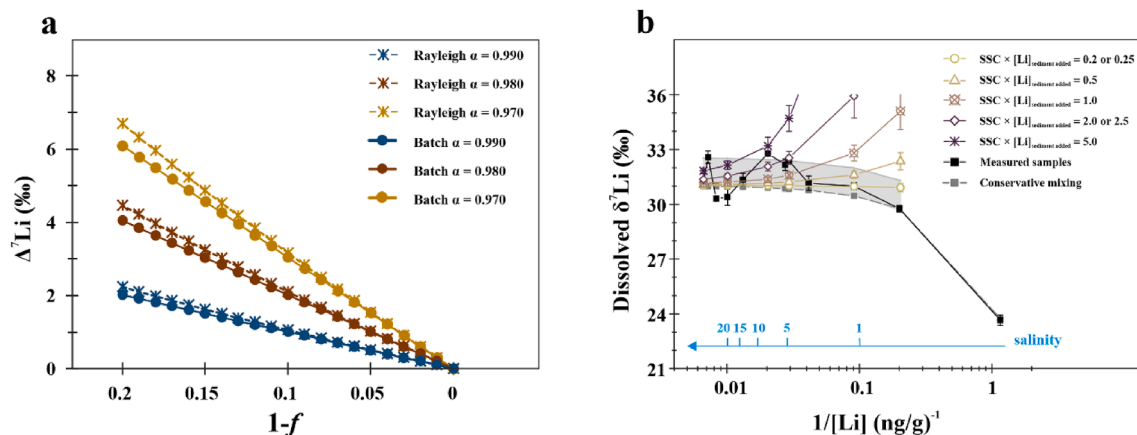
Fig. 5. Modelled Li isotope fractionation by sediment removal. (a) Modelled relationship between the fraction of Li loss and the Li isotope fractionation for the dissolved load (i.e., after Li loss compared to before Li loss in dissolved load). The term f is the fraction of Li remaining in the dissolved load after Li uptake by sediment (Section 5.1.3 and Supplementary Material S4). Curves are plotted for Rayleigh and batch models and for different fractionation factors (α). (b) Dissolved Li concentrations and Li isotope compositions for measured samples (black symbols and line) compared to a conservative mixing curve (grey dashed line) and to modelled results (coloured open symbols). The blue scale indicates the corresponding salinity. The grey shaded region shows the limitation on Li loss of the dissolved Li (<5%) at the corresponding Li concentration (Supplementary Material S4). SSC is the suspended sediment concentration, and [Li]$_{sediment\ added}$ is the mass of Li per gram that is gained by sediments. The uncertainty (sd) of δ⁷Li for the points from fractionation modelling stems from uncertainty in α (i.e., 0.975 ± 0.005) and the difference between Rayleigh and batch models. The modelled points in the scenario with SSC × [Li]$_{sediment\ added}$ = 0.2 and 0.25 are combined, as well as the scenario with SSC × [Li]$_{sediment\ added}$ = 2.0 and 2.5, and their differences are included in uncertainty.

The measured data and modelling results are compared in Fig. 5. At very low salinity (0–0.5), there is little resolvable Li uptake by particles. At low salinity (1–7), although no significant Li isotope fractionation is observed, Li removal could be approximately 1–2%, considering approximately 0.2 g/L SSC (Gibbs, 1976) and 1–2 μg/g [Li]$_{sediment\ added}$ (SSC × [Li]$_{sediment\ added}$ as 0.2–0.5). At medium salinity (7–18), Li removal is enhanced up to 5%, linked to 0.5 g/L SSC (Gibbs, 1976) and 4–5 μg/g [Li]$_{sediment\ added}$ (SSC × [Li]$_{sediment\ added}$ up to 2.5). In this case, the Li removal can elevate the dissolved δ⁷Li$_{measured}$ values by 1–2‰ higher than δ⁷Li$_{conservative}$, without leading to a resolvable decrease in the dissolved Li concentration. At medium salinity, there is an area affected by resuspension of mud particles due to the tides (Kineke et al., 1996). The particles in this area show higher biogenic silica concentrations, finer grain size and longer interaction time with the dissolved load (Gibbs, 1967; DeMaster et al., 1983; Kineke et al., 1996), which likely enhances Li removal but is not expected to affect equilibrium fractionation factors. At higher salinity (>20), due to the high dissolved Li concentrations and low SSC, particle Li uptake could only comprise a relatively small fraction of the Li budget, which would not cause resolvable Li isotope fractionation in the dissolved load. Overall, for the Amazon estuary as a whole, based on the assumption that 70% of the particles deposited at low and medium salinity area (Kineke et al., 1996), we estimate that the average [Li]$_{sediment\ added}$ is 3–4 μg/g.

5.1.4. Estimation of the Li removal flux during estuarine processes

An estuary model is used to calculate the Li budget accumulated through the whole Amazon estuary (Supplementary Material S5). Here, the estuary is assumed to be at steady state, with the exchange of material (i.e., water and particles) between the river, estuary and ocean being stable with time, and the geochemistry and particle distribution remaining constant with time.

For the dissolved load in the estuary, the inputs of dissolved Li are from river water, seawater, and sediment dissolution. However, the sediment samples exhibit net Li removal from the dissolved load rather than Li input, as also observed in basalt-water interaction experiments (Pogge von Strandmann et al., 2019a), indicating that the Li input from sediment dissolution is more than offset by Li uptake by secondary minerals. In other words, the output of dissolved Li in the model is sediment uptake. The total water volume and the seawater-contributed volume can be calculated according to the mass of dissolved Li input

from river water and seawater (Fig. 6, Table S5). According to the fractionation model (Section 5.1.3), the Li removal at medium salinity is relatively higher relative to low and high salinity. Thus, the fraction of Li remaining in the dissolved load after sediment removal from the start of the Amazon estuary to the corresponding salinity point is calculated as accumulated f (Σf) in Eq. (11) (details in Supplementary Material S5).

$$\sum f = \int f \times [Li]_{conservative} dV_{total} / \int [Li]_{conservative} \, dV_{total} \qquad (11)$$

The V_{total} is the total volume of the Amazon River water and seawater (Section 5.1.1). [Li]$_{conservative}$ is the dissolved Li concentration according to the conservative mixing line between river water and seawater (Section 5.1.3). The f is the fraction of Li that remains in the dissolved load after sediment uptake at each salinity point, which is estimated to be 1.00, 0.98, 0.95 and 0.98 at very low, low, medium and high salinity, respectively, according to the fractionation model (Table S5). Thus, the Σf in the Amazon estuary is calculated as 0.96–0.98 at medium and high salinity (Fig. 6, Supplementary Material S5). Specifically, around 2–3% of the Li contributed from river water and around 2–4% of the Li contributed from seawater are removed by the sediments in the Amazon estuary (Fig. 6, Supplementary Material S5). Therefore, the Li loss from river water in the Amazon estuary is calculated to be around 1.1–1.7 × 10⁸ g/yr, equivalent to 2–3% of the dissolved Li flux of the Amazon River.

From the sediment perspective, the average [Li]$_{sediment\ added}$ is estimated to be 3–4 μg/g using the fractionation model (Section 5.1.3). Combined with the Amazon sediment load of around 1.2 × 10¹² kg/yr (Milliman and Farnsworth, 2011), we estimate that the total Li removed from the dissolved load by sediment in the Amazon estuary is 3.6–4.8 × 10⁹ g/yr. Note that the removed Li flux is contributed by both river water and seawater, and that the Li removal mainly occurs from the river mouth to the middle estuary. According to the estuary model (Supplementary Material S5), the seawater-contributed Li mass is integrated as nearly 36 times that of the river water contributed Li mass from the river mouth to the middle estuary (i.e., at a salinity of 9.3) (Fig. 6). In this case, around 1.0–1.3 × 10⁸ g/yr of the Li removal by sediment is from river water, which is 1.8–2.4% of the dissolved Li discharge of the Amazon River. This estimate from the sediment perspective is in agreement with the estimate from the dissolved perspective, although the small difference may stem from the
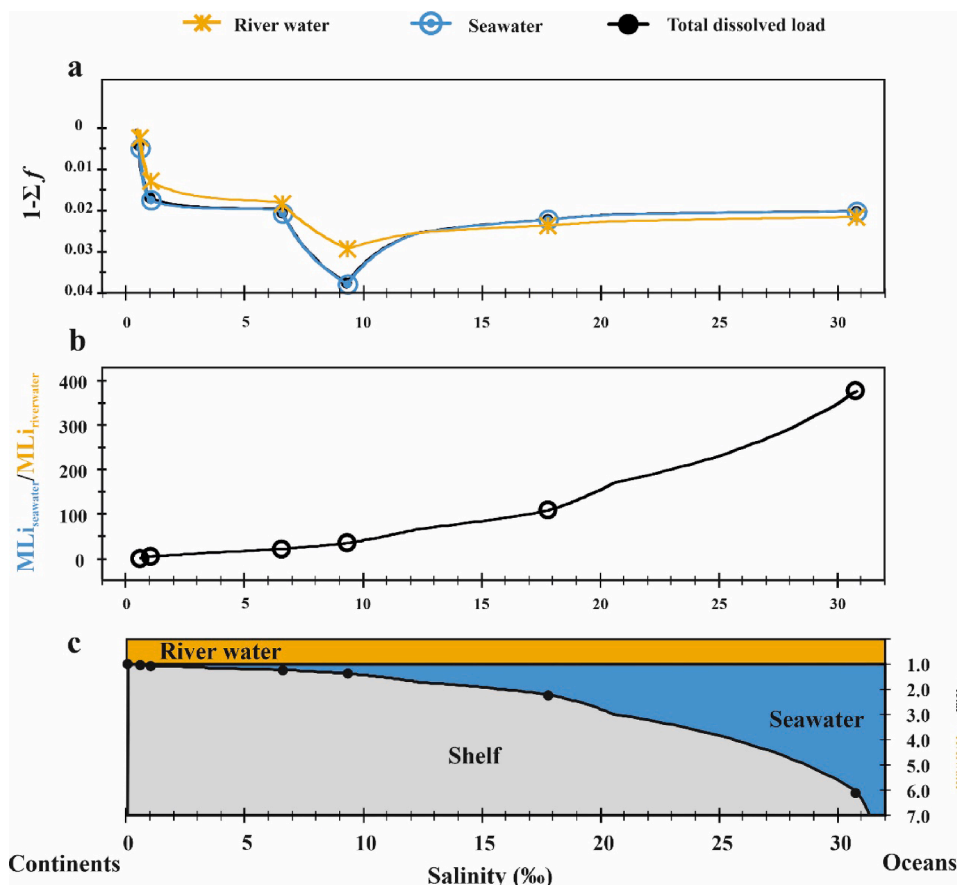
Fig. 6. Modelled Li loss from the dissolved load through the estuary. (a) The accumulated fraction of Li loss from the dissolved load after sediment removal (i.e., from the start of the Amazon estuary to the corresponding salinity point) (Section 5.1.4 and Supplementary Material S5). The black points represent Σf, which is the fraction of Li that remains in the dissolved load after Li removal by sediments accumulated to a given point in the estuary. The yellow cross symbols represent Σf_{river}, which is the fraction of Li supplied by the river water that remains in the dissolved Li supplied by the river water after Li removal by sediments accumulated to a given point in the estuary. The blue open circles represent $\Sigma f_{seawater}$, which is the fraction of Li supplied by the seawater that remains in the dissolved Li supplied by the seawater after Li removal by sediments accumulated to a given point in the estuary. (b) The ratio of dissolved load Li derived from seawater to that derived from river water through the Amazon estuary (Supplementary Material S5, Table S5). (c) The ratio of total water volume to river water volume, and a schematic diagram for river water and seawater volumes in the estuary (Supplementary Material S5, Table S5). In all panels, the lines between every set points are connected based on the data at the fitting salinities. The fitting salinities are calculated by the linear interpolation between samples whose salinity and Li concentration are obtained by measurements (Supplementary Material S5, Table S5).

uncertainty in the SSC values and spatial distributions through the estuary. In contrast to little removal of Li derived from river water, around $3.5–4.7 \times 10^9$ g/yr of Li removed from seawater by Amazon estuarine sediments is estimated.

5.2. Retention of major cations during estuarine processes

Besides Li, several major elements, such as Na, K, Mg and Ca, may transfer between the dissolved load and sediments during estuarine processes, which is likely to influence ocean biogeochemistry and the carbon cycle. It is known that continental silicate weathering net consumes atmospheric CO_2 if the dissolved cations and alkalinity produced during continental silicate weathering are transported into the ocean by rivers and deposited as carbonate (Berner and Berner, 1997). In contrast, if the dissolved cations and alkalinity are adsorbed and/or incorporated by aluminosilicate and/or hydroxides particles, there is no net atmospheric CO_2 consumption (Mackenzie and Kump, 1995; Berner and Berner, 1997). Thus, it is important to examine the fate of the cations, especially Ca and Mg, which are the major cations during carbonate formation.

5.2.1. Exchangeable pool

Some major elements in the riverine-dissolved load, such as K, Mg and Ca, can be attracted by the charged surfaces of sediments, especially clays (Sposito et al., 1999; Tipper et al., 2020). Although there is no direct alkalinity transfer during ion exchange (White, 2013), the adsorption of cations, especially Ca and Mg, can affect the cycle of Ca and Mg and the pH of seawater in theory, and hence influence the carbon cycle (Pogge von Strandmann et al., 2019a; Tipper et al., 2020). Notably, the exchangeable cations could return to the dissolved load during the subsequent diagenesis (Higgins and Schrag, 2010) because of the rapid interaction between the exchangeable pool and porewater

(Sayles and Mangelsdorf Jr., 1979; Lupker et al., 2016; Tipper et al., 2020).

The [Ca]$_{exchangeable}$ in the riverine endmember from the north channel (24MUC) and south channel (67MUC) transects are 0.8 mg/g and 2.2 mg/g, respectively, whereas the [Ca]$_{exchangeable}$ in the estuarine sediments varies from 0.7 to 1.5 mg/g. There is no clear relationship between [Ca]$_{exchangeable}$ and [Li]$_{exchangeable}$ (Fig. 7a), whereas [Ca]$_{exchangeable}$/[Li]$_{exchangeable}$ decreases with increasing $\delta^7Li_{exchangeable}$ (Fig. 7b) and increasing salinity. Furthermore, [Ca]$_{exchangeable}$/[Li]$_{exchangeable}$ is much lower in the ocean endmember than the riverine endmember. Therefore, the estuarine exchangeable pool may not be a significant sink for continent-derived Ca (Sayles and Mangelsdorf Jr., 1979). In contrast, the Amazon estuary exchangeable pool is likely a sink of continent-derived Mg (Sayles and Mangelsdorf Jr., 1979). The [Mg]$_{exchangeable}$ in the estuarine sediments varies from 1.2 to 1.9 mg/g, which is higher than [Mg]$_{exchangeable}$ in the riverine endmember from the north channel (0.5 mg/g) and south channel (0.3 mg/g).

Interestingly, the [K]$_{exchangeable}$/[Ca]$_{exchangeable}$ and [K]$_{exchangeable}$/[Mg]$_{exchangeable}$ ratios in the Amazon estuarine sediments are higher than in Amazon River sediments (Sayles and Mangelsdorf Jr., 1979). This finding implies that the dominant cations in the exchangeable pool shift from Ca in the river sediments to K, as well as Na (Sayles and Mangelsdorf Jr., 1979), in the estuarine sediments, which is also observed globally (Lupker et al., 2016; Tipper et al., 2020).

5.2.2. Retention of cations in clays

The element concentrations in the clay phase indicate the retention of cations by aluminosilicate particles. [Mg]$_{clay}$ and [K]$_{clay}$ increase through the estuary and have a positive relationship with both [Li]$_{clay}$ and δ^7Li_{clay} (Fig. 8). In contrast, [Al]$_{clay}$ and [Fe]$_{clay}$ increase at low salinity but remain stable after medium salinity, therefore [Al]$_{clay}$/[Li]$_{clay}$ and [Fe]$_{clay}$/[Li]$_{clay}$ decrease through the estuary and display a
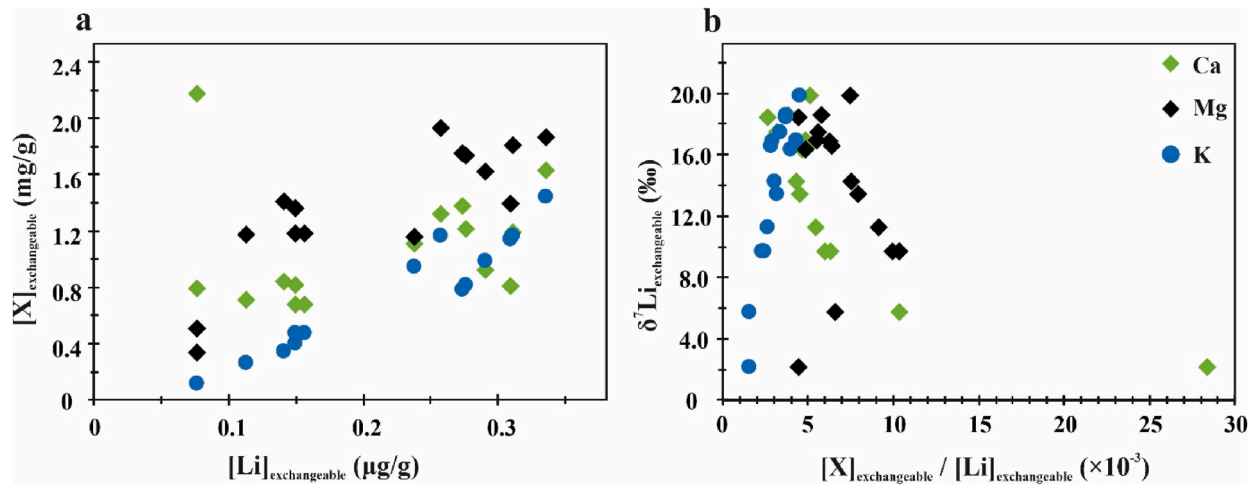
Fig. 7. The adsorption of cations by the exchangeable pool. (a) Trends of major element concentrations (Ca, Mg and K) with Li concentrations in the exchangeable pool of the sediment samples (i.e., SPM and MUC). (b) Trends of major element concentrations (Ca, Mg and K, as ratios to Li) with Li isotope compositions in the exchangeable pool of the sediment samples (i.e., SPM and MUC). The element ratios are by mass.
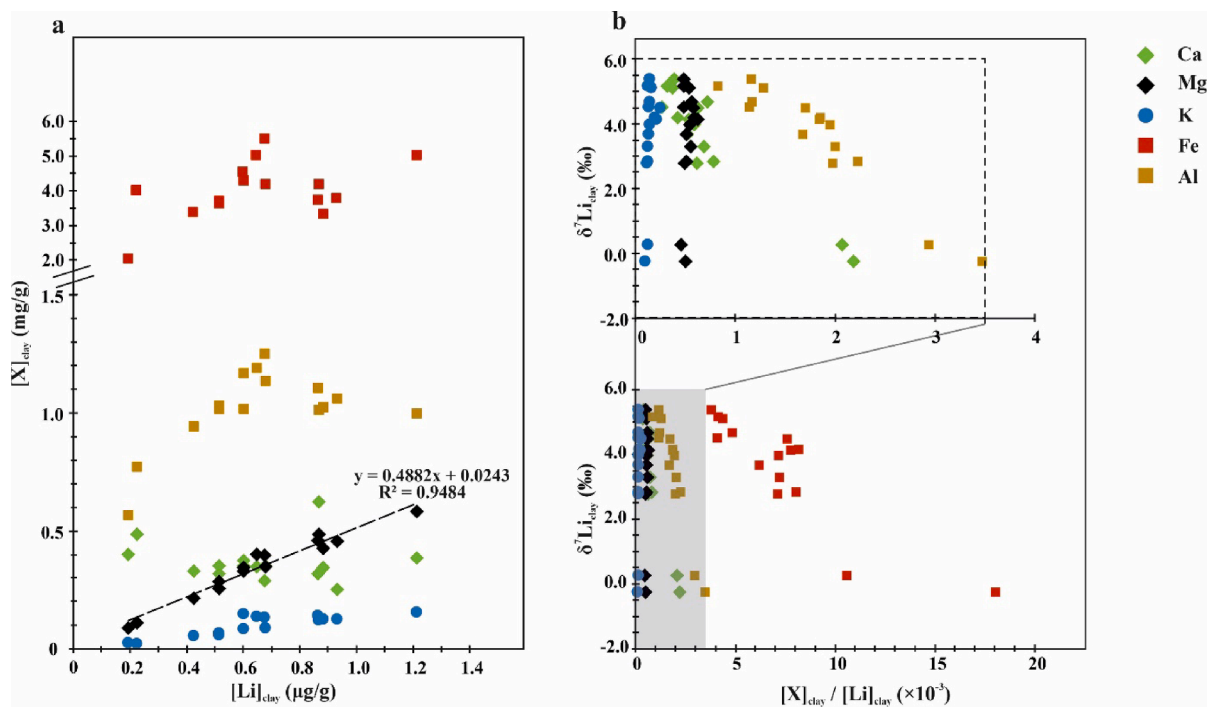

Fig. 8. The retention of cations in the clay phases. (a) Trends of major element concentrations (Ca, Mg, K, Fe and Al) with Li concentrations in the leached clay phase of the sediment samples (i.e., SPM and MUC, except for 41MUC). The black dashed line is a best-fit line for $[Mg]_{clay}$ versus $[Li]_{clay}$. (b) Trends of major element concentrations (Ca, Mg, K, Fe and Al, as ratios to Li) with Li isotope compositions in the leached clay phase of the sediment samples (i.e., SPM and MUC, except for 41MUC). The shaded area is magnified in the inset graph surrounded by the dashed box. The element ratios are by mass.

negative relationship with δ^7Li_{clay} (Fig. 8b). This indicates that the concentrations of mobile cations (e.g., Mg, K and Li) in clay phases increase through the estuary, which may be driven by the changes in water composition from river to estuary. The concentrations of dissolved Mg, K and Li in the saline water are much higher than river water, whereas the dissolved Al and Fe concentrations decrease to very low levels in the low salinity zone due to flocculation in the estuary (Boyle et al., 1977; Sholkovitz, 1978). The increasing concentration of mobile cations in the clay phase is also supported by mineral stability diagrams, which show a shift from the kaolinite (1:1 structure clay) field in the river water to the Na/K-micas or Na/K-smectite (2:1 structure clays) fields in the estuary (Fig. S3) (Velde, 1995). Although in the estuary transect the mechanical

sorting of river-derived sediments and differential flocculation of different clays also could lead to a shift from kaolinite to montmorillonite (Gibbs, 1967, 1977), the increased δ^7Li_{clay} nevertheless indicates the chemical retention of cations.

Interestingly, $[Mg]_{clay}/[Li]_{clay}$ and $[K]_{clay}/[Li]_{clay}$ generally remain constant at 500 and 150, respectively, through the estuary (Fig. 8b). In the dissolved load, starting from the salinity of 0.58, the concentration ratio of Mg and Li and the ratio of K and Li are stable at around 7300 and 2000, respectively. Thus, this may indicate an uptake of K, Mg and Li by the clays in equal proportions, possibly because major cations (but also Li) are present in high concentrations in the brackish water, due to inflow from seawater. In this case, clays (as well as oxides,

Supplementary Material S3) incorporate approximately 2 μg of Li for every 1 mg of Mg incorporated (Figs. 8a and S4). According to the calculations for sediment removal from the Li isotope fractionation model, the [Li]$_{sediment\ added}$ is around 3–4 μg/g and the total Li removal is 3.6–4.8 × 10^9 g/yr (Section 5.1.3 and 5.1.4). Therefore, the Mg incorporated in clays in the Amazon estuary is calculated to be 1.8–2.4 × 10^{12} g/yr. Furthermore, calculations using PHREEQC (Parkhurst and Appelo, 2013) show that Mg clays, such as sepiolite, are highly supersaturated, with their saturation index (SI) increasing from around 10 to 17 at low to medium salinity and then decreasing to around 14 at high salinity (Fig. S5, Table S6). Thus, the Mg incorporated in clays during estuarine processes likely has a significant influence on the Mg cycle in the ocean (Tipper et al., 2006; Berg et al., 2019; Shalev et al., 2019), although the Mg incorporated in clays during estuarine processes could subsequently be altered during diagenesis after burial (Higgins and Schrag, 2010). In contrast, [Ca]$_{clay}$ remains relatively stable throughout the estuary (excluding the high-carbonate sample 41MUC) and [Ca]$_{clay}$/[Li]$_{clay}$ decreases with increasing δ^{7}Li$_{clay}$ (Fig. 8). In addition, the calculated SI of calcite and dolomite change from undersaturated at low salinity to

supersaturated at medium salinity, which implies the potential for carbonate formation (Fig. S5, Table S6). Therefore, in the Amazon estuary, river-derived dissolved Ca is more likely to participate in carbonate formation than retention by clays.

5.3. Mechanical sorting and chemical alteration of bulk sediments

The concentrations of Ca, Mg, K, Fe, Mn, Al and Li in the bulk sediments are calculated from Eq. (2), but Na and Si concentration data are not available due to the leaching and dissolution methods. Based on the elemental composition of Amazon River sediment collected further inland, Na$_2$O comprises less than 2.0% of the bulk sediments (Martinelli et al., 1993; Dellinger et al., 2014), which is much less than its Al and Fe content. The Si concentrations can be approximately calculated using Eqs. (12) and (13), assuming the major elements are Al, Fe, K, Mg, Ca and Mn.

$$SiO_2\ (g/g) = 1\ (g/g) - (Al_2O_3\ (g/g) + Fe_2O_3\ (g/g) + K_2O\ (g/g)$$
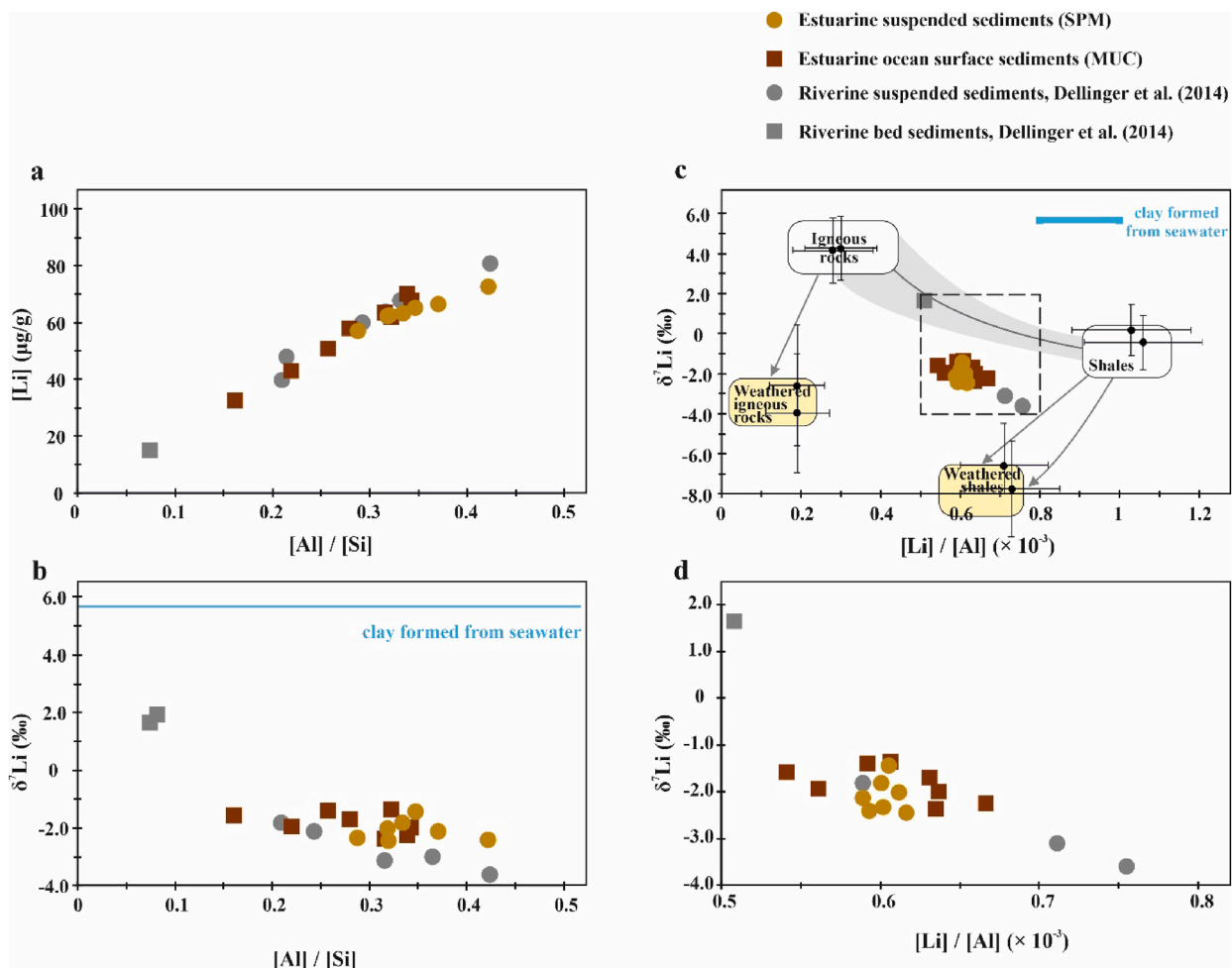$$+ MgO\ (g/g) + CaO\ (g/g) + MnO\ (g/g)) \quad (12)$$

Fig. 9. Relationships between Al, Si and Li concentrations, and Li isotopes, of bulk sediment samples from the Amazon. (a) Relationship between Al/Si ratios and Li concentrations in bulk sediment samples, including data from this study and from Dellinger et al. (2014). (b) Relationship between Al/Si ratios and Li isotope compositions in bulk sediment samples, including data from this study and from Dellinger et al. (2014). The blue line represents the estimated endmember of clays formed in seawater (δ^{7}Li = 5.7‰; Fig. 4). (c) Relationship between Li/Al ratios and Li isotope compositions in bulk sediment samples, including data from this study and from Dellinger et al. (2014). The blue line represents the estimated endmember of clays formed in seawater (δ^{7}Li = 5.7‰, Li/Al = 0.8–1.0). The rectangles with round corners are the continental weathering endmembers from Dellinger et al. (2014), and the black dots with error bars are the posteriori endmembers for the Amazon River derived in the inverse mixing modelling of Dellinger et al. (2014). The grey line and shaded area represent the mixtures between the igneous rock and shale endmembers, and the grey arrows represent the Li fractionation trend during weathering as shown in Dellinger et al. (2014). The data in the dashed box are shown magnified in panel (d). In all cases, the element ratios are by mass. In addition, the Al, Si and Li concentrations and Li isotope composition in bulk sediment samples from the c by Eqs. (1)–(3), (12) and (13). Note that data from sample 41MUC are not included.

$$[Si]_{bulk} \; (mg/g) = 1000 \times SiO_2 \; (g/g) \times molar \; mass \; Si \; (g/mol) \\ / \; molecular \; mass \; SiO_2 \; (g/mol) \quad (13)$$

The calculated $[Si]_{bulk}$ for the estuarine sediments range from 269 to 375 mg/g, which are within the range of measured Amazon River sediments further inland (Dellinger et al., 2014). The $[Al]_{bulk}/[Si]_{bulk}$ of the SPM samples are generally higher than for the MUC samples (Fig. 9a). The $[Al]_{bulk}/[Si]_{bulk}$ ratio increases at low and medium salinity but decreases at high salinity. At high salinity (sample 41MUC), both $[Al]_{bulk}$ and $[Si]_{bulk}$ decrease probably due to dilution of the silicate portion (likely of varying silicate mineral types) of the sediments by carbonates (Table 2, Supplementary Material S2). In the low and medium salinity zones, the increase in $[Al]_{bulk}/[Si]_{bulk}$ indicates an increase in clay content, as Al content of clays is generally higher than primary silicate minerals such as olivine, feldspar and quartz (Velde, 1995). The increasing surface area of MUC samples also shows an increasing clay content through the estuary (Fig. S6).

The increase in clay content could stem from two processes: clay neoformation in the estuary (Michalopoulos and Aller, 1995; Michalopoulos et al., 2000; Pogge von Strandmann et al., 2008) and/or mechanical sorting (Gibbs, 1977), as clays have a finer particle size than (eroded) primary grains and slow settling rates. However, the δ^7Li_{bulk} values lie in a narrow range from -2.4 to -1.3‰ through the estuary without a clear relationship to $[Al]_{bulk}/[Si]_{bulk}$ or $[Li]_{bulk}/[Al]_{bulk}$ (Fig. 9b and d). This indicates that the increased clay content in bulk sediment is mainly caused by mechanical sorting rather than clay neoformation in the Amazon estuary, similar to the observation from the Gulf of Papua (Brunskill et al., 2003) and the Yangtze River (Yang et al., 2021). Using Scanning Electron Microscope (SEM), the sample 85MUC at around 200 km away from Amazon River mouth is observed to contain finer particles than the sample 24MUC from the river end-member in the Amazon estuary (Fig. S7).

In contrast, during continental weathering in the Amazon catchment, as well as global large river catchments, the δ^7Li values of bulk sediments appear to decrease with increasing $[Al]/[Si]$ and $[Li]/[Al]$ (Fig. 9c) (Dellinger et al., 2014; Yang et al., 2021). This reflects that clay neoformation during continental weathering significantly contributes to the increasing clay content in river sediments. Thus, the amount of clays formed in the Amazon basin and the amount of eroded grains in the hinterland is much larger than the amount of clay formed in the estuary. The clays and eroded grains from the Amazon basin dominate the bulk estuarine sediments and mask the changes in bulk Li isotope composition. Although the δ^7Li_{bulk} values in estuarine sediments do not appear to reflect the alteration during estuarine processes, the chemically extracted clay phases nevertheless do provide evidence of alteration of river-derived particles during estuarine processes (Section 5.2.2), which indicates the value in examining the different phases contained within bulk sediment samples.

5.4. Implications of alteration of river-derived particles during estuarine processes for the global ocean Li budget

So far, only relatively few estuaries have been explored for their Li concentration and Li isotope behaviour, which is not yet sufficient to give a global view. In the Amazon estuary, as discussed previously, around 1.8–3.0% of the river input dissolved Li is retained in the river-derived sediments before they are buried (Section 5.1.4). In the Borgarfjörður estuary in Iceland, approximately 1.2% of the river dissolved Li input flux is estimated to be removed by its river-derived sediments, if the partition of Li removal from river water and seawater is similar to that of the Amazon estuary (Pogge von Strandmann et al., 2008). A limited modification by estuarine processes has also been observed in the Yangtze River estuary (Yang et al., 2021). Considering the similar minor modifications on riverine Li input among the estuaries of the preceding rivers, especially the Amazon and the Yangtze as large rivers,

the modification of the global riverine-dissolved Li input flux by river-derived sediments in estuaries could be expected to be less than 5.0% of its total. However, this minor impact on riverine Li fluxes must be examined in other estuaries, especially for large rivers with very high SSC, such as the Yellow River (average 26.9 g/L), Indus (2.8 g/L) and Ganges-Brahmaputra (1.1 g/L) (Huh et al., 1998; Gaillardet et al., 1999; Milliman and Farnsworth, 2011).

In contrast to the relatively minor impact on the riverine Li input flux, the amount of Li removed from seawater by river-derived sediments in the Amazon estuary is significant ($3.5–4.7 \times 10^9$ g/yr). Aside from the Amazon, the Li removal by estuarine sediments has been explored for only a few rivers. Pogge von Strandmann et al. (2008) examined Li and its isotopes in the dissolved load and bulk suspended sediments in the small basaltic estuary of Borgarfjörður, Iceland. In that estuary, about 3 µg/g Li was added to the suspended sediments, similar to our observations from the Amazon estuary. Around $0.84–1.4 \times 10^{10}$ g/yr of Li removal in global basaltic estuaries was estimated when considering the particle residence time in the estuary (Pogge von Strandmann et al., 2008). Brunskill et al. (2003) examined Li concentrations in both the dissolved load and bulk sediments in the Gulf of Papua, which is mainly supplied by the Fly, Purari and Kikori rivers. Both the water and particle discharge of the three rivers combined would rank at around 11th to 15th amongst global rivers (Milliman and Syvitski, 1992; Milliman and Farnsworth, 2011). Their average SSC (0.43 g/L, sediment discharge/water discharge, Brunskill et al., 2003) is around 0.24 g/L higher than that in the Amazon, and the Li uptake by sediments is estimated at around 6.87×10^9 g/yr (Brunskill et al., 2003). However, this estimate also includes the Li uptake after burial. Yang et al. (2021) explored Li and its isotopes in the estuary of the Yangtze River, ranked globally as 4th for discharge (Huh et al., 1998) and 5th for sediment load (Milliman and Farnsworth, 2011). Their study suggested that Li uptake by sediments is negligible give the conservative mixing of dissolved Li observed, and the Li isotope compositions in bulk sediments are consistent (Yang et al., 2021). However, the Li concentrations and Li isotopes in the exchangeable pool of those sediments show an increase through the Yangtze River estuary towards the ocean (Yang et al., 2021). The δ^7Li values exhibit a negative linear relationship with $1/Li$ ($R^2 = 0.73$) in the exchangeable pool, with an empirical endmember δ^7Li value of 23.4‰ suggesting that $\alpha_{exchangeable-seawater}$ is around 0.9924 in the Yangtze River estuary, which is similar to our observations of exchange in the Amazon River estuary (Section 5.1.2). Hence, around 0.2 µg/g of Li added to the exchangeable pool could be estimated based on their data (Yang et al., 2021), which is nevertheless smaller than the total Li removal in the Amazon estuary. In contrast, Colten and Hanor (1984) report Li concentration decreases in the exchangeable pool with increasing salinity through the Mississippi River estuary, which ranks as 6th for both discharge and sediment load amongst global rivers. In this study, however, the Li removal by global estuarine sediments is estimated to be $3.6–5.4 \times 10^{10}$ g/yr ($5.2–7.8 \times 10^9$ mol/yr) by assuming around 2–3 µg/g Li retained in river-derived sediments in the estuaries before burial. However, again, it is difficult to give an accurate global estimate due to the lack of sufficient data on the Li behaviour in different phases of the sediment and in different global settings. Thus, more large rivers need to be examined, especially those with a high particle load, such as the Brahmaputra-Ganges and Yellow rivers (Huh et al., 1998; Gaillardet et al., 1999; Milliman and Farnsworth, 2011).

In the ocean, there are two major Li inputs (i.e., river input and hydrothermal input) and two major outputs (i.e., AOC and uptake by MAAC) (Chan et al., 1992; Huh et al., 1998; Hathorne and James, 2006; Misra and Froelich, 2012; Li and West, 2014). If as large as extrapolated, the Li sink by river-derived sediment in the estuary before burial (i.e., estuarine cation removal, ECR), with a magnitude of approximately $3.6–5.4 \times 10^{10}$ g/yr and a fractionation ($\Delta^7Li_{ECR-seawater}$) of -20 to -30‰, could make another comparatively important contribution to the AOC and MAAC (Table S1). Notably, during ECR, Li is mainly removed by secondary minerals of the river-derived particles in the

saline water (Section 5.1.2), so theoretically, the interactive environments and Li-bonding sites during ECR are similar to MAAC. In this case, the fractionation during ECR and MAAC is similar, but larger than AOC, whose alteration temperature is higher (Hoefs and Sywall, 1997; Huh et al., 1998; Zhang et al., 1998; Li and West, 2014; Kalderon-Asael et al., 2021) (Table S1). Furthermore, as discussed in Sections 5.1.3 and 5.1.4, the ECR is related to riverine sediment discharge and is therefore closely related to continental erosion rates. Thus, the continental weathering (both physical erosion and chemical weathering) regime influences not only the dissolved riverine Li input flux and isotope composition (Dellinger et al., 2015; Pogge von Strandmann et al., 2021) but also the ECR output flux directly. Thus, ECR flux may change sensitively with continental erosion and exert an influence on the Li ocean output fluxes and therefore the Li isotope composition of the ocean (Li and West, 2014). For example, given that the continental erosion rate is thought to have increased during the Cenozoic due to mountain uplift and glacial expansion (Hay et al., 1989; Métivier et al., 1999), the ECR was likely much lower during the early Cenozoic than in the modern ocean, which could have helped contribute to the lower seawater δ^7Li values at that time (Li and West, 2014).

6. Conclusion

Lithium concentrations and isotopes from the dissolved load and different leached phases of the suspended sediment and bedload were measured at a series of sites from the Amazon estuary. The dissolved Li concentrations generally showed conservative mixing between river water and seawater in the Amazon offshore transect. In contrast, the dissolved δ^7Li values were slightly higher than the predicted values based on conservative mixing at medium salinity, indicating sensitivity of Li isotopes to non-conservative processes, and specifically to Li removal by sediments. Although there was some contribution from adsorption into the exchangeable pool, the Li was mainly retained into the secondary mineral lattice, especially the clays. In the Amazon estuary, the fraction of Li neo-incorporated into secondary mineral phases was estimated to be 3–4 μg/g in the river-derived sediments, with an isotopic fractionation factor $\alpha_{clay-seawater}$ of approximately 0.975. Through the whole Amazon estuary, the river-derived sediments removed around 3.6–4.8×10^9 g/yr of Li from the dissolved load. Specifically, around 1.0–1.7×10^8 g/yr was removed from river water, representing around 1.8–3.0% of the dissolved Li flux discharged by the Amazon River, whereas around 3.5–4.7×10^9 g/yr of Li was removed from seawater by river-derived sediments in the Amazon estuary.

For the ocean Li budget, although the estuarine modification of the dissolved load riverine Li input flux was insignificant, the extrapolated global dissolved Li removal by river-derived sediments was estimated to be around 3.6–5.4×10^{10} g/yr, which is comparable in magnitude to the previously estimated global marine authigenic clay Li sinks. However, few estuaries have been studied in detail for Li isotopes, so such estimates need to be verified by data collection from different estuarine settings. We also noted that the estuarine Li sink is likely to be closely related to the sediment input from continental erosion, and therefore changes in continental weathering and erosion regimes not only could influence the Li input flux and Li isotope composition of rivers but also could directly affect the estuarine Li sink, leading to a dual control on the Li isotope composition of the oceans.

In addition, elements such as Mg and K showed similar removal patterns to Li with retention by both exchangeable pool and clay phases in estuarine sediments. The different solution compositions of river water and seawater could be responsible for a shift in mineral stability in estuaries, thereby promoting the retention of Mg, K and Li in river-derived sediments. Particularly, the retention of Mg in clays may be a significant sink in the ocean Mg budget and would reduce the CO_2 burial efficiency arising from continental chemical weathering.

Declaration of Competing Interest

The authors declare that they have no known competing financial interests or personal relationships that could have appeared to influence the work reported in this paper.

Appendix A. Supplementary material

Supplementary material to this article can be found online at https://doi.org/10.1016/j.gca.2023.08.015. In Supplementary Material 1, first, the accuracy of elemental recovery in the full sequential leaching procedure is verified based on a comparison to the elemental concentrations measured in bulk sample dissolutions (Supplementary S1). Second, Supplementary S2 and S3 describe the results of major element concentrations (e.g., Ca, Mg, K, Al, Fe and Mn) in leaching phases (i.e., exchangeable, carbonate, oxide, clay and residue). Third, the details of the Li isotope fractionation model are described in Supplementary S4 and the estuary model for estimating Li removal flux is described in Supplementary S5. Fourth, the mineral stability and saturation are estimated based on the element concentrations in Amazon estuarine water samples. Finally, the list of symbols in the modelling is shown in Supplementary S7. In addition, the related figures to the supplementary text are attached in Supplementary Material 1. In Supplementary Material 2, a summary of published Li sink estimates is shown in Supplementary Table 1. The sampling details of solid samples are shown in Supplementary Table 2. The measured element concentrations (e.g., Na, Mg, Ca, K, Fe, Al, Mn, Li, Sr and Rb) of reference materials (i.e., NBS SRM 88A and SGR-1) are given in Supplementary Table 3. The calculations of Li isotope fractionation and estuary model are shown in Supplementary Tables 4 and 5. The mineral saturation calculated using PHREEQC is shown in Supplementary Table 6.

References

Andrews, E., Pogge von Strandmann, P.A.E., Fantle, M.S., 2020. Exploring the importance of authigenic clay formation in the global Li cycle. Geochim. Cosmochim. Acta 289, 47–68.

Benner, R., Opsahl, S., 2001. Molecular indicators of the sources and transformations of dissolved organic matter in the Mississippi river plume. Org. Geochem. 32, 597–611.

Berg, R.D., Solomon, E.A., Teng, F.Z., 2019. The role of marine sediment diagenesis in the modern oceanic magnesium cycle. Nat. Commun. 10, 4371.

Berner, E.K., Berner, R.A., 1996. Global Environment: Water, Air, and Geochemical Cycles. Prentice Hall, USA.

Berner, R.A., Berner, E.K., 1997. Silicate weathering and climate. In: Ruddiman, W.F. (Ed.), Tectonic Uplift and Climate Change. Springer, Boston.

Bouchez, J., Gaillardet, J., von Blanckenburg, F., 2014. Weathering intensity in lowland river basins: from the Andes to the Amazon Mouth. Procedia Earth Planet. Sci. 10, 280–286.

Boyle, E.A., Collier, R., Dengler, A.T., Edmond, J.M., Ng, A.C., Stallard, R.F., 1974. On the chemical mass-balance in estuaries. Geochim. Cosmochim. Acta 38, 1719–1728.

Boyle, E.A., Edmond, J.M., Sholkovitz, E.R., 1977. The mechanism of iron removal in estuaries. Geochim. Cosmochim. Acta 41, 1313–1324.

Brunskill, G.J., Zagorskis, I., Pfitzner, J., 2003. Geochemical mass balance for lithium, boron, and strontium in the Gulf of Papua, Papua New Guinea (Project TROPICS). Geochim. Cosmochim. Acta 67, 3365–3383.

Callahan, J., Dai, M., Chen, R.F., Li, X., Lu, Z., Huang, W., 2004. Distribution of dissolved organic matter in the Pearl River Estuary, China. Mar. Chem. 89, 211–224.

Chan, L.H., Alt, J.C., Teagle, D.A.H., 2002. Lithium and lithium isotope profiles through the upper oceanic crust: A study of seawater-basalt exchange at ODP Sites 504B and 896A. Earth Planet. Sci. Lett. 201, 187–201.

Chan, L.H., Hein, J.R., 2007. Lithium contents and isotopic compositions of ferromanganese deposits from the global ocean. Deep Res. Part II Top. Stud. Oceanogr. 54, 1147–1162.

Chan, L.H., Edmond, J.M., Thompson, G., Gillis, K., 1992. Lithium isotopic composition of submarine basalts: implications for the lithium cycle in the oceans. Earth Planet. Sci. Lett. 108, 151–160.

Charbonnier, Q., Bouchez, J., Gaillardet, J., Gayer, É., 2020. Barium stable isotopes as a fingerprint of biological cycling in the Amazon River basin. Biogeosciences 17, 5989–6015.

Chester, R., 1990. Marine Geochemistry. Unwin Hyman Ltd, London.

Clergue, C., Dellinger, M., Buss, H.L., Gaillardet, J., Benedetti, M.F., Dessert, C., 2015. Influence of atmospheric deposits and secondary minerals on Li isotopes budget in a highly weathered catchment, Guadeloupe (Lesser Antilles). Chem. Geol. 414, 28–41.

Colten, V.A., Hanor, J.S., 1984. Variations in dissolved lithium in the Mississippi River and Mississippi River estuary, Louisiana, U.S.A., during low river stage. Chem. Geol. 47, 85–96.

Condie, S.A., 1991. Separation and recirculation of the North Brazil Current. J. Mar. Res. 49, 1–19.

Dellinger, M., Gaillardet, J., Bouchez, J., Calmels, D., Galy, V., Hilton, R.G., Louvat, P., France-Lanord, C., 2014. Lithium isotopes in large rivers reveal the cannibalistic nature of modern continental weathering and erosion. Earth Planet. Sci. Lett. 401, 359–372.

Dellinger, M., Gaillardet, J., Bouchez, J., Calmels, D., Louvat, P., Dosseto, A., Gorge, C., Alanoca, L., Maurice, L., 2015. Riverine Li isotope fractionation in the Amazon River basin controlled by the weathering regimes. Geochim. Cosmochim. Acta 164, 71–93.

DeMaster, D.J., Knapp, G.B., Nittrouer, C.A., 1983. Biological uptake and accumulation of silica on the Amazon continental shelf. Geochim. Cosmochim. Acta 47, 1713–1723.

Dosseto, A., Bourdon, B., Gaillardet, J., Allègre, C.J., Filizola, N., 2006. Time scale and conditions of weathering under tropical climate: Study of the Amazon basin with U-series. Geochim. Cosmochim. Acta 70, 71–89.

Elderfield, H., Schultz, A., 1996. Mid-ocean ridge hydrothermal fluxes and the chemical composition of the ocean. Annu. Rev. Earth Planet. Sci. 24, 191–224.

Gaillardet, J., Dupré, B., Allègre, C.J., Négrel, P., 1997. Chemical and physical denudation in the Amazon River Basin. Chem. Geol. 142, 141–173.

Gaillardet, J., Dupré, B., Louvat, P., Allègre, C.J., 1999. Global silicate weathering and CO_2 consumption rates deduced from the chemistry of large rivers. Chem. Geol. 159, 3–30.

Geyer, W.R., Beardsley, R.C., Lentz, S.J., Candela, J., Limeburner, R., Johns, W.E., Castro, B.M., Soares, I.D., 1996. Physical oceanography of the Amazon shelf. Cont. Shelf Res. 16, 575–616.

Gibbs, R.J., 1967. The Geochemistry of the Amazon River System: Part I. The factors that control the salinity and the composition and concentration of the suspended solids. GSA Bull. 78, 1203–1232.

Gibbs, R.J., 1976. Amazon River sediment transport in the Atlantic Ocean. Geology 4, 45–48.

Gibbs, R.J., 1977. Clay mineral segregation in the marine environment. J. Sediment. Res. 47, 237–243.

Gislason, S.R., Oelkers, E.H., Eiriksdottir, E.S., Kardjilov, M.I., Gisladottir, G., Sigfusson, B., Snorrason, A., Elefsen, S., Hardardottir, J., Torssander, P., Oskarsson, N., 2009. Direct evidence of the feedback between climate and weathering. Earth Planet. Sci. Lett. 277, 213–222.

Gou, L.F., Liu, C.Y., Deng, L., Jin, Z., 2020. Quantifying the impact of recovery during chromatographic purification on the accuracy of lithium isotopic determination by multi-collector inductively coupled plasma mass spectrometry. Rapid Commun. Mass Spectrom. 34, e8577.

Hathorne, E.C., James, R.H., 2006. Temporal record of lithium in seawater: A tracer for silicate weathering? Earth Planet. Sci. Lett. 246, 393–406.

Hay, W.W., Shaw, C.A., Wold, C.N., 1989. Mass-balanced paleogeographic reconstructions. Geol. Rundschau 78, 207–242.

Higgins, J.A., Schrag, D.P., 2010. Constraining magnesium cycling in marine sediments using magnesium isotopes. Geochim. Cosmochim. Acta 74, 5039–5053.

Hindshaw, R.S., Aciego, S.M., Tipper, E.T., 2018. Li and U isotopes as a potential tool for monitoring active layer deepening in permafrost dominated catchments. Front. Earth Sci. 6, 102.

Hindshaw, R.S., Tosca, R., Goût, T.L., Farnan, I., Tosca, N.J., Tipper, E.T., 2019. Experimental constraints on Li isotope fractionation during clay formation. Geochim. Cosmochim. Acta 250, 219–237.

Hoefs, J., Sywall, M., 1997. Lithium isotope composition of Quaternary and Tertiary biogene carbonates and a global lithium isotope balance. Geochim. Cosmochim. Acta 61, 2679–2690.

Huh, Y., Chan, L.H., Zhang, L., Edmond, J.M., 1998. Lithium and its isotopes in major world rivers: implications for weathering and the oceanic budget. Geochim. Cosmochim. Acta 62, 2039–2051.

Hydes, D.J., Liss, P.S., 1977. The behaviour of dissolved aluminium in estuarine and coastal waters. Estuar. Coast. Mar. Sci. 5, 755–769.

Jeffcoate, A.B., Elliott, T., Thomas, A., Bouman, C., 2004. Precise, small sample size determinations of lithium isotopic compositions of geological reference materials and modern seawater by MC-ICP-MS. Geostand. Geoanal. Res. 28, 161–172.

Jiang, S., Müller, M., Jin, J., Wu, Y., Zhu, K., Zhang, G., Mujahid, A., Rixen, T., Muhamad, F.M., Sia, E.S.A., Jang, F.H.A., Zhang, J., 2019. Dissolved inorganic nitrogen in a tropical estuary in Malaysia: transport and transformation. Biogeosciences 16, 2821–2836.

Kalderon-Asael, B., Katchinoff, J.A.R., Planavsky, N.J., Hood, A.V.S., Dellinger, M., Bellefroid, E.J., Jones, D.S., Hofmann, A., Ossa, F.O., Macdonald, F.A., Wang, C., Isson, T.T., Murphy, J.G., Higgins, J.A., West, A.J., Wallace, M.W., Asael, D., Pogge von Strandmann, P.A.E., 2021. A lithium-isotope perspective on the evolution of carbon and silicon cycles. Nature 595, 394–398.

Kim, J., Grey, C.P., 2010. ^{2}H and ^{7}Li solid-state MAS NMR study of local environments and lithium adsorption on the iron(III) oxyhydroxide, akaganeite (β-FeOOH). Chem. Mater. 22, 5453–5462.

Kineke, G.C., Sternberg, R.W., Trowbridge, J.H., Geyer, W.R., 1996. Fluid-mud processes on the Amazon continental shelf. Cont. Shelf Res. 16, 667–696.

Kisakürek, B., James, R.H., Harris, N.B.W., 2005. Li and δ^7Li in Himalayan rivers: Proxies for silicate weathering? Earth Planet. Sci. Lett. 237, 387–401.

Koschinsky, A., Frank, M., Dittmar, T., Gledhill, M., de Rezende, C., Lodeiro, P., Seidel, M., Knoke, M., Paul, S., Zitoun, R., Heinrich, L., Fronzek, J., Münch, J., Scholten, J., Border, E., Schneider, A., de Carvalho, L., Leist, L., Mutzberg, A., Marques da Silva Jr., J., Cherene Bras de Oliveira, B., Walter, J., Soares Nóbrega, M., Bretschneider, L., Hathorne, E., Vosteen, P., Spiegel, T., Maguire, C., Rohleder, C., 2018. Interactions of trace metals, DOM, and particles in the Amazon estuary and associated plume as key processes for trace metal and DOM fluxes into the Atlantic. A contribution to the internatinal GEOTRACES program Cruise No. M147.

Krissansen-Totton, J., Catling, D.C., 2020. A coupled carbon-silicon cycle model over Earth history: Reverse weathering as a possible explanation of a warm mid-Proterozoic climate. Earth Planet. Sci. Lett. 537, 116181.

Kuehl, S.A., Nittrouer, C.A., DeMaster, D.J., 1982. Modern sediment accumulation and strata formation on the Amazon continental shelf. Mar. Geol. 49, 279–300.

Kuehl, S.A., DeMaster, D.J., Nittrouer, C.A., 1986. Nature of sediment accumulation on the Amazon continental shelf. Cont. Shelf Res. 6, 209–225.

Li, W., Liu, X.M., 2020. Experimental investigation of lithium isotope fractionation during kaolinite adsorption: Implications for chemical weathering. Geochim. Cosmochim. Acta 284, 156–172.

Li, W., Liu, X.M., Chadwick, O.A., 2020. Lithium isotope behavior in Hawaiian regoliths: Soil-atmosphere-biosphere exchanges. Geochim. Cosmochim. Acta 285, 175–192.

Li, G., West, A.J., 2014. Evolution of Cenozoic seawater lithium isotopes: Coupling of global denudation regime and shifting seawater sinks. Earth Planet. Sci. Lett. 401, 284–293.

Liu, C.Y., Pogge von Strandmann, P.A.E., Tarbuck, G., Wilson, D.J., 2022. Experimental investigation of oxide leaching methods for Li isotopes. Geostand. Geoanal. Res. 46, 493–518.

Lupker, M., France-Lanord, C., Lartiges, B., 2016. Impact of sediment-seawater cation exchange on Himalayan chemical weathering fluxes. Earth Surf. Dyn. 4, 675–684.

Mackenzie, F.T., Garrels, R.M., 1966. Chemical mass balance between rivers and oceans. Am. J. Sci. 264, 507–525.

Mackenzie, F.T., Kump, L.R., 1995. Reverse weathering, clay mineral formation, and oceanic element cycles. Science 270, 586–587.

Martinelli, L.A., Victoria, R.L., Dematte, J.L.I., Richey, J.E., Devol, A.H., 1993. Chemical and mineralogical composition of Amazon River floodplain sediments, Brazil. Appl. Geochem. 8, 391–402.

Métivier, F., Gaudemer, Y., Tapponnier, P., Klein, M., 1999. Mass accumulation rates in Asia during the Cenozoic. Geophys. J. Int. 137, 280–318.

Michalopoulos, P., Aller, R.C., 1995. Rapid clay mineral formation in Amazon delta sediments: Reverse weathering and oceanic elemental cycles. Science 270, 614–617.

Michalopoulos, P., Aller, R.C., Reeder, R.J., 2000. Conversion of diatoms to clays during early diagenesis in tropical, continental shelf muds. Geology 28, 1095–1098.

Milliman, J.D., Farnsworth, K.L., 2011. River Discharge to the Coastal Ocean: A Global Synthesis. Cambridge University Press, New York.

Milliman, J.D., Syvitski, J.P.M., 1992. Geomorphic/Tectonic control of sediment discharge to the ocean: The importance of small mountainous rivers. J. Geol. 100, 525–544.

Misra, S., Froelich, P.N., 2012. Lithium isotope history of cenozoic seawater: Changes in silicate weathering and reverse weathering. Science 335, 818–823.

Morris, A.W., Howland, R.J.M., Bale, A.J., 1986. Dissolved aluminium in the Tamar Estuary, southwest England. Geochim. Cosmochim. Acta 50, 189–197.

Murphy, M.J., Pogge von Strandmann, P.A.E., Porcelli, D., Ingri, J., 2014. Li isotope behaviour in the low salinity zone during estuarine mixing. Procedia Earth Planet. Sci. 10, 204–207.

Nittrouer, C.A., DeMaster, D.J., 1996. The Amazon shelf setting: tropical, energetic, and influenced by a large river. Cont. Shelf Res. 16, 553–573.

Oelkers, E.H., Gislason, S.R., Eiriksdottir, E.S., Jones, M., Pearce, C.R., Jeandel, C., 2011. The role of riverine particulate material on the global cycles of the elements. Appl. Geochem. 26, S365–S369.

Parkhurst, D.L., Appelo, C.A.J., 2013. Description of input and examples for PHREEQC version 3—A computer program for speciation, batch-reaction, one-dimensional transport, and inverse geochemical calculations. US Geol. Surv. Tech. Methods 6, 497.

Pistiner, J.S., Henderson, G.M., 2003. Lithium-isotope fractionation during continental weathering processes. Earth Planet. Sci. Lett. 214, 327–339.

Pogge von Strandmann, P.A.E., Henderson, G.M., 2015. The Li isotope response to mountain uplift. Geology 43, 67–70.

Pogge von Strandmann, P.A.E., James, R.H., van Calsteren, P., Gíslason, S.R., Burton, K.W., 2008. Lithium, magnesium and uranium isotope behaviour in the estuarine environment of basaltic islands. Earth Planet. Sci. Lett. 274, 462–471.

Pogge von Strandmann, P.A.E., Fraser, W.T., Hammond, S.J., Tarbuck, G., Wood, I.G., Oelkers, E.H., Murphy, M.J., 2019a. Experimental determination of Li isotope behaviour during basalt weathering. Chem. Geol. 517, 34–43.

Pogge von Strandmann, P.A.E., Schmidt, D.N., Planavsky, N.J., Wei, G., Todd, C.L., Baumann, K.H., 2019b. Assessing bulk carbonates as archives for seawater Li isotope ratios. Chem. Geol. 530, 119338.

Pogge von Strandmann, P.A.E., Kasemann, S.A., Wimpenny, J.B., 2020. Lithium and lithium isotopes in Earth's surface cycles. Elements 16, 253–258.

Pogge von Strandmann, P.A.E., Dellinger, M., West, A.J., 2021. Lithium isotopes: a tracer of past and present silicate weathering. In: Lyons, T., Turchyn, A., Reinhaed, C. (Eds.), Geochemical Tracers Earth Eystem Science. Cambridge University Press, Cambridge, pp. 1–24.

Pogge von Strandmann, P.A.E., Liu, X., Liu, C.Y., Wilson, D.J., Hammond, S.J., Tarbuck, G., Aristilde, L., Krause, A.J., Fraser, W.T., 2022. Lithium isotope behaviour during basalt weathering experiments amended with organic acids. Geochim. Cosmochim. Acta 328, 37–57.

Porcelli, D., Andersson, P.S., Wasserburg, G.J., Ingri, J., Baskaran, M., 1997. The importance of colloids and mires for the transport of uranium isotopes through the Kalix River watershed and Baltic Sea. Geochim. Cosmochim. Acta 61, 4095–4113.

Revels, B.N., Rickli, J., Moura, C.A.V., Vance, D., 2021a. Nickel and its isotopes in the Amazon Basin: the impact of the weathering regime and delivery to the oceans. Geochim. Cosmochim. Acta 293, 344–364.

Revels, B.N., Rickli, J., Moura, C.A.V., Vance, D., 2021b. The riverine flux of molybdenum and its isotopes to the ocean: weathering processes and dissolved-particulate partitioning in the Amazon basin. Earth Planet. Sci. Lett. 559, 116773.

Sayles, F.L., Mangelsdorf Jr., P.C., 1979. Cation-exchange characteristics of Amazon River suspended sediment and its reaction with seawater. Geochim. Cosmochim. Acta 43, 767–779.

Schroth, A.W., Crusius, J., Hoyer, I., Campbell, R., 2014. Estuarine removal of glacial iron and implications for iron fluxes to the ocean. Geophys. Res. Lett. 41, 3951–3958.

Seyfried, W.E., Janecky, D.R., Mottl, M.J., 1984. Alteration of the oceanic crust: Implications for geochemical cycles of lithium and boron. Geochim. Cosmochim. Acta 48 (3), 557–569.

Shalev, N., Bontognali, T.R.R., Wheat, C.G., Vance, D., 2019. New isotope constraints on the Mg oceanic budget point to cryptic modern dolomite formation. Nat. Commun. 10, 5646.

Sholkovitz, E.R., 1978. The flocculation of dissolved Fe, Mn, Al, Cu, Ni, Co and Cd during estuarine mixing. Earth Planet. Sci. Lett. 41, 77–86.

Spiegel, T., Vosteen, P., Wallmann, K., Paul, S.A.L., Gledhill, M., Scholz, F., 2021. Updated estimates of sedimentary potassium sequestration and phosphorus release on the Amazon shelf. Chem. Geol. 560, 120017.

Sposito, G., Skipper, N.T., Sutton, R., Park, S.H., Soper, A.K., Greathouse, J.A., 1999. Surface geochemistry of the clay minerals. PNAS 96, 3358–3364.

Stallard, R.F., 1985. River chemistry, geology, geomorphology, and soils in the Amazon and Orinoco basins. In: Drever, J.I. (Ed.), The Chemistry of Weathering. D. Reidel Publishing Company, Holland, pp. 293–316.

Stoffyn-Egli, P., 1982. Conservative behaviour of dissolved lithium in estuarine waters. Estuar. Coast. Shelf Sci. 14, 577–587.

Tessier, A., Campbell, P.G.C., Bisson, M., 1979. Sequential extraction procedure for the speciation of particulate trace metals. Anal. Chem. 51, 844–851.

Tipper, E.T., Galy, A., Gaillardet, J., Bickle, M.J., Elderfield, H., Carder, E.A., 2006. The magnesium isotope budget of the modern ocean: constraints from riverine magnesium isotope ratios. Earth Planet. Sci. Lett. 250, 241–253.

Tipper, E.T., Stevenson, E.I., Alcock, V., Knight, A.C.G., Baronas, J.J., Hilton, R.G., Bickle, M.J., Larkin, C.S., Feng, L., Relph, K.E., Hughes, G., 2020. Global silicate

weathering flux overestimated because of sediment-water cation exchange. Proc. Natl. Acad. Sci. U. S. A. 118, e2016430118.

Tomascak, P.B., Magna, T., Dohmen, R., 2016. Advances in Lithium Isotope Geochemistry. Springer International Publishing, Switzerland.

Velde, B., 1995. Origin and Mineralogy of Clays. Springer, Germany.

Viers, J., Dupré, B., Gaillardet, J., 2009. Chemical composition of suspended sediments in World Rivers: New insights from a new database. Sci. Total Environ. 407, 853–868.

Vigier, N., Decarreau, A., Millot, R., Carignan, J., Petit, S., France-Lanord, C., 2008. Quantifying Li isotope fractionation during smectite formation and implications for the Li cycle. Geochim. Cosmochim. Acta 72, 780–792.

Vital, H., Stattegger, K., 2000. Major and trace elements of stream sediments from the lowermost Amazon River. Chem. Geol. 168, 151–168.

Vosteen, P., Spiegel, T., Gledhill, M., Frank, M., Zabel, M., Scholz, F., 2022. The fate of sedimentary reactive iron at the land-ocean interface: A case study from the Amazon shelf. Geochem. Geophys. 23, e2022GC010543.

Walker, J.C.G., Hays, P.B., Kasting, J.F., 1981. A negative feedback mechanism for the long-term stabilization of Earth's surface temperature. J. Geophys. Res. 86, 9776–9782.

White, W.M., 2013. Geochemistry. Wiley-Blackwell, UK.

Wilson, S., 1998. United States Geological Survey certificate of cnalysis basalt, Columbia River, BCR-2. United States Geological Survey Report.

Wilson, D.J., Pogge von Strandmann, P.A.E., White, J., Tarbuck, G., Marca, A.D., Atkinson, T.C., Hopley, P.J., 2021. Seasonal variability in silicate weathering signatures recorded by Li isotopes in cave drip-waters. Geochim. Cosmochim. Acta 312, 194–216.

Wimpenny, J., Gíslason, S.R., James, R.H., Gannoun, A., Pogge von Strandmann, P.A.E., Burton, K.W., 2010a. The behaviour of Li and Mg isotopes during primary phase dissolution and secondary mineral formation in basalt. Geochim. Cosmochim. Acta 74, 5259–5279.

Wimpenny, J., James, R.H., Burton, K.W., Gannoun, A., Mokadem, F., Gíslason, S.R., 2010b. Glacial effects on weathering processes: New insights from the elemental and lithium isotopic composition of West Greenland rivers. Earth Planet. Sci. Lett. 290, 427–437.

Wimpenny, J., Colla, C.A., Yu, P., Yin, Q.Z., Rustad, J.R., Casey, W.H., 2015. Lithium isotope fractionation during uptake by gibbsite. Geochim. Cosmochim. Acta 168, 133–150.

Wooster, W.S., Lee, A.J., Dietrich, G., 1969. Redefinition of salinity. Limnol. Oceanogr. 14, 437–438.

Yang, C., Vigier, N., Lian, E., Lai, Z., Yang, S., 2021. Decoupling of dissolved and particulate Li isotopes during estuarine processes. Geochem. Perspect. Lett. 19, 40–44.

Yao, P., Zhao, B., Bianchi, T.S., Guo, Z., Zhao, M., Li, D., Pan, H., Wang, J., Zhang, T., Yu, Z., 2014. Remineralization of sedimentary organic carbon in mud deposits of the Changjiang Estuary and adjacent shelf: Implications for carbon preservation and authigenic mineral formation. Cont. Shelf Res. 91, 1–11.

Zhang, L., Chan, L.H., Gieskes, J.M., 1998. Lithium isotope geochemistry of pore waters from Ocean Drilling Program Sites 918 and 919, Irminger Basin. Geochim. Cosmochim. Acta 62, 2437–2450.

Zhu, X., Zhang, R., Wu, Y., Zhu, J., Bao, D., Zhang, J., 2018. The remobilization and removal of Fe inestuary—A case study in the Changjiang estuary, China. J. Geophys. Res. Ocean. 123, 2539–2553.

Supplementary Material for:

The influence of river-derived particles on estuarine and marine elemental cycles: evidence from lithium isotopes

Authors: Chun-Yao Liu[a]*, David J. Wilson[a], Ed C. Hathorne[b], Antao Xu[b], Philip A. E. Pogge von Strandmann[a,c]

[a] London Geochemistry and Isotope Centre (LOGIC), Institute of Earth and Planetary Sciences, University College London and Birkbeck, University of London, Gower Street, London WC1E 6BT, UK

[b] GEOMAR Helmholtz Centre for Ocean Research Kiel, Wischhofstrasse 1-3, Kiel 24148, Germany

[c] Mainz Isotope Geochemistry (MIGHTY), Institute of Geosciences, Johannes Gutenberg University, 55122, Mainz, Germany

* Corresponding author. e-mail: chunyao.liu.19@ucl.ac.uk

S1. Comparison of bulk elemental compositions obtained by different methods (calculation vs. measurement).

The MUC samples in this study are the uppermost 0.5–2 cm of sediment for each core at sampling locations from the GEOTRACES M147 cruise. The M147 cruise also obtained sediment samples at different depths of more than one core at each sampling location for other scientific topics (Koschinsky et al., 2018, Spiegel et al., 2021, Vosteen et al., 2022). Using these samples, Spiegel et al. (2021) obtained the concentrations of Li, Ca, Mg, K, Fe, Mn and Al of MUC24, MUC41, MUC67, MUC73, MUC85, MUC89, MUC93, MUC108 and MUC117 by ICP-OES after dissolving bulk samples in $HF-HClO_4-HNO_3$, and Vosteen et al. (2022) obtained the concentrations of K, Fe, and Al of MUC24, MUC41, MUC85, MUC89, MUC93 and MUC117 by ICP-OES after dissolving bulk samples in $HF-HClO_4-HNO_3$. Here, the average elemental compositions of the sediments at 0–1 cm and 1–2 cm from Spiegel et al. (2021) and Vosteen et al. (2022) are compared with the bulk elemental compositions calculated based on the chemical extraction data in this study.

The relative standard deviations (RSD) between $[Li]_{bulk}$ from this study and the measured bulk Li concentrations (Spiegel et al., 2021) are 1.0% to 22.9% (4 samples < 5%; 4 samples at 5–15%; 1 sample at 22.9%). The average RSD between the concentrations of Ca, Mg, K, Fe, Mn and Al in the bulk samples obtained in this study and in Spiegel et al. (2021) are 20%, 18%, 10%, 8%, 11% and 20%, respectively. The RSD between the concentrations of K, Fe and Al in the bulk samples obtained in this study and Vosteen et al. (2022) are 0.9–28.0% (mostly 0.9–3.8%, plus only one at 28.0%), 0.1–7.6% and 1.4–8.9%, respectively. The differences may be due to analytical precision and/or natural variability due to differences between sampled cores

during the GEOTRACES M147 cruise, where more than one core was collected at each sampling site (Koschinsky et al., 2018).

S2. The chemical extracted phases of the sediments

S2.1 Influence of the remaining dissolved load on the exchangeable pool

The process of sampling and the existence of pore water could potentially influence the suspended load sediment (SPM) and/or surface sediment (MUC) samples. The river water or seawater may attach to the SPM and MUC samples, although both the MUC and SPM samples were separated by centrifugation before freeze drying (Section 2.2) (Koschinsky et al., 2018). Theoretically, some of the elements in this dissolved material could remain in the SPM and MUC samples, and would likely be re-dissolved in the leachates of the first phase (i.e., exchangeable pool).

Based on the elemental concentrations of the dissolved load samples from the Amazon south channel transect, the Ca/Li, Mg/Li and K/Li ratios of the riverine endmember are 6.9, 3.5 and 1.9 g/mg, respectively, and these ratios are 2.4, 7.3 and 2.4 g/mg in seawater. The δ^7Li value of the riverine endmember is 23.7‰, and in saline water it ranges from 29.4–32.8‰. Basically, the Ca/Li, Mg/Li, and K/Li ratios in the pore water of the ocean surface sediments are similar to the overlying saline water (Smrzka et al., 2019; Andrews et al., 2020). Previous studies also confirm that Li concentrations and isotope compositions in the pore waters of surface ocean sediments are similar to seawater (Zhang et al., 1998; Andrews et al., 2020). In contrast, the $[Ca]_{exchangeable}/[Li]_{exchangeable}$, $[Mg]_{exchangeable}/[Li]_{exchangeable}$ and $[K]_{exchangeable}$ $/[Li]_{exchangeable}$ ratios of both the SPM and MUC samples do not exhibit typical seawater

elemental ratios or a binary mixing trend between seawater and clay compositions (Fig. S1) (Yang et al., 2021). Furthermore, the SPM samples from the Amazon north channel fit the trend of the MUC samples from the Amazon north channel transect (Fig. S1), even though the SPM and MUC samples were sampled and treated by different methods in the field (Section 2.2). In addition, two SPM samples (SPM8s and SPM8d) are from the same location but different water depths, and therefore different salinities (20 and 24, respectively), yet show similar $[Ca]_{exchangeable}$, $[Mg]_{exchangeable}$, $[K]_{exchangeable}$, $[Li]_{exchangeable}$ and $\delta^7Li_{exchangeable}$ (Table 2). The $[Ca]_{exchangeable}$, $[Mg]_{exchangeable}$ and $[K]_{exchangeable}$ values are within the ranges of concentrations of exchangeable Ca, Mg and K in of Sayles and Mangelsdorf (1979). The above evidence therefore supports that any remaining ambient waters (i.e., saline water and/or pore water) have a negligible influence on the extracted exchangeable pool.

S2.2 Elemental concentrations in exchangeable pool

Apart from Na, which was added from the leaching reagents (NaOAc), the exchangeable pool of both SPM and MUC samples are dominated by Mg, Ca and K, whereas the Fe, Al and Mn contents are very low (Fig. S2, Table 2 in main text). In the north channel transect, the $[Ca]_{exchangeable}$ fluctuates from 0.68 to 0.85 mg/g at low and medium salinity and increases to 1.54 mg/g at high salinity. The $[Mg]_{exchangeable}$ increases from 0.51 mg/g in the river endmember to 1.17 mg/g at low salinity, and then fluctuates from 1.16 to 1.41 mg/g at higher salinities. The $[K]_{exchangeable}$ generally increases through the transect from 0.12 to 1.06 mg/g. In the alongshore transect, $[K]_{exchangeable}$ generally remains constant, whereas $[Ca]_{exchangeable}$ and $[Mg]_{exchangeable}$ increase from 0.81 to 1.63 mg/g, and from 1.39 to 1.87 mg/g, respectively.

S2.3. Influences on carbonate leachates

The sample 41MUC contains 39.7% carbonate, based on the total inorganic carbonate analysis (Spiegel et al., 2021). Its $[Ca]_{carbonate}$ is 66.9 mg/g, which is around 80 times higher than its $[Mg]_{carbonate}$, which indicates that calcium carbonate dominates its carbonate leachates. The $[Mn]_{carbonate}/[Ca]_{carbonate}$ and $[Al]_{carbonate}/[Ca]_{carbonate}$ ratios are 0.30 mg/g and 0.13 mg/g, respectively. Furthermore, the $[Ca]_{oxide}$ of 41MUC is 120 mg/g, which is higher than its $[Ca]_{carbonate}$, indicating that the oxide leachates of 41MUC are likely to be influenced by carbonates that were not fully leached in the previous step. This scenario likely arises because our leaching method is primarily designed for silicate soils, sediments and rocks, with carbonate contents at least less than 15% and ideally less than 5% (Liu et al., 2022). The $[Li]_{carbonate}$ of 41MUC is 0.33 μg/g, which represents only approximately 1% of the Li in the bulk sample, while the $\delta^7Li_{carbonate}$ value of 41MUC is 14.9‰.

Apart from sample 41MUC, the operationally-defined carbonate leachates of the other MUC and SPM samples are likely to be partly influenced by leaching of other phases, due to their low carbonate contents. Most of the suspended particles transported by the Amazon river to the estuary are derived from the Andes mountains, where the rocks rarely contain carbonates (Gibbs, 1967; Kuehl et al., 1982; Baturin and Gordeev, 2019). Furthermore, the calculated saturation index (SI) of carbonates in the river endmember (W66) and the pH of the Amazon mainstream of around 6.8 indicate that carbonate precipitation is not favourable in this river system (Fig. S5) (Dellinger et al., 2015).

The $[Ca]_{carbonate}/[Mg]_{carbonate}$ and $[Ca]_{carbonate}/[Ca]_{exchangeable}$ ratios of the sediment samples

(except 41MUC) range from 0.6 to 8.7 and from 0.25 to 3.85, respectively, without clear trends. These data indicate a lack of significant calcium carbonate content in these sediments, and therefore clays may influence the carbonate leachates (Liu et al., 2022). Furthermore, except for sample 41MUC, the $[Mn]_{carbonate}/[Ca]_{carbonate}$ ratios range from 34 to 253 mg/g, and $[Al]_{carbonate}/[Ca]_{carbonate}$ ratios range from 4 to 118 mg/g. In contrast, the Mn/Ca ratios in leachates of carbonate-dominated samples range from 0.1 μg/g to 35 mg/g (Misra and Froelich, 2012; Pogge Von Strandmann et al., 2013, 2019b, 2021; Ullmann et al., 2013; Bastian et al., 2018; Dellinger et al., 2020; Washington et al., 2020), while the recommended Al/Ca ratios in carbonate leachates should be less than 0.54 mg/g (i.e., 0.8 mmol/mol) (Pogge Von Strandmann et al., 2013) or even less than 0.27 mg/g (i.e., 0.4 mmol/mol) (Dellinger et al., 2020). Except for 41MUC, the $\delta^7Li_{carbonate}$ values of the other sediments lie between their corresponding $\delta^7Li_{exchangeable}$ and δ^7Li_{oxide} values (Fig. 3 in main text). The above evidence suggests that, when the carbonate content in the sediments is low (Spiegel et al., 2021), the operationally-defined carbonate leachates are probably not dominated by carbonate, but may be influenced by the dissolution of other phases instead (Liu et al., 2022).

S2.4 Oxide leachates

The oxide leachate of 41MUC is likely influenced by additional leaching of carbonate remaining from the previous step due to its high carbonate content (Supplementary Material S2.3). For all other samples, Fe, Mn and Al dominate the oxide leachates of the MUC and SPM samples (Fig. S2). For example, $[Ca]_{oxide}/[Fe]_{oxide}$, $[Mg]_{oxide}/[Fe]_{oxide}$, and $[K]_{oxide}/[Fe]_{oxide}$ of the sediments range from 0.13–0.41 g/g, 0.05–0.17 g/g, and 0.02–0.18 g/g, respectively.

However, it is difficult to completely avoid interference from clay phases (Supplementary Material S3; Liu et al., 2022). In that context, it is worth noting that $[Mg]_{oxide}$ and $[K]_{oxide}$, which usually enter clays instead of oxides, increase with salinity in the Amazon north channel transect from 0.02 to 0.2 mg/g and from 0.02 to 0.14 mg/g, respectively.

In the north channel transect, $[Fe]_{oxide}$ generally increases from 0.47 to 1.53 mg/g with salinity (Fig. S2). Meanwhile, $[Fe]_{oxide}/[Fe]_{bulk}$ fluctuates at around 1.5% from the river endmember up to medium salinity, then increases to 3.6% at a salinity of ~20. In the alongshore transect, $[Fe]_{oxide}$ remains stable at around 1.0 mg/g. For $[Mn]_{oxide}$, one ocean surface sediment sample, 85MUC, located at the intersection of the north channel transect and the alongshore transect has low $[Mn]_{oxide}$ (0.03 mg/g). Except for 85MUC and 41MUC, the $[Mn]_{oxide}$ in the north transect varies in a narrow range from 0.17 to 0.24 mg/g; these values are higher than $[Mg]_{oxide}$ and $[K]_{oxide}$ in all the sediments, and higher than $[Ca]_{oxide}$ at low and medium salinity. The $[Mn]_{oxide}/[Mn]_{bulk}$ is in the range of 20.0 to 32.3% (except for 85MUC at 6.0% and 41MUC at 60.4%). For $[Al]_{oxide}$, the values range from 0.08 to 0.22 mg/g and show no clear trend with salinity in the offshore transect or with distance from the river mouth in the alongshore transect.

S2.5 Clay phase

In the clay phase of most of the MUC and SPM samples (except for 41MUC), Fe and Al are the dominant cations (Fig. S2). The clay leachate of sediment 41MUC also shows a high $[Ca]_{clay}$ of 5.78 mg/g, whereas in the other samples the $[Ca]_{clay}$ is lower and stable at around 0.35 mg/g, except for slightly higher values in 117MUC (0.62 mg/g). Except for 41MUC, $[Fe]_{clay}$ increases from 2.04 to 3.39 mg/g at the beginning of the Amazon north channel transect,

then increases slightly to 4.29 mg/g, and it fluctuates at 3.7–5.0 mg/g in the alongshore transect. For $[Al]_{clay}$, the riverine endmember of the north channel transect has 0.57 mg/g, and it then varies from 0.94 to 1.25 mg/g in the other sediments. Both $[Mg]_{clay}$ and $[K]_{clay}$ in the north channel transect increase continuously with salinity, from 0.09 to 0.49 mg/g, and from 0.02 to 0.13 mg/g, respectively.

S2.6 Residue and bulk sediments

The concentrations of Ca, Mg, K, Fe, Mn, Al and Li in the bulk sediments are calculated using Eq. (2) in the main text. Among these elements, the $[Al]_{bulk}$ is highest, followed by $[Fe]_{bulk}$, $[K]_{bulk}$, $[Mg]_{bulk}$, $[Ca]_{bulk}$ and $[Mn]_{bulk}$. In the north channel transect, the $[Ca]_{bulk}$ is 6.87 mg/g in the river endmember, remains stable at around 4.5 mg/g at low and medium salinity, and increases to 197 mg/g in the carbonate-dominated sediment 41MUC. In contrast, in that same transect, the $[Fe]_{bulk}$, $[Al]_{bulk}$, $[Mg]_{bulk}$ and $[K]_{bulk}$ increase in the low salinity zone, and then remain relatively constant at around 1.6 times the river endmember at medium salinity, before decreasing at high salinity.

S3. Cation retention by oxides

Except for sample 41MUC, which contains 39.7% carbonate (Supplementary Material S2), Fe, Mn and Al dominate the oxide leachates of the MUC and SPM samples (Fig. S2). This observation indicates that the HH leaching probably attacked Fe/Mn oxides (e.g., ferrihydrite, lepidocrocite, goethite and pyrolusite) and Al oxides (i.e., gibbsite), as expected (Velde, 1995; Bigham et al., 2002; Poulton and Canfield, 2005; Lenstra et al., 2021; Liu et al., 2022). Except

for sample 41MUC, the $[Fe]_{oxide}$ in the other leachates shows a positive relationship with $[Li]_{oxide}$ (Fig. S4). In contrast, $[Mn]_{oxide}$ and $[Al]_{oxide}$ are generally constant through the estuary and do not show clear relationships with $[Li]_{oxide}$ (Fig. S4). The different trends between $[Fe]_{oxide,}$ $[Mn]_{oxide}$ and $[Al]_{oxide}$ may imply that there is less formation of Mn-oxides (e.g., Mn-nodules, pyrolusite or birnessite) and Al-oxides (i.e., gibbsite), and more formation of Fe-oxides (e.g., ferrihydrite, lepidocrocite and goethite) through the Amazon estuary. Such a scenario seems reasonable because Fe removal in estuaries is regarded as highly related to flocculation (Boyle et al., 1977; Sholkovitz et al., 1978), whereas Mn cycling is more closely related to redox conditions (Sholkovitz, 1978; Chester, 1990). In addition, Fe removal in the estuary could also be due to Fe-rich clay formation (Michalopoulos and Aller, 1995). Furthermore, $[Mg]_{oxide}$ also increases through the estuary and shows a positive linear relationship with $[Li]_{oxide}$, while the $[Mg]_{oxide}/[Li]_{oxide}$ ratio is the same as in the clay phase (Fig. 8 in main text and Fig. S4). Since Amazon sediments contain more secondary clays than secondary oxides (Martinelli et al., 1993), the oxide leachates may be additionally influenced by inadvertent leaching of the clay or residue (Liu et al., 2022).

S4. Fractionation model for Li removal from the dissolved load into sediments

As discussed in Section 5.1.2, the exchangeable, oxide and clay phases of the sediments appear to remove Li from the saline water in the Amazon estuary with an accompanying isotopic fractionation. In the dissolved load, $[Li]_{measured}$ generally shows conservative mixing, but the measured lithium isotopic compositions ($\delta^7 Li_{measured}$) are slightly higher than predicted for conservative mixing ($\delta^7 Li_{conservative}$), especially at medium salinity.

Here, Rayleigh models (Eq. (S1)) and batch models (Eq. (S2)) are fitted to explore the influence of sediment Li uptake from the dissolved load (Dellinger et al., 2015; Murphy et al., 2019; Pogge von Strandmann et al., 2019a; Yang et al., 2021).

$$\delta^7\text{Li}_{\text{after-removal}} = \delta^7\text{Li}_{\text{conservative}} + 1000 \times (\alpha - 1) \times \ln(f) \quad \text{(S1)}$$

$$\delta^7\text{Li}_{\text{after-removal}} = \delta^7\text{Li}_{\text{conservative}} + 1000 \times \ln(\alpha) \times (f - 1) \quad \text{(S2)}$$

$$[\text{Li}]_{\text{after-removal}} = [\text{Li}]_{\text{conservative}} \times f \quad \text{(S3)}$$

The terms $[\text{Li}]_{\text{conservative}}$ and $\delta^7\text{Li}_{\text{conservative}}$ are the Li concentration and Li isotope composition in the dissolved load calculated based on conservative mixing. Because the measured dissolved Li concentrations conform to conservative mixing, the $[\text{Li}]_{\text{conservative}}$ here is the same as $[\text{Li}]_{\text{measured}}$ in Eq (4) in the main text. In the model, six $[\text{Li}]_{\text{conservative}}$ points are designated as 4.99 μg/L (sample W70), 10.99 μg/L (sample W69), 33.96 μg/L (sample W80), 49.10 μg/L (sample W79), 99.11 μg/L (sample W75) and 150.65 μg/L (sample W56fish) (Table S4), based on the Li concentrations in the dissolved load in the south channel transect. The terms $[\text{Li}]_{\text{after-removal}}$ and $\delta^7\text{Li}_{\text{after-removal}}$ are the Li concentration and Li isotope composition in the dissolved load after Li removal by sediments, and α is the fractionation factor between specific sediment phases and seawater. As outlined in Section 5.1.2, the leachate data indicate that $\alpha_{\text{exchangeable-seawater}}$ is approximately 0.9860–0.9935 and $\alpha_{\text{oxide/clay-seawater}}$ is approximately 0.9714–0.9757. Therefore, in the following modelling, $\alpha_{\text{exchangeable-seawater}}$ is set as 0.9900 ± 0.0050 and $\alpha_{\text{oxide-seawater}}$ and $\alpha_{\text{clay-seawater}}$ are set as 0.9750 ± 0.0050 (Table S4). These α values are similar to, or slighter smaller than, reported in previous studies (Pistiner and Henderson, 2003; Chan and Hein, 2007; Pogge von Strandmann et al., 2008, 2019a, 2020; Wimpenny et al., 2010; Hindshaw et al., 2018; Li and Liu, 2020; Li et al., 2020). The term f is the fraction of Li that

remains in the dissolved load after removal into the solid phases, and is calculated from Eq. (S4).

$$f = 1 - SSC \times [Li]_{sediment\ added} / [Li]_{conservative} \quad (S4)$$

Here, SSC is the suspended sediment concentration, and $[Li]_{sediment\ added}$ is the mass of Li per gram that is gained by the sediments.

In the Amazon estuary, the SSC in the surface layer (<3 m) is greater than 0.2 g/L just off the river mouth, greater than 0.5 g/L in the muddy area in the middle of the estuary, but less than 0.1 g/L towards the end of the estuary (Gibbs, 1976; Kineke et al., 1996). The average SSC in the Amazon river estuary has also been calculated as 0.19 g/L based on the Amazon river annual discharge of water and its particle load (Gaillardet et al., 1999; Milliman and Farnsworth, 2011). The SSC of samples SPM27–31 range from 0.26 g/L to 0.59 g/L (Table S2). To explore the influence of the SSC, the value of SSC is set at three levels: 0.1, 0.5 and 1.0 g/L (Table S4).

In the Amazon north channel transect, the maximum Li added to the estuarine sediments compared to the riverine endmember (i.e., $[Li]_{sediment\ added}$) is 0.23 μg/g in exchangeable phases, 0.32 μg/g in oxide phases, and 0.67 μg/g in clay phases. According to the two sediment samples from the Amazon south channel transect (i.e., 67MUC and 73MUC), the sediments take up 0.18 μg/g in exchangeable phases, 0.11 μg/g in oxide phases, and 0.38 μg/g in clay phases. For the alongshore transect, the maximum Li added to the sediments (relative to the river endmember) is 0.26 μg/g in exchangeable phases, 0.33 μg/g in oxide phases, and 1.02 μg/g in clay phases. However, because the clay leaching method is designed to obtain the Li isotope composition of the clay phase rather than to quantitatively leach the entire clay phase (Liu et

al., 2022; Pogge von Strandmann et al., 2022), the amount of Li removed into the clay phase may be underestimated in this case. According to mineralogical studies, clay minerals could account for up to 50% of the Amazon river sediments (Martinelli et al., 1993). However, the residue after the clay leaching shows stable $\delta^7Li_{residue}$ values through the estuary (Fig. 9 in main text), so the residue appears to be negligibly influenced by the clay that is remaining after clay extraction. Based on mass balance considerations, the Li from any remaining clays should represent less than 20% of the total Li in the bulk sediments; otherwise, the δ^7Li values in the residue should be observed to increase with salinity, in a similar manner to the clay leachates, which is not seen. Therefore, we consider that the $[Li]_{sediment\ added}$ could potentially comprise up to a maximum of 10 µg/g. Thus, $[Li]_{sediment\ added}$ in the exchangeable phases is set as 0.2 and 0.3 µg/g (Table S4). Because of their similar fractionation factors, the oxide and clay phases can be treated as one phase with $[Li]_{sediment\ added}$ values set as 0.5, 1.0, 2.0, 5.0 and 10.0 µg/g. (Table S4).

The results of the modelling demonstrate that the Li adsorbed by the exchangeable phases rarely affects either the $[Li]_{conservative}$ or the $\delta^7Li_{conservative}$ values in the dissolved load (Table S4), while the Li removed by oxides and clay phases could increase the $\delta^7Li_{conservative}$ values without significant alteration of the $[Li]_{conservative}$ in the dissolved load. The exchangeable phases achieve a maximum adsorption of 4.2 ± 1.9% of the dissolved load Li at very low $[Li]_{conservative}$ of 5 ng/g (assuming water density as 1 g/mL), and as a result the δ^7Li value in the dissolved load can only increase by 0.28 ± 0.25‰. At a higher salinity (higher dissolved Li concentration), exchangeable phases scavenge less than 3%, and generally less than 1%, of the Li from the dissolved load. This relatively small amount of Li uptake leads to very little increase (less than

0.3‰) in the dissolved δ^7Li values. Thus, due to the relatively small amount of Li removal and the modest isotopic fractionation, the exchangeable phase negligibly changes the dissolved Li behaviour, and hence there is no discernible deviation from conservative mixing (Fig. 2 in main text).

In contrast, due to the large isotopic fractionation ($\alpha_{clay/oxide-seawater} = 0.9750 \pm 0.0050$), dissolved δ^7Li values can be increased by 2.0–3.2‰ by oxide/clay uptake if f is 0.90 (i.e., 10% removal), and by 4.0–6.7‰ if f is 0.80 (i.e., 20% removal). However, the observed conservative mixing for dissolved Li concentrations in the Amazon estuary provides a constraint on f, which has to remain higher than 0.95 (based on the analytical uncertainty of the Li concentrations). Thus, dissolved δ^7Li values could be increased by 1.0–1.5‰ by oxide/clay uptake, when f is 0.95 (Table S4, Fig. 5 in main text), which may explain the higher measured dissolved δ^7Li values in the medium salinity zone than those calculated based on conservative mixing.

In the modelling, the key controlling factors on f are [Li]$_{sediment\ added}$ and SSC. For Li removal by oxides/clays, when the SSC is 0.1 g/L, and [Li]$_{sediment\ added}$ is 0.5 or 1 μg/g, the value of f at all modelled salinity values is higher than 0.98, which causes less than a 0.6‰ increase in dissolved load δ^7Li values (Table S4, Fig. 5 in main text). In contrast, if SSC is 1 g/L and [Li]$_{sediment\ added}$ is 5 or 10 μg/g, the value of f is less than 0.50 in the low salinity zone, and around 0.80 at medium salinity. In that case, there would be significant Li uptake, and the mixing of dissolved Li would be readily observed as non-conservative. According to our dissolved Li data from the Amazon, at very low salinity (0–0.5), the Li concentrations and isotopes show conservative mixing (Fig. 5b in main text), consistent with little resolvable Li uptake by particles. Similarly, at low salinity (1–7), no significant Li isotopic fractionation is observed,

although Li removal could be relatively greater with f being 0.99 to 0.98 with approximately

0.2 g/L SSC (Gibbs, 1976) and 1–2 µg/g [Li]$_{sediment\ added}$. At medium salinity (9–18), $\delta^7Li_{measured}$

values are 1–2‰ higher than expected for conservative mixing (Fig. 5b in main text). Such

values could arise in a scenario with more Li removal under conditions of 0.5g/L SSC (Gibbs,

1976) and 4–5 µg/g [Li]$_{sediment\ added}$, enabling a lowering of f to 0.95 (remaining consistent with

the concentration data). At higher salinity (> 20), due to the high dissolved Li concentrations

and lower SSC, the amount of particle Li uptake could only comprise a relatively small fraction

of the Li budget, and does not cause resolvable Li isotope fractionation. Overall, for the

Amazon estuary as a whole, based on the assumption that 70% of the river-derived particles

are deposited on the seafloor within 200 km from the river mouth (corresponding to sample

85MUC from the Amazon north channel and W79 from the Amazon south channel at medium

salinity) (Kineke et al., 1996), we estimate that the average [Li]$_{sediment\ added}$ is 3–4 µg/g.

S5. Estuary model for estimating the Li removal flux during estuarine processes

The conservative mixing model (Section 5.1.1) and fractionation model (Section 5.1.3 and

Supplementary Material S4) are combined to quantify the fate of dissolved Li in the entire

Amazon estuary. Here, the estuary is assumed to be at steady state, with the exchange of

material (i.e., water and particles) between the river, estuary, and ocean being stable with time,

and the geochemistry and particle distribution remaining constant with time. For the dissolved

load in the estuary, the inputs of dissolved Li are from river water, seawater, and sediment

dissolution (Fig. 6 in main text). However, the sediment samples indicate a net Li output rather

than Li input. Therefore, the input from sediment/mineral dissolution cannot be directly

quantified, and can be regarded as being offset by the removal. Note that, in basalt weathering experiments, only ~4% of the Li removed by secondary mineral formation was added by primary mineral dissolution (Pogge von Strandmann et al., 2019a), which suggests that the removal process may typically be dominant. The volume of river water ($V_{riverwater}$) input is regarded as constant throughout the whole estuary, since it represents the integration of river discharge over a period of time, with the Amazon river water input being around 6300 km^3 per year (Milliman and Farnsworth, 2011). Assuming that the Li concentration in the river water at the river mouth also remains stable, the total riverine Li input flux remains stable. In other words, the river water input is assumed to travel through the whole estuary and to mix into the body of ocean water on the shelf (Fig. 6 in main text).

Based on the mixing model, the total water volume ($V_{total} = V_{riverwater}/FV_{riverwater}$) and the seawater-contributed volume can be calculated, and both increase through the estuary (Fig. 6 in main text). Thus, the mass of Li from river water and seawater can be integrated as in Eqs. (S5) and (S6), and their ratio is as shown in Eq. (S7) (Table S5). The output of dissolved Li at steady-state arises from sediment uptake. According to the fractionation model, the fraction of Li that remains in the dissolved load after sediment uptake (f) was calculated to be 1.00, 0.98, 0.95 and 0.98 at very low, low, medium and high salinity, respectively (Table S5). Thus, the fraction of Li that remains in the dissolved load after sediment removal from the beginning of the Amazon estuary to the corresponding salinity point can be calculated as Σf (Eq. (S8)). The Σf_{river} is the fraction of Li supplied by the river water that remains in the dissolved Li supplied by the river water after Li removal by sediments accumulated to a given point in the estuary (Eq. (S9)). The $\Sigma f_{seawater}$ is the fraction of Li supplied by the seawater that remains in the

dissolved Li supplied by the seawater after Li removal by sediments accumulated to a given point in the estuary (Eq. (S10)).

$$MLi_{riverwater} = \int [Li]_{conservative} \times FLi_{riverwater}\, dv_{total} \quad (S5)$$

$$MLi_{seawater} = \int [Li]_{conservative} \times FLi_{seawater}\, dv_{total} \quad (S6)$$

$$MLi_{seawater} / MLi_{riverwater} = \frac{[Li]_{seawater}}{[Li]_{riverwater}} \times \left(\frac{V_{total} - V_{river}}{V_{river} \times \ln (V_{total}/V_{river})} - 1\right) \quad (S7)$$

$$\Sigma f = \int f \times [Li]_{conservative}\, dV_{total} / \int [Li]_{conservative}\, dV_{total} \quad (S8)$$

$$\Sigma f_{river} = \int f \times [Li]_{conservative} \times FLi_{riverwater}\, dV_{total} / \int [Li]_{conservative} \times$$

$$FLi_{riverwater}\, dV_{total} \quad (S9)$$

$$\Sigma f_{seawater} = \int f \times [Li]_{conservative} \times FLi_{seawater}\, dV_{total} / \int [Li]_{conservative} \times$$

$$FLi_{seawater}\, dV_{total} \quad (S10)$$

In the above equations, $MLi_{riverwater}$ and $MLi_{seawater}$ represent the mass of Li discharged by the river and the mass of Li from seawater participating in the conservative mixing. The terms $[Li]_{measured}$, $[Li]_{riverwater}$, $[Li]_{seawater}$, $FLi_{riverwater}$, $FLi_{seawater}$, V_{total}, $V_{riverwater}$, and $V_{seawater}$ are described in the conservative mixing calculation (Section 5.1.1). Here, Σf, Σf_{river} and $\Sigma f_{seawater}$ were calculated using a rectangular numerical integration method. To increase the accuracy of the numerical integration, the $[Li]_{conservative}$ was interpolated at every 1 µg/L from 1 to 150 µg/L (Table S5). The accuracy and precision of the rectangular numerical integration is verified based on the ratios of $MLi_{seawater}$ and $MLi_{riverwater}$, which are integrated as in Eqs (S5) and (S6) by rectangular numerical integration, being in the range from 0.9985 to 1.0000 of $MLi_{seawater}/MLi_{riverwater}$ calculated by Eq. (S7). The corresponding salinity is calculated using linear interpolation according to the $[Li]_{measured}$ between every measured samples.

Overall, these calculations indicate around 2–3% Li loss from the river water accumulated

from the beginning of the estuary to a salinity of above 9.3 in the Amazon estuary (Fig. 6 in main text and Table S5). Based on the Amazon river water discharge (~6300 km^3/yr) (Milliman and Farnsworth, 2011), and the measured dissolved Li concentration in the river water at its mouth (sample W66, 0.87 μg/L), the dissolved Li input flux from the Amazon river is 5.5×10^9 g/yr. Therefore, the Li loss from river water in the Amazon estuary is calculated to be around 1.1–1.7×10^8 g/yr, equivalent to 2–3% of the Amazon river dissolved Li flux.

From the sediment perspective, the total Li uptake by the sediment (Flux Li$_{\text{sediment removal}}$) can be calculated from Eq. S11. Here, the Load$_{\text{river sediment}}$ is the sediment mass transported by river water in a given time (i.e., erosion rate if calculated based on SSC) and assumed to be deposited only in the estuary area. The average [Li]$_{\text{sediment added}}$ is estimated to be 3–4 μg/g based on the fractionation model (Supplementary Material S4) and the Amazon sediment load is around 1.2×10^{12} kg/yr (Milliman and Farnsworth, 2011). Therefore, the total flux of dissolved Li removed by sediment in the Amazon estuary is 3.6–4.8×10^9 g/yr.

Flux Li$_{\text{sediment removal}}$ = Load$_{\text{river sediment}}$ × [Li]$_{\text{sediment added}}$ (S11)

If there is a simple mass balance in the estuary as a whole, the Li loss from the dissolved load (i.e., river water and seawater) should be equal to the Li gain in the sediment load. The Li removal mainly occurs at the beginning and middle of the estuary (Supplementary Material S4). According to Eq. (S7), integration of the seawater Li mass is ~36 times the river water Li mass from the river mouth to the middle of the estuary at a salinity of 9.3 (Fig. 6b, Table S5). In this case, around 1.0–1.3×10^8 g/yr of the Li uptake by sediment is from river water, which is around 1.8–2.4% of the dissolved Li flux of the Amazon river. More significantly, around 3.5–4.7×10^9 g/yr Li is removed from seawater by estuarine sediments in the Amazon estuary.

S6. Mineral stability and saturation

In estuaries, the mixing of river water and saline water leads to significant changes in the weathering environments for the particle loads transported by rivers, including changes in mineral saturation states. For example, the Amazon dissolved load samples show that the concentrations of Cl, Na, Mg, Ca and K rapidly increase, while the concentrations of dissolved SiO_4^{4-} and total dissolved nitrogen decrease (Table 1 in main text). Furthermore, the pH increases from around 7 in the river, to around 8.5 at medium salinity, and then decreases slightly to around 8.2 at high salinity. In this case, the predominant weathering products of feldspar shift from the kaolinite field (river) to the mica field (estuary) in the theoretical stability diagram (Fig. S3) (Tardy, 1971). The stability diagrams were plotted by PhreePlot (Kinniburgh and Cooper, 2011), with the database from PHREEQC (Parkhurst and Appelo, 2013) and Robie and Hemingway (1995). Compared to kaolinite ($Al_2Si_2O_5(OH)_4$), mica ($KAl_2[AlSi_3O_{10}](OH)_2$ or $NaAl_2[AlSi_3O_{10}](OH)_2$) could retain more cations (e.g., Na, K, Mg, Li).

Using PHREEQC (Parkhurst and Appelo, 2013), the saturation index (SI) for a range of minerals was calculated using input concentrations of Na, Ca, Mg, K, Li, NO_2^-, SiO_4^{4-}, NO_3^- and Cl^-, and alkalinity, temperature and pH (Table S6). As expected, carbonate minerals, such as calcite, aragonite and dolomite, rapidly shift from being undersaturated in the river water to being supersaturated in the saline water (Fig. S5). Salts (i.e., halite and sylvite) are undersaturated in the whole estuary, although their SI also increases with increasing salinity. Most importantly, the calculations show that silicate minerals, such as sepiolite and talc, are

highly supersaturated, with their SI increasing from around 10 in the river water to 17 at low to medium salinity and then decreasing slightly to around 14 at high salinity (Fig. S5). These calculated SIs support the removal of cations such as Mg and Li into sediment particles in the estuary.

S7. List of symbols in the modelling

$[Li]_{measured}$: Li concentration of each dissolved sample measured by ICP-MS.

$\delta^7 Li_{measured}$: Li isotope composition of each dissolved sample measured by MC-ICP-MS.

$[Li]_{riverwater}$: Li concentration of Amazon river water at the estuary, i.e., the Li concentration of sample W66.

$\delta^7 Li_{riverwater}$: Li isotope composition of Amazon river water at the estuary, i.e., the Li isotope composition of sample W66.

$[Li]_{seawater}$: Li concentration of modern seawater, i.e., 180 µg/L.

$\delta^7 Li_{seawater}$: Li isotope composition of modern seawater, i.e., 31‰.

V_{river}: volume of Amazon river water contributed during conservative mixing based on Li concentration.

$V_{seawater}$: volume of seawater contributed during conservative mixing based on Li concentration.

V_{total}: total volume of water from mixing of river water and seawater.

$F V_{riverwater}$: mass fraction of the water volume contributed by Amazon river water

$F V_{seawater}$: mass fraction of the water volume contributed by seawater, assuming a density of seawater approximately equal to river water.

$F Li_{riverwater}$: mass fraction of the Li contributed by Amazon river water.

$F\mathrm{Li}_{\text{seawater}}$: mass fraction of the Li contributed by seawater.

$\delta^7\mathrm{Li}_{\text{conservative}}$: dissolved Li isotope composition in the estuary that would be expected based on theoretical conservative mixing of river water and seawater.

$[\mathrm{Li}]_{\text{conservative}}$: Li concentration in the dissolved load based on conservative mixing of river water and seawater. It is the same as $[\mathrm{Li}]_{\text{measured}}$ at the measured sample points.

$[\mathrm{Li}]_{\text{after-removal}}$: Li concentration in the dissolved load after Li removal by sediments.

$\delta^7\mathrm{Li}_{\text{after-removal}}$: Li isotope composition in the dissolved load after Li removal by sediments.

f: fraction of Li that remains in the dissolved load after Li removal by sediments.

$[\mathrm{Li}]_{\text{sediment added}}$: the mass of Li per gram that is gained by sediments in the estuary.

SSC: suspended sediment concentration.

α: Li isotopic fractionation factor.

$\mathrm{Load}_{\text{river sediment}}$: mass per unit time of sediment transported by river water to the estuary (i.e., erosion rate if it is calculated based on the SSC in the river water).

Flux $\mathrm{Li}_{\text{sediment removal}}$: the flux of Li (mass) removed in the estuary by the river-transported sediments.

$\mathrm{MLi}_{\text{riverwater}}$: accumulated mass of Li supplied by the river water to a given point during the conservative mixing of river water and seawater.

$\mathrm{MLi}_{\text{seawater}}$: accumulated mass of Li supplied by the seawater to a given point during the conservative mixing of river water and seawater.

Σf: fraction of Li that remains in the dissolved load after Li removal by sediments accumulated to a given point in the estuary.

Σf_{river}: fraction of Li supplied by the river water that remains in the dissolved Li supplied by

the river water after Li removal by sediments accumulated to a given point in the estuary.

$\Sigma f_{seawater}$: fraction of Li supplied by the seawater that remains in the dissolved Li supplied by

the seawater after Li removal by sediments accumulated to a given point in the estuary.

References

Andrews, E., Pogge von Strandmann, P. A. E., Fantle, M. S., 2020. Exploring the importance of authigenic clay formation in the global Li cycle. Geochim. Cosmochim. Acta 289, 47–68.

Bastian, L., Vigier, N., Reynaud, S., Kerros, M. E., Revel, M., Bayon, G., 2018. Lithium isotope composition of marine biogenic carbonates and related reference materials. Geostand. Geoanal. Res. 42, 403–415.

Baturin, G. N., Gordeev, V. V., 2019. Geochemistry of Suspended Matter in the Amazon River Waters. Geochemistry Int. 57, 197–205.

Bigham, J. M., Fitzpatrick, R. W., Schulze, D. G., 2002. Iron oxides. Soil Mineral. with Environ. Appl. 7, 323–366.

Boyle, E. A., Edmond, J. M., Sholkovitz, E. R., 1977. The mechanism of iron removal in estuaries. Geochim. Cosmochim. Acta 41, 1313–1324.

Chan, L. H., Hein, J. R., 2007. Lithium contents and isotopic compositions of ferromanganese deposits from the global ocean. Deep. Res. Part II Top. Stud. Oceanogr. 54, 1147–1162.

Chester, R., 1990. Marine Geochemistry. Unwin Hyman Ltd, London.

Dellinger, M., Gaillardet, J., Bouchez, J., Calmels, D., Louvat, P., Dosseto, A., Gorge, C., Alanoca, L., Maurice, L., 2015. Riverine Li isotope fractionation in the Amazon River basin controlled by the weathering regimes. Geochim. Cosmochim. Acta 164, 71–93.

Dellinger, M., Hardisty, D. S., Planavsky, N. J., Gill, B. C., Kalderon-Asael, B., Asael, D., Croissant, T., Swart, P. K., West, A. J., 2020. The effects of diagenesis on lithium isotope ratios of shallow marine carbonates. Am. J. Sci. 320, 150–184.

Gaillardet, J., Dupré, B., Louvat, P., Allègre, C. J., 1999. Global silicate weathering and CO_2

consumption rates deduced from the chemistry of large rivers. Chem. Geol. 159, 3–30.

Gibbs, R. J., 1967. The Geochemistry of the Amazon River System: Part I. The Factors that Control the Salinity and the Composition and Concentration of the Suspended Solids. GSA Bull. 78, 1203–1232.

Gibbs, R. J., 1976. Amazon River sediment transport in the Atlantic Ocean. Geology 4, 45–48.

Hindshaw, R. S., Aciego, S. M., Tipper, E. T., 2018. Li and U isotopes as a potential tool for monitoring active layer deepening in permafrost dominated catchments. Front. Earth Sci. 6, 102.

Kinniburgh, D., Cooper, D., 2011. PhreePlot: Creating graphical output with PHREEQC.

Kineke, G. C., Sternberg, R. W., Trowbridge, J. H., Geyer, W. R., 1996. Fluid-mud processes on the Amazon continental shelf. Cont. Shelf Res. 16, 667–696.

Koschinsky, A., Frank, M., Dittmar, T., Gledhill, M., de Rezende, C., Lodeiro, P., Seidel, M., Knoke, M., Paul, S., Zitoun, R., Heinrich, L., Fronzek, J., Münch, J., Scholten, J., Border, E., Schneider, A., de Carvalho, L., Leist, L., Mutzberg, A., Marques da Silva Jr., J., Cherene Bras de Oliveira, B., Walter, J., Soares Nóbrega, M., Bretschneider, L., Hathorne, E., Vosteen, P., Spiegel, T., Maguire, C., Rohleder, C., 2018. Interactions of trace metals, DOM, and particles in the Amazon estuary and associated plume as key processes for trace metal and DOM fluxes into the Atlantic. A contribution to the internatinal GEOTRACES program Cruise No. M147.

Kuehl, S. A., Nittrouer, C. A., DeMaster, D. J., 1982. Modern sediment accumulation and strata formation on the Amazon continental shelf. Mar. Geol. 49, 279–300.

Lenstra, W. K., Klomp, R., Molema, F., Behrends, T., Slomp, C. P., 2021. A sequential extraction procedure for particulate manganese and its application to coastal marine sediments.

Chem. Geol. 584, 120538.

Li, W., Liu, X. M., 2020. Experimental investigation of lithium isotope fractionation during kaolinite adsorption: Implications for chemical weathering. Geochim. Cosmochim. Acta 284, 156–172.

Li, W., Liu, X. M., Chadwick, O. A., 2020. Lithium isotope behavior in Hawaiian regoliths: Soil-atmosphere-biosphere exchanges. Geochim. Cosmochim. Acta 285, 175–192.

Liu, C. Y., Pogge von Strandmann, P. A. E., Tarbuck, G., Wilson, D. J., 2022. Experimental investigation of oxide leaching methods for Li isotopes. Geostand. Geoanal. Res. 46, 493–518.

Martinelli, L. A., Victoria, R. L., Dematte, J. L. I., Richey, J. E., Devol, A. H., 1993. Chemical and mineralogical composition of Amazon River floodplain sediments, Brazil. Appl. Geochemistry 8, 391–402.

Michalopoulos, P., Aller, R. C., 1995. Rapid clay mineral formation in Amazon delta sediments: Reverse weathering and oceanic elemental cycles. Science 270, 614–617.

Milliman, J. D., Farnsworth, K. L., 2011. River discharge to the coastal ocean: A global synthesis. Cambridge University Press. New York.

Misra, S., Froelich, P. N., 2012. Lithium isotope history of cenozoic seawater: Changes in silicate weathering and reverse weathering. Science 335, 818–823.

Murphy, M. J., Porcelli, D., Pogge von Strandmann, P. A. E., Hirst, C. A., Kutscher, L., Katchinoff, J. A., Mörth, C. M., Maximov, T., Andersson, P. S., 2019. Tracing silicate weathering processes in the permafrost-dominated Lena River watershed using lithium isotopes. Geochim. Cosmochim. Acta 245, 154–171.

Parkhurst, D. L., Appelo, C. A. J., 2013. Description of input and examples for PHREEQC

version 3—A computer program for speciation, batch-reaction, one-dimensional transport, and inverse geochemical calculations. US Geol. Surv. Tech. methods 6, 497.

Pistiner, J. S., Henderson, G. M., 2003. Lithium-isotope fractionation during continental weathering processes. Earth Planet. Sci. Lett. 214, 327–339.

Pogge von Strandmann, P. A. E., James, R. H., van Calsteren, P., Gíslason, S. R., Burton, K. W., 2008. Lithium, magnesium and uranium isotope behaviour in the estuarine environment of basaltic islands. Earth Planet. Sci. Lett. 274, 462–471.

Pogge von Strandmann, P. A. E., Jenkyns, H. C., Woodfine, R. G., 2013. Lithium isotope evidence for enhanced weathering during Oceanic Anoxic Event 2. Nat. Geosci. 6, 668–672.

Pogge von Strandmann, P. A. E., Fraser, W. T., Hammond, S. J., Tarbuck, G., Wood, I. G., Oelkers, E. H., Murphy, M. J., 2019a. Experimental determination of Li isotope behaviour during basalt weathering. Chem. Geol. 517, 34–43.

Pogge von Strandmann, P. A. E., Schmidt, D. N., Planavsky, N. J., Wei, G., Todd, C. L., Baumann, K. H., 2019b. Assessing bulk carbonates as archives for seawater Li isotope ratios. Chem. Geol. 530, 119338.

Pogge von Strandmann, P. A. E, Dellinger, M., West, A. J., 2021. Lithium Isotopes: A Tracer of Past and Present Silicate Weathering, in: Lyons, T., Turchyn, A., Reinhaed, C. (Eds.), Geochemical Tracers Earth System Science. Cambridge University Press, Cambridge, pp. 1–24.

Pogge von Strandmann, P. A. E., Liu, X., Liu, C. Y., Wilson, D. J., Hammond, S. J., Tarbuck, G., Aristilde, L., Krause, A. J., Fraser, W. T., 2022. Lithium isotope behaviour during basalt weathering experiments amended with organic acids. Geochim. Cosmochim. Acta 328, 37–57.

Poulton, S. W., Canfield, D. E., 2005. Development of a sequential extraction procedure for iron: implications for iron partitioning in continentally derived particulates. Chem. Geol. 214, 209–221.

Robie, R., Hemingway, B., 1995. Thermodynamic properties of minerals and related substances at 298.15 K and 1 bar (10^5 Pascals) pressure and at higher temperatures. Bull. U.S. Geol. Surv. 2131, pp.461.

Sayles, F. L., Mangelsdorf Jr., P. C., 1979. Cation-exchange characteristics of Amazon River suspended sediment and its reaction with seawater. Geochim. Cosmochim. Acta 43, 767–779.

Sholkovitz, E. R., Boyle, E. A., Price, N. B., 1978. The removal of dissolved humic acids and iron during estuarine mixing. Earth Planet. Sci. Lett. 40, 130–136.

Sholkovitz, E. R., 1978. The flocculation of dissolved Fe, Mn, Al, Cu, Ni, Co and Cd during estuarine mixing. Earth Planet. Sci. Lett. 41, 77–86.

Smrzka, D., Zwicker, J., Bach, W., Feng, D., Himmler, T., Chen, D., Peckmann, J., 2019. The behavior of trace elements in seawater, sedimentary pore water, and their incorporation into carbonate minerals: a review. Facies 65, 41.

Spiegel, T., Vosteen, P., Wallmann, K., Paul, S. A. L., Gledhill, M., Scholz, F., 2021. Updated estimates of sedimentary potassium sequestration and phosphorus release on the Amazon shelf. Chem. Geol. 560, 120017.

Tardy, Y., 1971. Characterization of the principal weathering types by the geochemistry of waters from some European and African crystalline massifs. Chem. Geol. 7, 253–271.

Ullmann, C. V., Campbell, H. J., Frei, R., Hesselbo, S. P., Pogge von Strandmann, P. A. E., Korte, C., 2013. Partial diagenetic overprint of Late Jurassic belemnites from New Zealand:

Implications for the preservation potential of δ^7Li values in calcite fossils. Geochim. Cosmochim. Acta 120, 80–96.

Velde, B, 1995. Origin and Mineralogy of Clays. Springer, Germany.

Vosteen, P., Spiegel, T., Gledhill, M., Frank, M., Zabel, M., Scholz, F., 2022. The fate of sedimentary reactive iron at the land-ocean interface: A case study from the Amazon shelf. Geochem. Geophys., 23, e2022GC010543.

Washington, K. E., West, A. J., Kalderon-Asael, B., Katchinoff, J. A. R., Stevenson, E. I., Planavsky, N. J., 2020. Lithium isotope composition of modern and fossilized Cenozoic brachiopods. Geology 48, 1058–1061.

Wimpenny, J., Gíslason, S. R., James, R. H., Gannoun, A., Pogge von Strandmann, P. A. E., Burton, K. W., 2010. The behaviour of Li and Mg isotopes during primary phase dissolution and secondary mineral formation in basalt. Geochim. Cosmochim. Acta 74, 5259–5279.

Yang, C., Vigier, N., Lian, E., Lai, Z., Yang, S., 2021. Decoupling of dissolved and particulate Li isotopes during estuarine processes. Geochem. Perspect. Lett. 19, 40–44.

Zhang, L., Chan, L. H., Gieskes, J. M., 1998. Lithium isotope geochemistry of pore waters from Ocean Drilling Program Sites 918 and 919, Irminger Basin. Geochim. Cosmochim. Acta 62, 2437–2450.
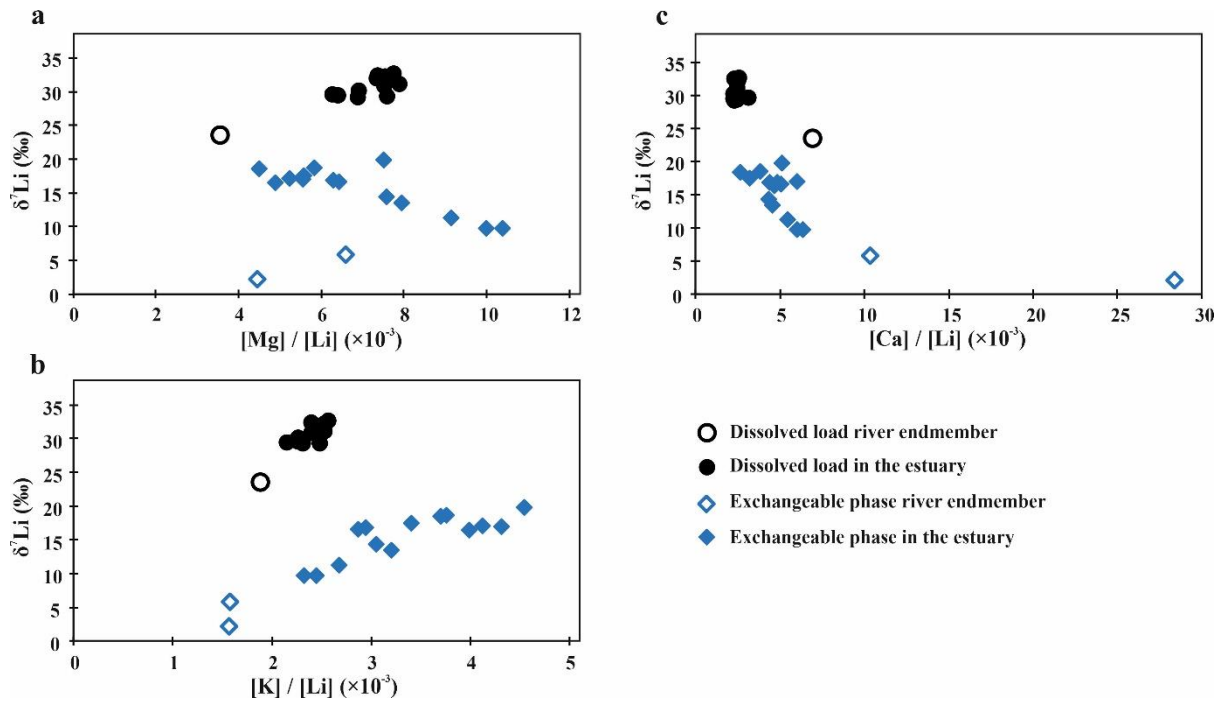
Figures

Fig. S1. Negligible influence of the remaining dissolved load on the exchangeable pool.

(a) Li isotope compositions versus Mg/Li ratios. (b) Li isotope compositions versus K/Li ratios.

(c) Li isotope compositions versus Ca/Li ratios. The open black circles and open blue diamonds

are the dissolved load (W66) and the exchangeable phases extracted from sediments (24MUC

and 67MUC) that represent the river endmember near the beginning of the Amazon estuary.

The filled black circles and filled blue diamonds represent the other samples from the Amazon

estuary. The element ratios are by mass.
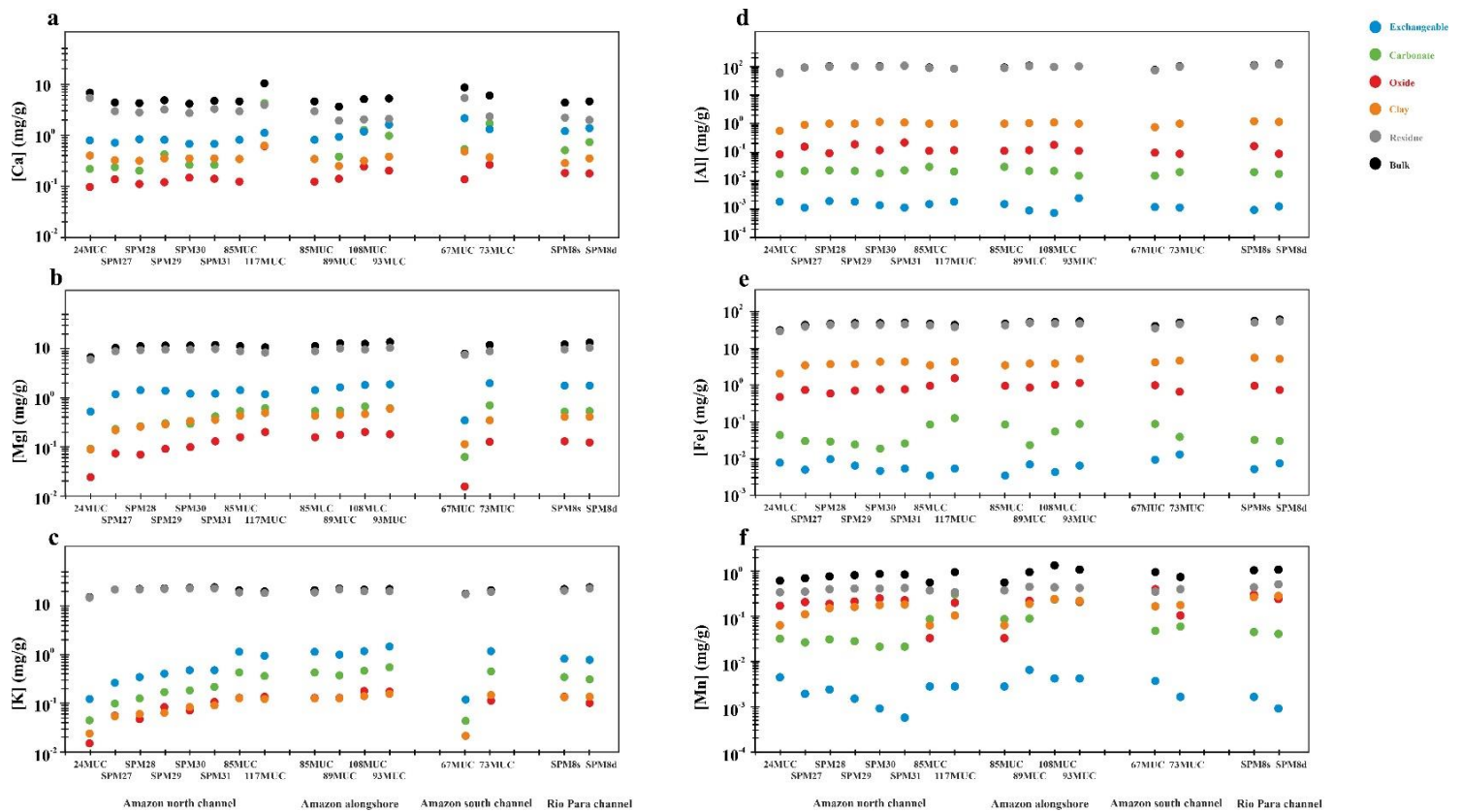
Fig. S2. Elemental concentrations for different phases of the sediment samples.

Panels (a), (b), (c), (d), (e) and (f) are the concentrations of Ca, Mg, K, Al, Fe and Mn for different phases of the sediment samples. Note that the phases are separated based on sequential leaching, and that the carbonate phase is probably influenced by the leaching of phases other than carbonate (Supplementary Material S2). The data labelled 'bulk' represent the sum of the other fractions, based on Eq. (2) in the main text. Where the black data points are not visible, they are hidden by the grey data points because of their similar values. Note that data from sample 41MUC are not shown.
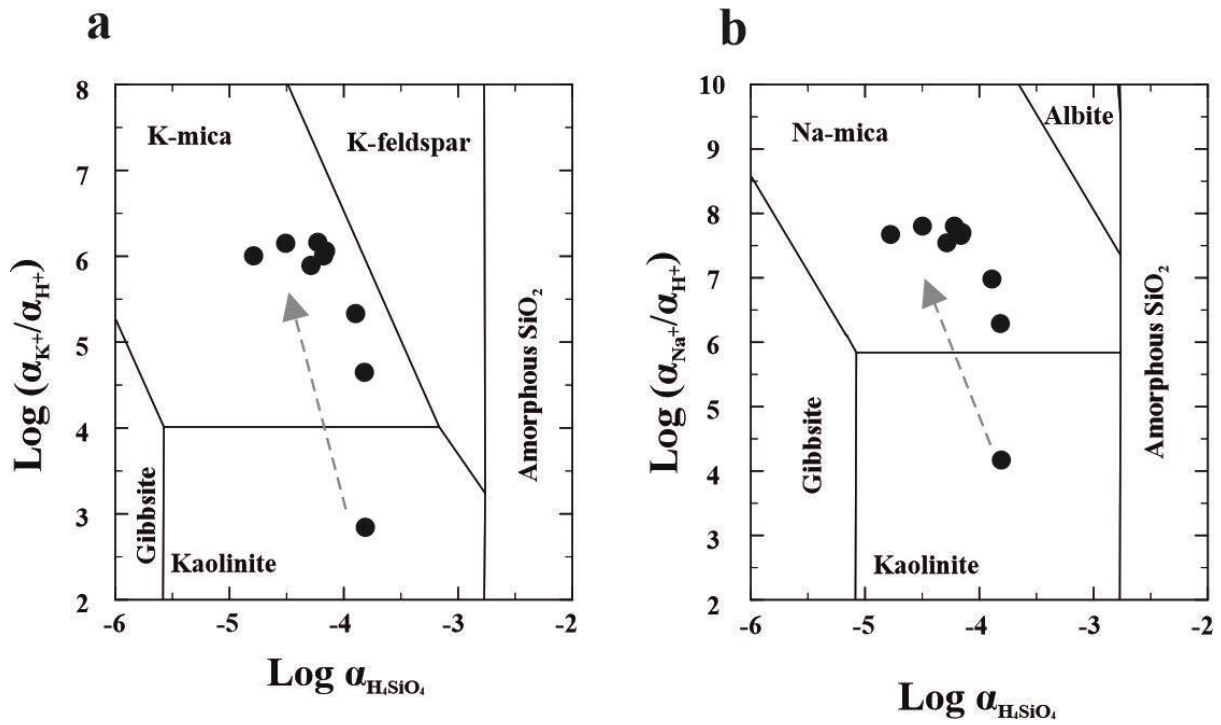
Fig. S3. Stability diagrams of K-aluminosilicate and Na-aluminosilicate.

(a) Stability diagram of K-aluminosilicate. (b) Stability diagram of Na-aluminosilicate. Calculations for individual water samples are shown as black filled circles, and the grey arrows indicate the direction from river to ocean. For details, see Supplementary Material S6.
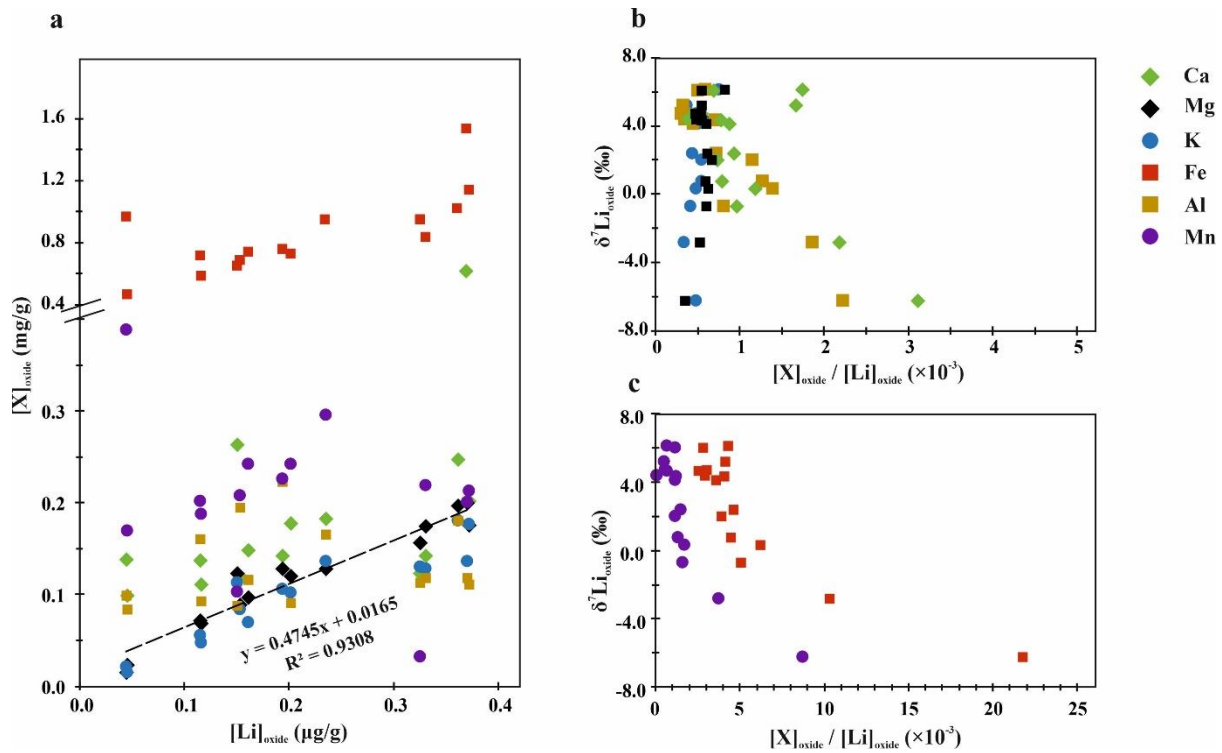
Fig. S4. The retention of cations in oxide phases.

(a) Trends of major element concentrations (Ca, Mg, K, Fe, Al, Mn) with Li concentrations in the leached oxide phase of the sediment samples, i.e., SPM and MUC (except for 41MUC). The black dashed line is a best-fit line for $[Mg]_{oxide}$ and $[Li]_{oxide}$. (b) Trends of Li isotope compositions with Ca, Mg, K and Al concentrations (plotted as ratios to Li concentrations) in the leached oxide phase of the sediment samples, i.e., SPM and MUC (except for 41MUC). (c) Trends of Li isotope compositions with Fe and Mn concentrations (plotted as ratios to Li concentrations) in the leached oxide phase of the sediment samples, i.e., SPM and MUC (except for 41MUC). The element ratios are by mass.
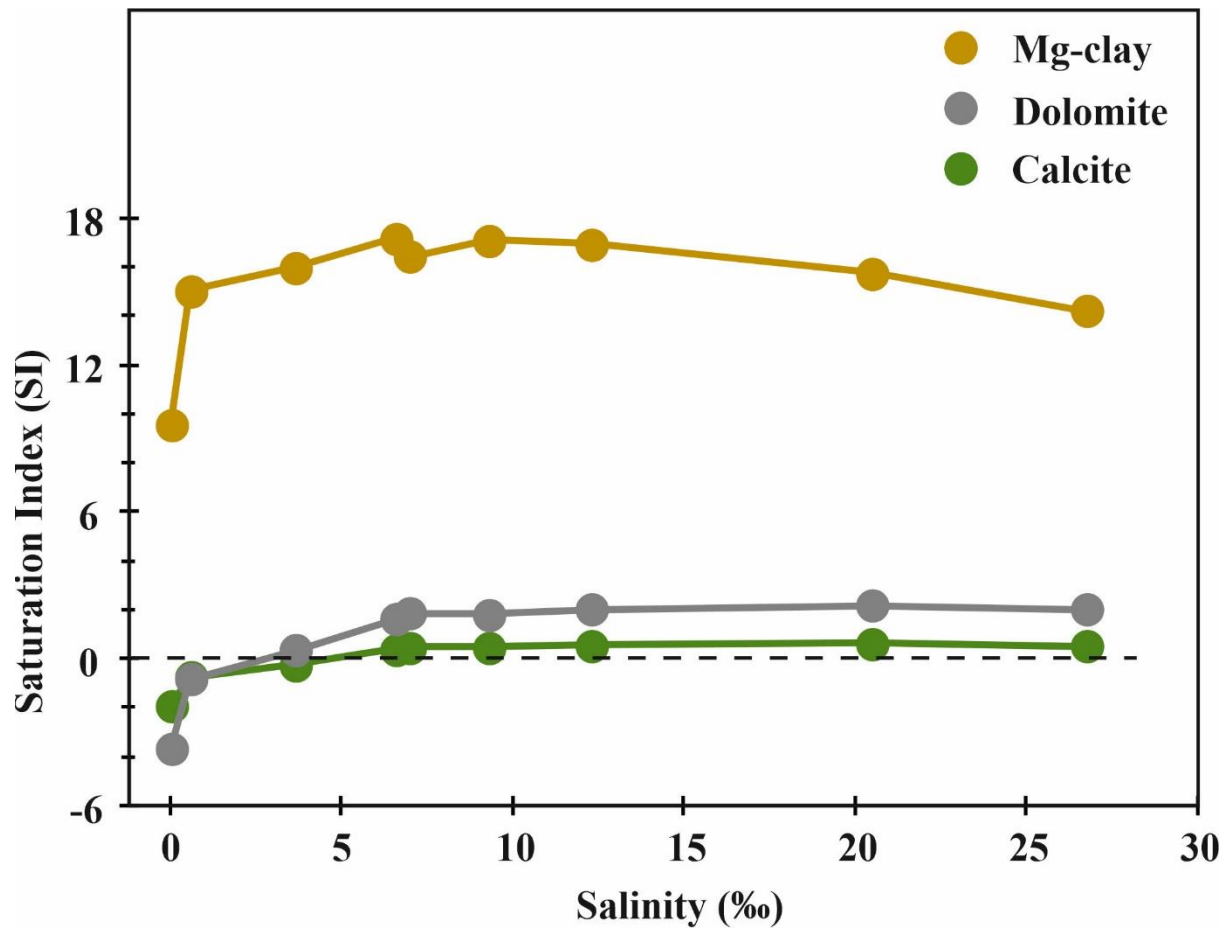
Fig. S5. Calculated saturation index (SI) for selected minerals in the Amazon estuary.

The dashed black line is plotted at SI=0; lower values are undersaturated and higher values are supersaturated. For details, see Supplementary Material S6 and Table S1. The Mg-clay here is sepiolite.
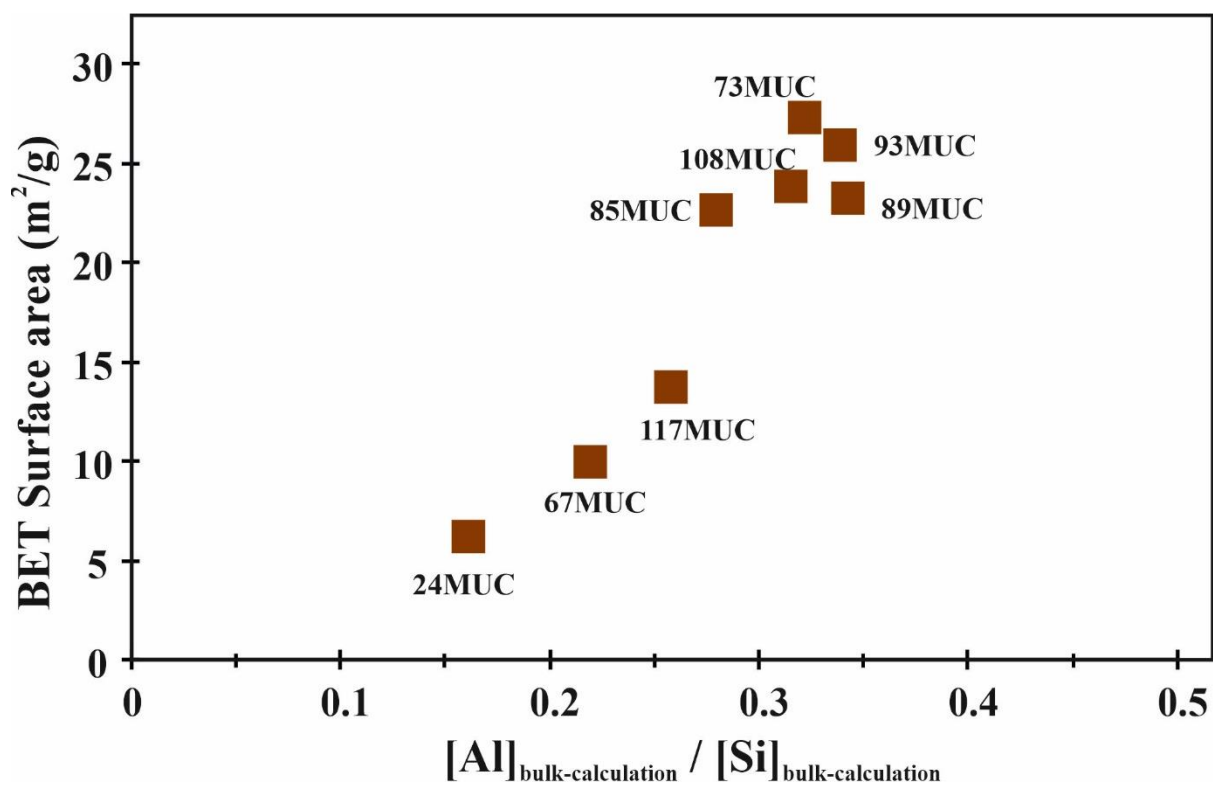
Fig. S6. Relationship between BET surface area and bulk Al/Si ratios in the MUC sediment samples.

Sample 41MUC is excluded because of its high carbonate content. The element ratios are by mass. The surface area of the MUC samples was determined by Nova 1200 (Quantachrome) at Johannes Gutenberg University, Mainz.
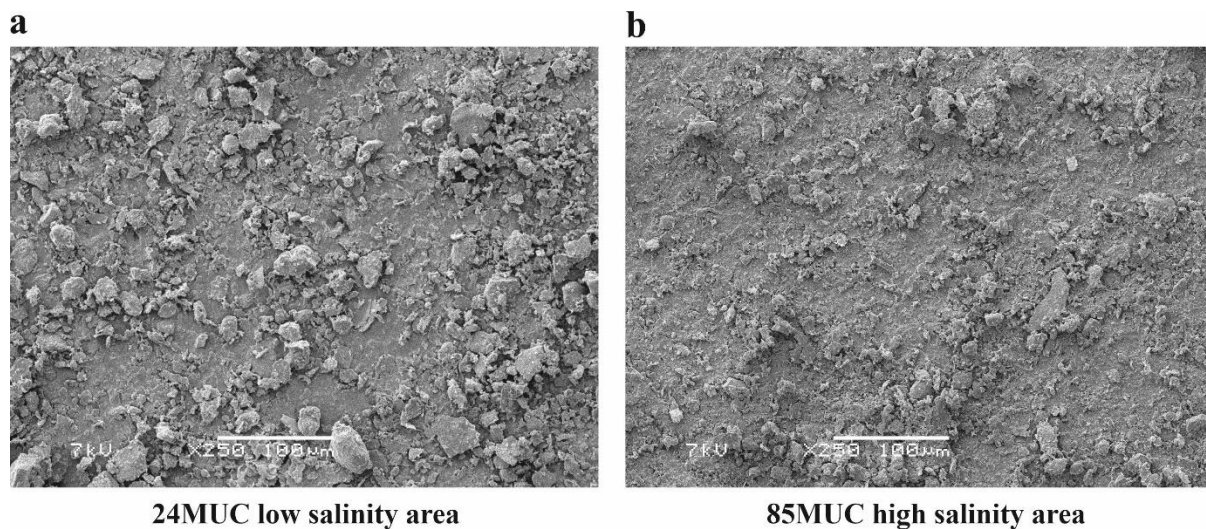
24MUC low salinity area   **85MUC high salinity area**

Fig. S7. SEM images for sediment samples 24MUC and 85MUC.

(a) Sample 24MUC at 50 km away from the Amazon river mouth in the estuary. (b) Sample 85MUC at around 200 km away from the Amazon river mouth in the estuary. Samples were imaged at UCL with a Jeol JSM-6480LV high-performance Variable Pressure Analytical Scanning Electron Microscope, using a 7 kV accelerating voltage and around 9 mm working distance. The scale bars are 100 μm.